National Library
of Canada

Bibliothèque nationale
du Canada

Canadian Theses Service

Service des thèses canadiennes

Ottawa, Canada
K1A 0N4

NOTICE

The quality of this microform is heavily dependent upon the quality of the original thesis submitted for microfilming. Every effort has been made to ensure the highest quality of reproduction possible.

If pages are missing, contact the university which granted the degree.

Some pages may have indistinct print especially if the original pages were typed with a poor typewriter ribbon or if the university sent us an inferior photocopy.

Reproduction in full or in part of this microform is governed by the Canadian Copyright Act, R.S.C. 1970, c. C-30, and subsequent amendments.

AVIS

La qualité de cette microforme dépend grandement de la qualité de la thèse soumise au microfilmage. Nous avons tout fait pour assurer une qualité supérieure de reproduction.

S'il manque des pages, veuillez communiquer avec l'université qui a conféré le grade.

La qualité d'impression de certaines pages peut laisser à désirer, surtout si les pages originales ont été dactylographiées à l'aide d'un ruban usé ou si l'université nous a fait parvenir une photocopie de qualité inférieure.

La reproduction, même partielle, de cette microforme est soumise à la Loi canadienne sur le droit d'auteur, SRC 1970, c. C-30, et ses amendements subséquents.

NL-339 (r. 88/04) c

Canada

UNIVERSITY OF ALBERTA

REDUCING ANTENNA NOISE IN A SYNTHESIS TELESCOPE
AND
AN OBSERVATION OF AN HII REGION

BY

MARCUS DUANE ANDERSON

A THESIS
SUBMITTED TO THE FACULTY OF GRADUATE STUDIES AND RESEARCH
IN PARTIAL FULFILLMENT OF THE REQUIREMENTS FOR THE DEGREE
OF MASTER OF SCIENCE.

DEPARTMENT OF ELECTRICAL ENGINEERING

EDMONTON ALBERTA
SPRING 1990

National Library of Canada
Canadian Theses Service
Ottawa, Canada
K1A 0N4

Bibliothèque nationale du Canada
Service des thèses canadiennes

NOTICE

The quality of this microform is heavily dependent upon the quality of the original thesis submitted for microfilming. Every effort has been made to ensure the highest quality of reproduction possible.

If pages are missing, contact the university which granted the degree.

Some pages may have indistinct print especially if the original pages were typed with a poor typewriter ribbon or if the university sent us an inferior photocopy.

Reproduction in full or in part of this microform is governed by the Canadian Copyright Act, R.S.C. 1970, c. C-30, and subsequent amendments.

AVIS

La qualité de cette microforme dépend grandement de la qualité de la thèse soumise au microfilmage. Nous avons tout fait pour assurer une qualité supérieure de reproduction.

S'il manque des pages, veuillez communiquer avec l'université qui a conféré le grade.

La qualité d'impression de certaines pages peut laisser à désirer, surtout si les pages originales ont été dactylographiées à l'aide d'un ruban usé ou si l'université nous a fait parvenir une photocopie de qualité inférieure.

La reproduction, même partielle, de cette microforme est soumise à la Loi canadienne sur le droit d'auteur, SRC 1970, c. C-30, et ses amendements subséquents.

ISBN 0-315-60252-X

NL-339 (r. 88/04) c

Canada

UNIVERSITY OF ALBERTA

RELEASE FORM

NAME OF AUTHOR: MARCUS DUANE ANDERSON

TITLE OF THESIS: REDUCING ANTENNA NOISE IN A SYNTHESIS TELESCOPE AND AN OBSERVATION OF AN HII REGION

DEGREE: MASTER OF SCIENCE

YEAR THIS DEGREE GRANTED: 1990

PERMISSION IS HEREBY GRANTED TO THE UNIVERSITY OF ALBERTA LIBRARY TO REPRODUCE SINGLE COPIES OF THIS THESIS AND TO LEND OR SELL SUCH COPIES FOR PRIVATE, SCHOLARLY OR SCIENTIFIC RESEARCH PURPOSES ONLY.

THE AUTHOR RESERVES OTHER PUBLICATION RIGHTS, AND NEITHER THE THESIS NOR EXTENSIVE EXTRACTS FROM IT MAY BE PRINTED OR OTHERWISE REPRODUCED WITHOUT THE AUTHOR'S WRITTEN PERMISSION.

Marcus D. Anderson

BOX 56
VICEROY, SASKATCHEWAN
S0H 4H0

Date: December 22ND 1989

UNIVERSITY OF ALBERTA

FACULTY OF GRADUATE STUDIES AND RESEARCH

THE UNDERSIGNED CERTIFY THAT THEY HAVE READ, AND RECOMMENDED TO THE FACULTY OF GRADUATE STUDIES AND RESEARCH FOR ACCEPTANCE, A THESIS ENTITLED "REDUCING ANTENNA NOISE IN A SYNTHESIS TELESCOPE AND AN OBSERVATION OF AN HII REGION"

SUBMITTED BY MARCUS DUANE ANDERSON

IN PARTIAL FULFILLMENT OF THE REQUIREMENTS FOR THE DEGREE OF MASTER OF SCIENCE.

JFVaneldik

Dr. J.F. Vaneldik
(Supervisor)

Thomas Landecker

Dr. T.L. Landecker
(Supervisor)

D. Routledge

Dr. D. Routledge

Dr. D.P. Hube

Date: December 20TH 1989

ABSTRACT

This thesis explores two topics which are related to the synthesis telescope at the Dominion Radio Astrophysical Observatory (DRAO). The first topic is an investigation into the antenna performance at 1420 MHz. It has shown how to improve the sensitivity of the telescope by reducing the antenna temperature of the individual elements of the array. Each antenna of the array has an antenna temperature of about 26 K.

The power pattern of one of the antennas was measured to obtain a better understanding of the individual contributors to antenna temperature. It has also enabled a numerical calculation of antenna temperature to be performed. The results of the calculation show that spillover and feedleg scatter are significant contributors to antenna temperature. A reduction of antenna temperature from these two sources was obtained by adding two modifications to the antenna. The first modification was a fence placed on the rim of the antenna which lowered the antenna temperature by about 8 K, by partially suppressing the spillover lobe and feedleg scatter lobes. The second modification involved changing the shape of the feedlegs from a circular to a triangular cross-section. This lowered the antenna temperature by about 5 K, by directing the scatter lobes from the feedlegs up off the ground and

into the sky. The results of these experiments have shown that a significant reduction of antenna temperature can be achieved with fairly simple modifications to the antennas.

The second topic of this thesis is an observation of Sharpless 183 (S183), with the synthesis telescope at DRAO. Previous radio observations of this object have failed to show conclusively whether the object is an HII region or a supernova remnant. The 408 MHz and 1420 MHz maps from the synthesis telescope have better resolution than any of the previous observations of this object. They have shown that S183 has flux densities of 6.33 ± 0.40 and 6.92 ± 0.50 Jy at 1420 MHz and 408 MHz respectively. The spectral index was found to be 0.07 ± 0.05, implying that S183 is probably an HII region, contradicting earlier suggestions in the literature that it is a supernova remnant. Modeling indicates that ~ 67 $M_\odot$ of ionized material is present with $N_e \sim 12.5\ cm^{-3}$.

ACKNOWLEDGMENTS

Many individuals have been very helpful to me over the course of this project. First, I wish to thank my supervisors, Tom Landecker, Dave Routledge, and Fred Vaneldik for their support, encouragement, and helpful suggestions.

I am grateful to Lloyd Higgs and Geoff Croes who wrote much of the software that I used while at DRAO, and answered my many questions. Ron Casorso was very helpful during the measurement of the antenna power pattern, and made many trips on foot up and down the mountain to our transmitter location. Erika Rohner and Cindy Furtado arranged very comfortable accommodations for myself and my family during our summer stay in Penticton. Rob Roger and Tom Landecker provided me with many rides to and from the observatory. During my visits I found it a pleasure to work with all the staff at DRAO.

Additionally, I would like to thank Robert Morse from U of A Department of Applied Science in Medicine, who helped me combine the two sets of digitized antenna pattern data into a single usable file.

My parents have always been ready and willing to lend a helping hand when needed, which I have appreciated very much.

Finally, I owe my warmest thanks to my wife LuEllen, my son John, and my daughter Sarah, who have been at my side throughout this project.

TABLE OF CONTENTS

Chapter Page

1. INTRODUCTION 1

    1.1 The Birth of Radio Astronomy 1

    1.2 The Method of Aperture Synthesis 3

    1.3 The DRAO Synthesis Telescope 16
        1.3.1 Synthesis Telescope Sensitivity 18
        1.3.2 Loss in the Transmission Line 23
        1.3.3 Noise Contribution from the Amplifier 23
        1.3.4 Noise Due to Antenna Temperature 24

    1.4 Topics of Thesis 29

2. DETERMINATION OF ANTENNA TEMPERATURE 33

    2.1 Individual Contributors to Antenna Temperature 33
        1) Atmospheric Noise Contribution 34
        2) Sky Contribution 34
        3) Spillover Contribution 34
        4) Mesh Leakage Contribution 38
        5) Diffraction Contribution 39

    2.2 Data Collection and Presentation 45
        2.2.1 The Experimental Measurements 47
        2.2.2 Accuracy of the Measurements 53
        2.2.3 Data Presentation 58
            1) The RA-DEC Coordinate System 58
            2) The RHO-PHI Coordinate System in Rectangular Form 61
            3) The RHO-PHI Coordinate System in Polar Form 64

    2.3 Calculation of Antenna Temperature Using the Power Pattern of the Far East Antenna 68
        2.3.1 Considerations Required Before Determining Antenna Temperature 69
        2.3.2 Numerical Calculation of Antenna Temperature Using the Pattern 76
        3.3.3 Summary of Results 85

3. TWO METHODS OF REDUCING ANTENNA TEMPERATURE 89

3.1 The Method Used to Measure Antenna Temperature 90
  3.1.1 The Receiver 90
  3.1.2 The Measurement Method 92

3.2 Experimental Reduction of Antenna Temperature Using a Fence 96

3.3 Reduction of Antenna Temperature Using Feedlegs with a Triangular Cross-Section 101
  3.3.1 Characteristics of the Feedleg Lobes in the $\rho - \phi$ Plane 101
    1) Location of the Scatter Cones in the (ρ, ϕ) System 101
    2) Width of the Scatter Cones 108
    3) Average Power Levels in the Scatter Cones 109
  3.3.2 An Estimate of Antenna Temperature Due to Feedleg Scatter 118
  3.3.3 Reduction of Antenna Temperature By Modifying the Shape of the Feedlegs 121
  3.3.4 Results 132

3.4 Feedleg Scatter as a Function of Size, Configuration, and Material of the Feedlegs 133

3.5 Summary of the Antenna Work 144
  3.5.1 Antenna Measurement Discrepancy Explained 144
  3.5.2 Results of Antenna Modifications 148
  3.5.3 Recommendations 152

4. INTRODUCTION TO SHARPLESS 183 156

4.1 Previous Observations of S183 157

5. THE S183 SURVEY 164

5.1 Observations and Data Reduction 164
  5.1.1 Preliminary Data Reduction 164
  5.1.2 Cleaning the Maps 164
  5.1.3 Adding the Low Order Spacings 177

5.2 Results 191

6. INTERPRETATION OF OBSERVATIONS OF S183 201

6.1 408 MHz and 1420 MHz Data 201
  6.1.1 Determination of Spectral Index 201
  6.1.2 A Model of S183 215
  6.1.3 Exciting Star of S183 237
  6.1.4 The Search for a Radio Recombination Line in S183 242

6.2 IRAS (Infrared Astronomical Satellite) Data 245
  6.2.1 Calculation of Dust Temperatures 245
  6.2.2 Calculation of the Parameter "R" 251

6.3 LBN 0611 253

6.4 Conclusions 253

7. CONCLUSIONS 255

REFERENCES 258

LIST OF TABLES

Table	Description	Page
1.1	Antenna Parameters of the Synthesis Telescope	17
1.2	Estimates of the Contribution to System Noise for the DRAO Synthesis Telescope at 1420 MHz	22
2.1	Calculation of T_A Due to Spillover	37
2.2	Calculation of T_A Due to Diffraction	43
2.3	Theoretical Values for the Contributors to T_A	46
2.4	Measurements of T_G	74
2.5	Summary of Results of Antenna Temperature For the Far East Antenna	86
3.1	Antenna Temperature Measurements for the Fifth Antenna at the Zenith with and Without a Fence	99
3.2	Location of the Feedleg Lobes for the FE Antenna	106
3.3	Measured Widths of Scatter Cone Lobes From the Far East Antenna	111
3.4	Antenna Temperature for the Far East Antenna Due to the Feedleg Lobes for a Range of Average Power Levels	122
3.5	The Direction of the Scattered Wave from Triangular Shaped Feedlegs for Various Half-Vertex Angles	126
3.6	Antenna Temperature Measurements for the Fifth Antenna at the Zenith with Feedleg and Fence Modifications	131
3.7	Estimates of Antenna Temperature Due to Tripod Feedleg Arrangement Using IFR Method	136

3.8 Estimates of Antenna Temperature Due to Quadrupod Feedleg Arrangement Using IFR Method 137

3.9 Estimates of Antenna Temperature Due to Tripod of Dielectric Feedlegs Using IFR Method ($\epsilon_r = 5.2$) 139

3.10 Estimates of Antenna Temperature Due to Quadrupod of Dielectric Feedlegs Using IFR Method ($\epsilon_r = 5.2$)..........................140

3.11 Estimates of Antenna Temperature Due to Tripod of Dielectric Feedlegs Using IFR Method ($\epsilon_r = 2.5$)..........................141

3.12 Estimates of Antenna Temperature Due to Quadrupod of Dielectric Feedlegs Using IFR Method ($\epsilon_r = 2.5$)..........................142

3.13 Comparison of Estimates and Measurements of Antenna Temperature for the Antennas of the Synthesis Telescope 146

3.14 Summary of Antenna Temperature Measurements 150

5.1 Telescope Parameters and Survey Details for S183 165

6.1 Flux Density Measurements of S183 206

6.2 Measured Flux Densities for S183 210

6.3 Determination of Model Parameters for S183 231

6.4 Measured Brightness Temperatures of S183 ...233

6.5 Model Brightness Temperatures of S183 235

6.6 List of Parameters for the Model of S183 ...236

6.7 Summary of the main Characteristics of S183 238

6.8 Selected SAO Stars in the Field of S183 239

6.9 Excitation Parameter (U) for Stars of Spectral Type O4 to B1 241

LIST OF FIGURES

Figure	Description	Page
1.1	Definition of Coordinate Systems	5
1.2	A Radio Interferometer	7
1.3	The Ellipse in the uv Plane	8
1.4	Interferometer Output for a Strong and a Weak Radio Source	14
1.5	Noise Contributions in an Interferometer Pair	19
1.6	Regions that Contribute to Antenna Temperature	27
2.1	Sky and Atmospheric Noise Contributions to Antenna Temperature	35
2.2	Diffraction Around the Rim of the Far East Antenna	41
2.3	Configuration of the Equipment for Measuring the Power Pattern of the Far East Antenna	50
2.4	Scan Through the Main Beam	52
2.5	Flow Chart of Data Reduction Process	54
2.6	The Antenna Pattern Shown in the RA-DEC Coordinate System	60
2.7	Illustration of the RHO-PHI Coordinate System	62
2.8	The Antenna Pattern Shown in the RHO-PHI Coordinate System	63
2.9	Illustration of the RA-DEC to RHO-PHI Mapping Process	65
2.10	The Front Half of the Antenna Pattern for the Far East Antenna	66
2.11	The Rear Half of the Antenna Pattern for the Far East Antenna	67

2.12 The Number of Pixels in the PHI Direction that Contain Data as a Function of RHO 70

2.13 The Average Power (P_{AVE}) as a Function of RHO for the Far East Antenna 72

2.14 Effective Ground Temperature T_G as a Function of RHO 75

2.15 The RHO-PHI Antenna Pattern with the Horizon Superimposed 77

2.16 Cumulative Antenna Temperature as a Function of RHO 78

2.17 Antenna Temperature for Selected Areas of the Pattern 80

3.1 Block Diagram of the Dicke Receiver, and Results of the Linearity Test 91

3.2 A Determination of Antenna Temperature 94

3.3 An Antenna with a Fence 97

3.4 The Geometry of a Scatter Cone from One of the Feedlegs 103

3.5 Determining the Location of the Scatter Cones on the RHO-PHI System 104

3.6 Theoretical Locations of the Feedleg Lobes in the RHO-PHI System 107

3.7 Cross-Sections Through the Feedleg Scatter Lobes 110

3.8 IFR Values for Metallic Cylinders 113

3.9 Sidelobe Levels as a Function of the Parameter A_{CO} 114

3.10 The Direction of the Scattered Wave from a Triangular Feedleg 125

3.11 Direction of the scattered Wave for Various Half-Vertex Angles 128

3.12 The Modifications Added to the Feedlegs of the Fifth Antenna 130

3.13 Comparison of Metallic and Dielectric Feedlegs 143

3.14 Contributors to Antenna Temperature 149

4.1 A 1420 MHz Map which Includes S183 158

4.2 A 1400 MHz Map of S183 160

4.3 Map of Fan Beam Scans in the Region of S183 161

5.1 The preliminary 1024 X 1024 408 MHz Map 167

5.2 The Preliminary 512 X 512 408 MHz Map 169

5.3 The Preliminary 512 X 512 1420 MHz Map 170

5.4 The Beam Function Superimposed on the Map for Cleaning 173

5.5 The Clean 408 MHz Map 175

5.6 The Clean 1420 MHz Map 176

5.7 Telescope Transfer Functions 179

5.8 The Low Order 408 MHz Map 181

5.9 The Filter Applied to the uv Visibility Data 183

5.10 The Filtered 408 MHz Low Order Map 185

5.11 The Complete 408 MHz Map 188

5.12 The Final 408 MHz Map 189

5.13 The Low Order 1420 MHz Map 190

5.14 The Filtered Low Order 1420 MHz Map 192

5.15 The Complete 1420 MHz Map 193

5.16 The Final 1420 MHz Map 194

5.17 The 1420 MHz Map with Shading 195

5.18 The 408 MHz Map with Shading 196

6.1 The 408 MHz Polygons 207

6.2 The 1420 MHz Polygons 208

6.3 The Radio Spectrum of S183 211

6.4 The Brightness Temperature Spectral Index Map of S183 213

6.5 Model of S183 216

6.6 Brightness Temperature of the Components of S183 217

6.7 Rotation Curve of the Galaxy 219

6.8 Cross-Section Through Component 1 of S183 225

6.9 S183 at 60 µm 246

6.10 S183 at 100 µm 247

6.11 1420 MHz Map with 60 µm Emission Superimposed 248

6.12 Map of $T_{D\ 60/100}$ for S183 250

LIST OF PLATES

Plate	Description	Page
5.1	A Section of the Palomar Sky Survey Showing S183	198

CHAPTER 1

INTRODUCTION

This thesis covers two topics related to the Synthesis Telescope at the Dominion Radio Astrophysical Observatory (DRAO). The first is an investigation of antenna performance which has shown how to improve the sensitivity of the telescope substantially. The second is an investigation of the nature of the galactic nebula, Sharpless 183 (S183), based on observations with the telescope.

1.1 THE BIRTH OF RADIO ASTRONOMY

The field of radio astronomy is quite young when compared with its optical counterpart. It had its beginnings in the early 1930's when Karl Jansky, a radio engineer employed at Bell Telephone Laboratories, was studying the direction of arrival of thunderstorm static. It was hoped that the results of his work would enable the design of antenna networks that would have minimal responses in these directions, and hence, reduce the effects of this interference on transoceanic radio-telephone communications.

In January 1933 he reported the first results of his investigation. Along with two types of radio interference from thunderstorms, he identified a third, a steady hiss type of interference of unknown origin. Later in 1933, he had identified the source of this interference as being extraterrestial, and in 1935 he had isolated the Milky May Galaxy as its source. This discovery marked the beginning of radio astronomy, and since that time instruments of ever increasing size and sophistication have been designed and built to explore the radio sky.

Initially, single steerable antennas were constructed with a general emphasis on more collecting area with each new instrument. The increasing size of the telescopes enabled more power to be collected from a given direction with higher resolution. The end result of this development trend was the construction of the fully steerable, 100 m diameter parabolic reflector at Effelsberg near Bonn in 1972. The largest single antenna ever constructed is the 305 m spherical reflector at Arecibo, Puerto Rico, which is operated by Cornell University. The fixed antenna is built into a bowel shaped depression in the ground and its beam is partially steerable by moving the feed, which is suspended over the spherical reflector.

Larger single antenna instruments have not been constructed due to strength of materials limitations. Earth-based instruments therefore would have been limited to sizes of 100 m to 300 m, if new techniques had not been developed to overcome these design limitations.

1.2 THE METHOD OF APERTURE SYNTHESIS

The DRAO Synthesis Telescope is a member of a class of instruments which has overcome the size limitation stated above by a technique known as aperture synthesis. These telescopes synthesize large aperture measurements using arrays made up of much smaller and cheaper antennas. Aperture synthesis uses the fact that a Fourier transform relation exists between the sky radio brightness distribution $T_B(l,m)$, and the response of a radio interferometer $T(u,v)$ of variable baseline. The Fourier transform pair is given by equations 1.1 and 1.2[1].

$$T(u,v) = \iint M(l,m)e^{j2\pi(ul + vm)}dl\ dm \qquad 1.1a$$

where:

$$M(l,m) = \frac{1}{\lambda^2}\,2[A_1(l,m)\cdot A_2(l,m)]^{1/2}(1-l^2-m^2)^{-1/2}T_B(l,m) \qquad 1.1b$$

$$M(l,m) = \iint T(u,v)e^{-j2\pi(ul + vm)}\ du\ dv \qquad 1.2$$

The coordinate systems used in equations 1.1 and 1.2 are the sky coordinates (l,m) and the u-v plane coordinates (u,v). The relationship between these is illustrated by figures 1.1a and 1.1b. Figure 1.1a shows the u-v plane with a unit hemisphere superimposed. Any direction in the sky can be uniquely defined by two of the direction cosines $l = \cos\alpha$, $m = \cos\beta$, and $n = \cos\gamma$. Using l and m, an element of solid angle d , is defined by equation 1.3 below[2].

$$d\omega = \frac{dl\ dm}{\cos\gamma} = \frac{dl\ dm}{(1-l^2-m^2)^{1/2}} \qquad 1.3$$

Figure 1.1b shows the baseline B, in wavelengths between antennas 1 and 2 of an interferometer in the u-v plane. Distances u and v are measured in wavelengths toward the west and south respectively. If the antennas point to a source in the direction (l,m) in the sky, the source will see a projected baseline b. A phase delay ψ, given by equation 1.4, represents the geometric path length difference that an incoming signal sees as it is received by antennas 1 and 2 of the interferometer pair.

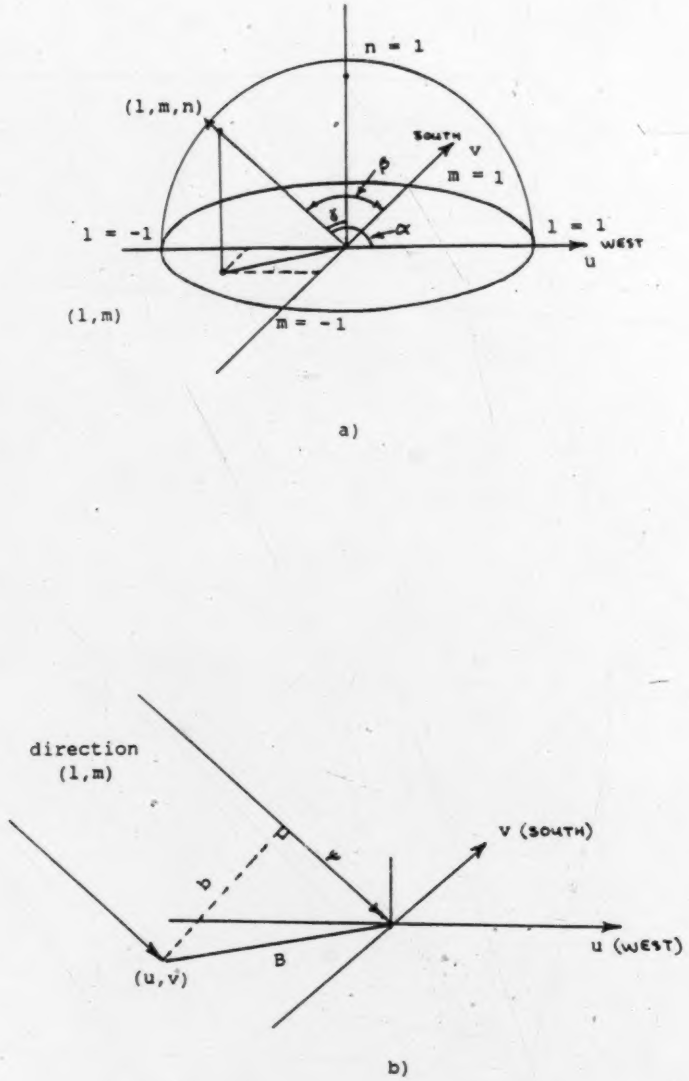

Figure 1.1
Definition of Coordinate Systems

a) Unit sphere showing a vector pointing to a source at the location (l,m,n) and its relationship to the angles (α, β, γ), (Adapted from Christiansen and Högbom[3]).

b) Sketch showing an interferometer baseline B observing a source in the direction (l,m). The sketch also shows the projected baseline b, and the phase difference $\psi = 2\pi(ul + vm)$ that a signal acquires as it encounters the antennas of the interferometer.

$$\psi = 2\pi(ul + vm) \qquad 1.4$$

Figure 1.2 shows one of a number of interferometers that are formed by correlating pairs of antennas in a synthesis telescope. As the antennas of the interferometer track the source, as they do in Earth rotation synthesis, the projected baseline (b) as seen from the source, traces out an ellipse in the u-v plane as shown in figure 1.3. The ellipse traced in the u-v plane is a result of the earth rotating with the baseline fixed to its surface, usually in an east-west orientation. The points near the major axis of the ellipse are measured when the interferometer baseline is at right angles to the direction of the source. Points near the minor axis of the ellipse are measured when the array is in line with the direction to the source. The width of the minor axis of the ellipse is determined by the declination of the source. At the celestial pole, the ellipse becomes a circle.

As is shown in figure 1.2, an interferometer of a synthesis telescope has an output which is a complex voltage whose amplitude and phase must be recorded. The real and imaginary components of the output are referred to as the cosine and sine, or in-phase and quadrature outputs

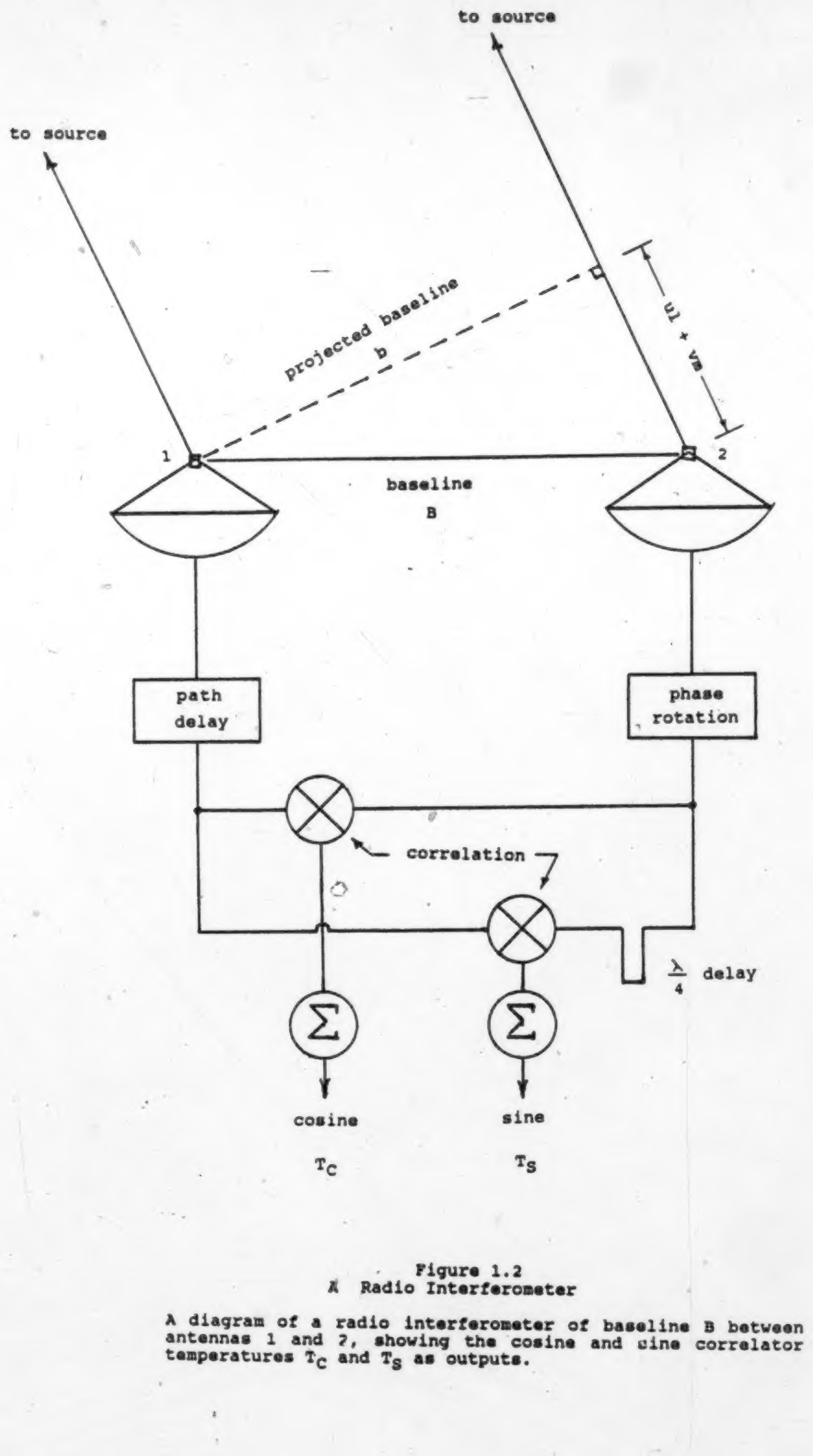

Figure 1.2
A Radio Interferometer

A diagram of a radio interferometer of baseline B between antennas 1 and 2, showing the cosine and sine correlator temperatures T_C and T_S as outputs.

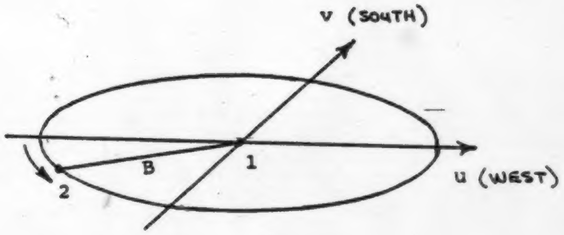

Figure 1.3
The ellipse in the uv Plane

The ellipse traced out in the u-v plane by the projected baseline B between antennas 1 and 2.

respectively. The output or correlation temperature of the cosine and sine channels of the interferometer at any location along the ellipse is given by[4]

$$T_C = \frac{1}{\lambda^2} \int_{4\pi} T_B(l,m)\, A_C(l,m)\, d\omega \qquad 1.5a$$

and

$$T_S = \frac{1}{\lambda^2} \int_{4\pi} T_B(l,m)\, A_S(l,m)\, d\omega \qquad 1.5b$$

where: $T_B(l,m)$ = the brightness temperature of the sky in the direction (l,m), and

A_C and A_S = the cosine and sine effective areas of the interferometer given by equations 1.6a and 1.6b respectively.

$$A_C = 2(A_1 \cdot A_2)^{1/2} \cos \psi \qquad 1.6a$$

$$A_S = 2(A_1 \cdot A_2)^{1/2} \sin \psi \, . \qquad 1.6b$$

The phase delay ψ is held at a value close to zero by the delay system of the telescope. Then $\cos \psi = 1$, and $\sin \psi = 0$, at the field center.

In equation 1.6

ψ = the phase delay, $2\pi(ul + vm)$ between the two antennas at a given point in the u-v plane (see figure 1.1b) and

A_1 and A_2 = the effective areas of each of the individual antennas given by

$$A_1 = A_{1max}F_1(l,m) \qquad 1.7a$$

and

$$A_2 = A_{2max}F_2(l,m) \qquad 1.7b$$

where $F(l,m)$ = the normalized power pattern of each antenna.

If the antennas are identical then

$$A_{1max} = A_{2max} = A_{max} = \frac{\lambda^2}{\iint_{4\pi} F(l,m)\, d\omega} \qquad 1.8$$

or

$$A_{max} = \frac{\lambda^2}{\Omega} \quad . \qquad 1.9$$

As the projected baseline of the interferometer moves around the elliptical track in the u-v plane, the outputs

T_C and T_S are integrated, sampled, and scaled, and then combined using equation 1.10 to form the complex correlation temperature T(u,v) given by equation 1.1.

$$T(u,v) = T_C + j\,T_S \qquad 1.10$$

The calibration of T(u,v) involves observing bright point sources, usually quasars, with the interferometer to obtain the amplitude and phase response to sources of known flux density. In this way, any amplitude or phase variations artificially introduced by the system can be measured and eliminated from the data, provided that calibration is performed sufficiently often.

It is the values of T(u,v) (also called the complex visibility function), that are used to fill the u-v plane prior to performing the transform to obtain the radio brightness distribution of the sky.

To show that equation 1.10 is equivalent to the expression for half of the Fourier transform pair given in equation 1.1, the cosine and sine equivalent areas in equations 1.6a and 1.6b can be rewritten in their complex form

$$A = 2(A_1 \cdot A_2)^{1/2} e^{j\psi} . \qquad 1.11$$

Then using equation 1.11, the sine and cosine correlation temperatures given by equations 1.5a and 1.5b may be rewritten in complex form

$$T = \frac{1}{\lambda^2} \iint T_B(l,m)\ 2(A_1 \cdot A_2)^{1/2} e^{j\psi}\, d\omega \qquad 1.12$$

To express the result in 1.12 for any interferometer spacing in the u-v plane, equation 1.3 is substituted for $d\omega$, and the phase ψ is replaced with equation 1.4. When these expressions have been substituted in equation 1.12, equation 1.1 is the result.

From equations 1.1a, 1.1b, and 1.2 it can be seen that, by taking the Fourier transform of $T(u,v)$, the sky brightness $T_B(l,m)$ is recovered, weighted by the factor

$$\frac{1}{\lambda^2}\ 2[A_1(l,m) \cdot A_2(l,m)]^{1/2}(1-l^2-m^2)^{-1/2} . \qquad 1.13$$

For $T(u,v)$ in equation 1.1 to be valid for a synthesis telescope, two operations must be performed in the interferometer shown in figure 1.2. First, a delay must be added in one arm to equalize the signal path to the correlator. As well, because of the rotation of the Earth, the phase of one of the arms must be rotated in order to keep the response pattern of the interferometer centered on the observation field.

Equation 1.6 represents two sets of fringes displaced 90° from each other with a period 1/b radians on the sky, where b is the projected baseline of the interferometer in wavelengths. The output of the interferometer at any given time is the corresponding Fourier component of the brightness distribution of the sky in that particular orientation. In the course of 12 hours, the baseline of the interferometer has traced out half of the ellipse in the u-v plane shown in figure 1.3, and the orientation of the fringe pattern has rotated through 180°. Figure 1.4 shows the interferometer response pattern, and outputs T_C and T_S if it were used to measure two point sources, a strong one centered in the field, and a weaker source displaced slightly to the side.

It is unnecessary to measure the visibilities on the second half of the ellipse, since the values obtained would be the complex conjugate of those acquired in the first 12

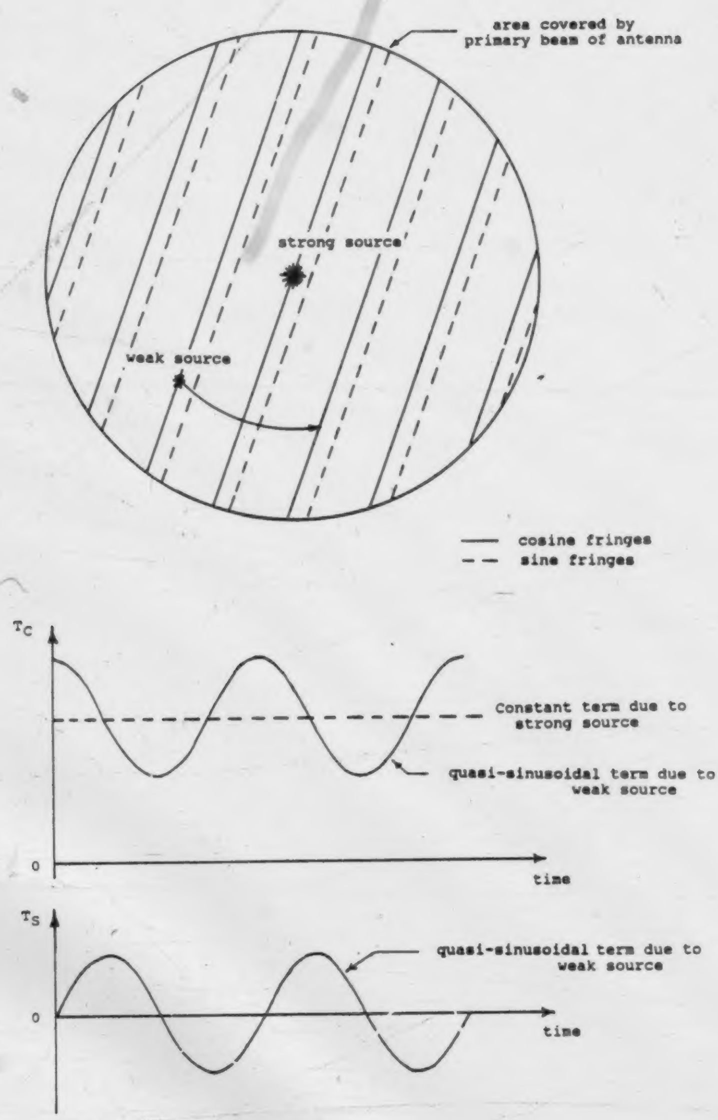

Figure 1.4
Interferometer Output for a Strong and a Weak Radio Source

Diagram showing the cosine and sine fringe patterns on the sky, within the area covered by the primary beam of the individual antennas that make up the interferometer pair. The sine fringes are displaced 90° with respect to the cosine fringes. The outputs of the cosine and sine channels are shown for a strong point source centered in the field, and a weaker one offset from the center. As the earth rotates, the fringe pattern rotates about the field center, which causes the weaker source to travel through the fringes in a CCW direction.

hours of observation. In 12 hours, the rotation of the earth has effectively interchanged the two antennas because it has rotated the interferometer through 180°. Therefore, after an observing run of 12 hours, the spacing of the antennas is changed, and the interferometer response from another track in the u-v plane is measured and recorded. An aperture synthesis telescope usually consists of several antennas. If this is so, the time required to sample T(u,v) over the u-v plane is minimized by being able to form multiple, non-redundant baselines by correlating different pairs of antennas simultaneously.

After the u-v plane has been sampled adequately, the data are gridded into an array suitable for the FFT (Fast Fourier Transform) algorithm. The transform of the u-v data is then calculated, which gives a map of the radio brightness distribution of the sky.

The main advantage of aperture synthesis telescopes compared with other types of radio telescopes is the angular resolution that is obtainable. The resolution of a synthesis telescope is comparable with that of a single antenna whose diameter is the dimension of the longest baseline used. In this way, the very narrow beam of a large diameter antenna can be synthesized with only a fraction of the collecting area being required. In the case of the synthesis telescope at DRAO, an antenna ~ 600 m in diameter is synthesized in 35 days using four antennas which have diameters of ~ 9 m. A fifth antenna is in the process of being integrated into the system, with plans for a sixth and seventh antenna expansion in the near future.

1.3 THE DRAO SYNTHESIS TELESCOPE

With the addition of the fifth antenna, the DRAO Synthesis Telescope consists of an array of five antennas, of which two are fixed, and three are movable on a 300 m track. The five antennas are ~ 9 m paraboloids with an F/D ratio of ~ 0.42, but each antenna varies slightly from these values as a result of being purchased from different sources. Table 1.1 lists the various parameters of each of the five antennas in the synthesis array.

The maximum baseline of the array is 600 m (between the fixed antennas) arranged in an east-west configuration. The track on which the three movable antennas are located occupies the west half of the array, and has seventy observing stations located along its length at regular spacings of 4.286 m. Using earth rotation and four antennas each survey requires 35, 12 hour observing sessions to complete. The telescope operates at 408 MHz and 1420 MHz simultaneously producing maps 7.4° square and

TABLE 1.1 ANTENNA PARAMETERS OF SYNTHESIS TELESCOPE

Antenna	Dia. (m)	F.L. (m)	F/D Ratio	Mesh size (cm)	β (deg)	feedleg		Conditions below antennas
						dia (cm)	config.	
FW	9.14	3.81	0.42	1.59	57.3	8.89	quad	tower, 1/2 track
W	8.53	3.66	0.43	1.59	55.6	15.24	tri	tower, platform, track
5 th	8.53	3.66	0.43	0.95	55.6	15.24	tri	tower, platform, track
E	8.53	3.66	0.43	0.95	55.6	15.24	tri	tower, platform, track
FE	9.14	3.81	0.42	1.59	57.3	8.89	quad	tower

Note: β is the angle formed between the feedleg and the axis of the antenna.

2.1° square with resolutions of 3.5' X 3.5' cosec δ and 1.0' X 1.0' cosec δ respectively, where δ is the declination of the field being surveyed.

1.3.1 SYNTHESIS TELESCOPE SENSITIVITY

A synthesis telescope is made up of pairs of antennas which have their outputs correlated or multiplied to give an output signal proportional to the average product of the voltages from the two component antennas. A schematic of a correlated pair of antennas is shown in figure 1.5. Each pair of antennas has a minimum detectable sine or cosine correlation temperature given by[5].

$$\Delta T_{MIN} = QM \frac{\sqrt{T'_{sys1} \; T'_{sys2}}}{\sqrt{\Delta \nu t} \; \sqrt{\eta'_{t1} \; \eta'_{t2}}} \qquad 1.14$$

where: M = 2 for a direct multiplying correlation receiver,

Q = a factor, usually between 2 and 5, that determines the level above the noise at which one can begin to extract information,

T'_{sys1} and T'_{sys2} = noise temperatures of the antenna-preamplifier combination referred

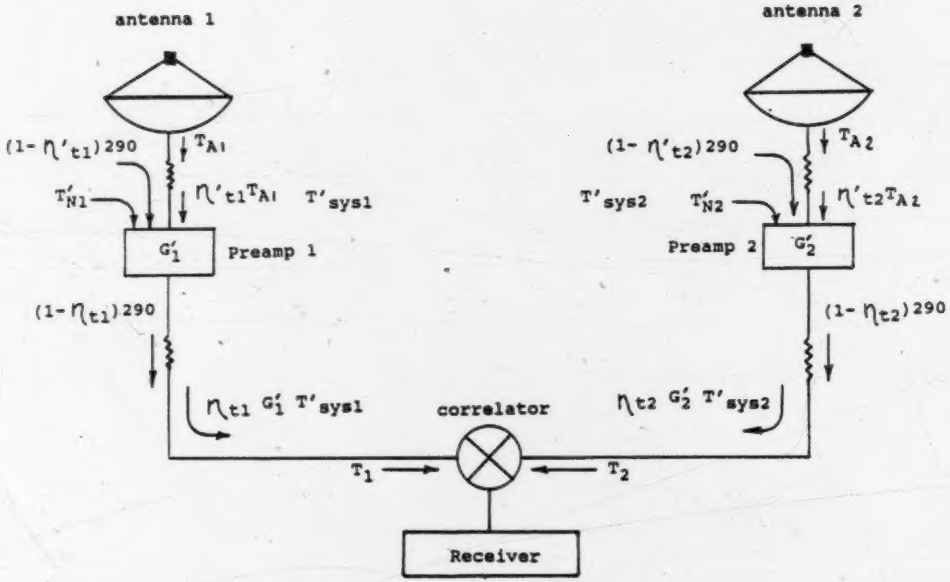

Figure 1.5
Noise Contributions in an Interferometer Pair

Schematic of a correlation telescope or interferometer pair, showing contributions to system noise. The primed values denote contributions referred to the input of the preamplifier, whereas the unprimed quantities refer to contributions to system noise that occur after the preamplifier (Adapted from Christiansen and Högbom[5]).

to the preamplifier inputs,

$\Delta\nu$ = receiver bandwidth in Hz.

t = integration time in seconds, and

η'_{t1} and η'_{t2} = power efficiencies of the transmission lines which connect the antennas to the preamplifiers.

Equation 1.14 assumes that the available powers (T_1 and T_2 in figure 1.5) coming from each antenna-preamplifier half of the system, have been adjusted to be equal, and that the gain of the preamplifiers is high enough so that any noise introduced into the system at a later point can be ignored.

If these conditions are met,

$$T_1 \sim T_{sys1} G'_1 \eta_{t1} \quad \text{and} \quad T_2 \sim T_{sys2} G'_2 \eta_{t2} \qquad 1.16$$

where: η_{t1} and η_{t2} = the transmission line efficiencies that connect the preamplifiers to the receiver,

G'_1 and G'_2 = the gain of each preamplifier, and

$$T'_{sys1} = T_{A1}\eta'_{t1} + (1 - \eta'_{t1})T_{290} + T'_{N1} \qquad 1.16a$$

$$T'_{sys2} = T_{A2}\eta'_{t2} + (1 - \eta'_{t2})T_{290} + T'_{N2} \qquad 1.16b$$

where: T_{A1} and T_{A2} = the antenna temperature of each antenna,

T_{290} = assumed physical temperature of the transmission line between the antenna and preamplifier, and

T'_{N1} and T'_{N2} = the noise temperature of each of the preamplifiers.

The system temperature of the two halves of the interferometer, given by equation 1.16, is made up of 3 components: 1) the loss in the transmission line between the antenna and the preamplifiers η', 2) the noise temperature of the amplifier (T'_N), and 3) the antenna temperature (T_A). If any one of these components is reduced, the sensitivity of the telescope will be improved.

Table 1.2 lists estimates of the contributions to system temperature for the DRAO telescope at 1420 MHz. The telescope operates at both 1420 MHz and 408 MHz, but in this thesis only the performance of the telescope at 1420 MHz is discussed.

TABLE 1.2 ESTIMATES OF THE CONTRIBUTIONS TO SYSTEM NOISE FOR THE DRAO SYNTHESIS TELESCOPE AT 1420 MHz

Receiver Noise	50 K
Galactic Emission	2 K
Cosmic Microwave Background	3 K
Antenna Noise	18 K
Atmosphere (2.2 K at zenith at 1420 MHz, 4.4 K at elevation 30°)	3 K
Total	76 K

1.3.2 LOSS IN THE TRANSMISSION LINE

The amplifiers of the DRAO antennas are mounted directly on the 1420 MHz probes which are located 8.7 cm from the bottom of a 15 cm diameter circular wave guide which clamps to the feed horn. The feed is clamped to the wave guide with a sliding fit to enable focusing. The loss in the waveguide and waveguide-amplifier connection is likely very low, which would give a high value to the transmission line efficiencies η'_{t1} and η'_{t2} in equations 1.16a and 1.16b, which in turn would result in low contributions to system temperature (probably less than 2 K).

1.3.3 NOISE CONTRIBUTIONS FROM THE AMPLIFIERS

The present system temperature of each of the DRAO antennas is about 80 K at 1420 MHz. The 3 stage low noise amplifiers now in use have noise temperatures (T_N) ~ 50 K. There are plans to replace the FET's (field effect transistors) in the amplifiers in the future with HEMT's (high electron mobility transistors) which will result in amplifier noise temperatures of ~ 40 K, a 10 K improvement. If Peltier cooling of the amplifiers is used, receiver noise temperatures of about 20 K to 25 K may be possible. An MSc project on this topic is currently underway at the University of Alberta in the Department of Electrical Engineering. Therefore, in the not so distant future, the system noise due to the noise temperatures of the amplifiers should be greatly reduced.

1.3.4 NOISE DUE TO ANTENNA TEMPERATURE (T_A)

In the radio astronomy situation, the output of an antenna is measured in Kelvin or K, and is referred to as antenna temperature (T_A). Antenna temperature is defined as the temperature a fictitious resistor would have for its thermal noise power per unit bandwidth to equal the power delivered by an antenna, with the resistor replacing the antenna at the input terminals of a noiseless amplifier. The amplifier would be receiving power from the resistor according to equation 1.17 given by Nyquist[6]

$$w = kT \qquad 1.17$$

where: w = spectral power in watts Hz^{-1},

k = Boltzmann's constant, and

T = absolute temperature K,
(antenna temperature T_A in this case).

The antenna temperature may be found for any single antenna by evaluating

$$T_A = \frac{1}{\Omega} \int_{4\pi} F(\rho, \phi)\, T(\rho, \phi)\, d\omega \qquad 1.18$$

where: $F(\rho, \phi)$ = the normalized power response or polar diagram of the antenna, with $F(0,0) = 1.0$,

$T(\rho, \phi)$ = the temperature of the source in the direction (ρ, ϕ), and

Ω = the antenna solid angle.

The solid angle of an antenna (Ω) is a measure of its ability to concentrate radiation and is defined as

$$\Omega = \int_{4\pi} F(\rho, \phi)\, d\omega \qquad 1.19$$

Using equation 1.19, the gain G, of an antenna is given by

$$G = \frac{4\pi}{\Omega} \qquad 1.20$$

which is a measure of how much better an antenna performs than an isotropic radiator.

When equation 1.18 is evaluated for one of the 9 m antennas at DRAO, the contributions to antenna temperature are from three separate regions, which are illustrated in figure 1.6.

In region 1, the antenna receives radiation from the sky (extraterrestial radio sources), and the atmosphere. In the spillover region (region 2), energy from the ground is radiated directly into the feed at the focus of the antenna. This is undesirable, since it contaminates the true signal which the antenna receives from the location in the sky that it is pointed at. As well as direct radiation from the ground, the antenna receives ground radiation which is scattered off the feedlegs before entering the feed. Mathematically, the antenna temperature due to radiation coming from the spillover region is expressed by

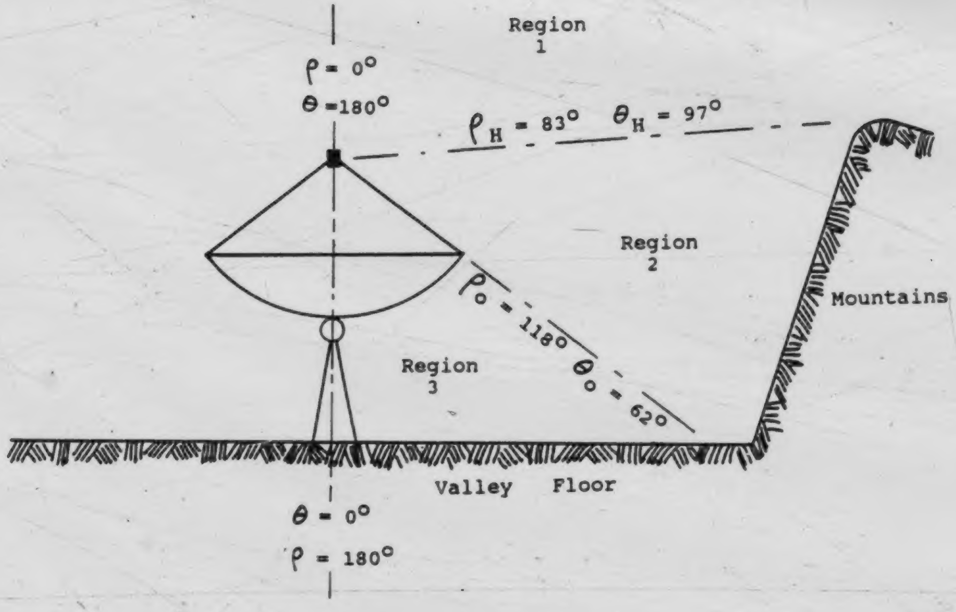

Figure 1.6
Regions that Contribute to Antenna Temperature

A drawing of an antenna showing the three separate regions that contribute to the antenna temperature. In this diagram, two coordinate systems are shown. Angles in the coordinate system centered on the main beam of the antenna have values of ρ . As well, the coordinate system centered on the power pattern of the feed is given and has angles represented by θ .

$$T_S = T_G \frac{\int_{\rho_H}^{\rho_o} F(\rho) \sin\rho \, d\rho}{\int_0^{\pi} F(\rho) \sin\rho \, d\rho} \qquad 1.21$$

where: $F(\rho)$ = the power pattern of the antenna,

T_G = the ground temperature,

ρ_o = the semi-angle of the antenna, and

ρ_H = the angle of the horizon.

Circular symmetry is assumed for simplicity, and the ground temperature is assumed to be independant of direction.

The integral in the denominator of equation 1.21 is the total solid angle of the antenna, and is equivalent to equation 1.19. When the antenna is pointed at the zenith, the integral in the numerator of equation 1.21, sums the solid angle of the antenna from its edge to the horizon. At DRAO the horizon is formed by the mountains which surround the site of the telescope.

Region 3 of figure 1.6 contributes to antenna temperature by two mechanisms. The first is leakage of ground radiation though the mesh of the antenna into the feed, and secondly, the feed receives energy which is diffracted around the rim of the antenna. As in the spillover region, the antenna temperature resulting from leakage and diffraction in region 3 is expressed as

$$T_{LD} = T_G \frac{\int_{\rho_0}^{\pi} F(\rho) \sin\rho \, d\rho}{\int_{0}^{\pi} F(\rho) \sin\rho \, d\rho} \qquad 1.22$$

where: T_{LD} = antenna temperature due to leakage through the mesh and diffraction around the rim of the antenna.

1.4 TOPICS OF THESIS

In any sophisticated instrument that is designed and constructed, continual improvements are made by modification and redesign of its various parts and subsystems. The synthesis telescope at DRAO is no exception to this process. The first three chapters of this thesis focus on improving the sensitivity of the telescope by reducing the antenna temperature of the individual elements that form the array.

Theoretical calculations for the antennas of the synthesis telescope predicted that the antenna temperature at the zenith should be about 19.8 ± 2.5 K, while an antenna temperature = 25.9 ± 2.5 K was measured in 1980 for the far east antenna. Prior to the work described in this thesis the discrepancy between these two values had not been accounted for. Contributions to antenna temperature from spillover and scatter from the feedlegs were thought to make up most of this difference.

In an effort to characterize the effects of spillover and feedleg scatter, and to account for the discrepancy between the theoretical and measured values of antenna temperature, the response pattern of the FE antenna was measured in July and August of 1986. These measurements furnish the values of $F(\rho, \phi)$ which are needed in equation 1.18. By assuming values for the ground temperature $T(\rho, \phi)$, equation 1.18 can be used to calculate a direct value of antenna temperature.

As well, the response pattern enables separate estimates of antenna temperature to be calculated for regions 2 and 3 shown in figure 1.6 by evaluating equations 1.21 and 1.22 between the appropriate limits. These measurements and calculations have shown that the effects of spillover and feedleg scatter are significant contributors to antenna temperature for the DRAO synthesis antennas.

Currently, the system noise temperature of the antennas which make up the synthesis telescope is about 80 K. As amplifiers with lower noise become available, contributions to system noise from sources such as spillover and feedleg scatter become more significant. As a result, effort should be expended to reduce these sources as well.

With this in mind, an experiment was performed on the fifth antenna to try to reduce its antenna temperature. The antenna was modified by adding a cylindrical fence around its rim, which had the effect of reducing antenna temperature due to spillover. As well, wedges with serrated leading edges were added to the feedlegs to alter their shape in cross section, which reduced antenna temperature due to feedleg scatter. Individual measurements of antenna temperature were obtained with the fence and the feedleg modifications added separately to the antenna. Measurements of antenna temperature were also obtained with both modifications on the antenna at the same time. In each case a significant reduction of antenna temperature was observed. Chapters 2 and 3 of the thesis discuss the measurement of the response pattern of the FE antenna along with the experiments that were performed to reduce the value of antenna temperature of the fifth antenna.

Chapters 4 to 6 of the thesis discuss an observation of S183 using the synthesis telescope at DRAO. It is an extended radio source at $l = 123.2^{\circ}$, $b = +2.9^{\circ}$, which is also visible as a faint optical nebula on the red print of the Palomar Observatory Sky Survey (POSS). Previous radio surveys of this object have not shown conclusively whether this object is a supernova remnant or an HII region. For this reason, a survey using the DRAO synthesis telescope was undertaken. The 408 MHz and 1420 MHz continuum maps from the synthesis telescope have better resolution than any of the previous surveys of this object. The information from these two maps has shown that S183 is an HII region, and not a supernova remnant as has been previously suggested in the literature.

CHAPTER 2

DETERMINATION OF ANTENNA TEMPERATURE

2.1 INDIVIDUAL CONTRIBUTORS TO ANTENNA TEMPERATURE

Prior to 1986, attempts were made to account for the measured value of antenna temperature = 25.9 ± 2.5 K[7] for the far east antenna by considering the individual contributors:

1. Atmosphere
2. Sky
3. Spillover
4. Mesh leakage
5. Diffraction.

It was hoped that by examining each of the contributors in turn, a theoretical estimate of antenna temperature would match the measured value. An agreement between the theoretical and measured values of antenna temperature would indicate that the response pattern of the antenna was sufficiently understood to allow attempts at selective reduction of one or more of the sources of noise listed above. A discussion of each contribution to the theoretical antenna temperature follows.

1) Atmospheric Noise Contribution (2.2 K)

This source arises due to the atmosphere attenuating and scattering extraterrestial radio signals. Its effect becomes more significant as the zenith angle increases, assuming a plane parallel slab of atmosphere, varying as the secant of the zenith angle. Figure 2.1 shows the antenna temperature as a function of antenna zenith angle[8]. From the plot at 1.4 GHz, antenna temperature due to atmospheric absorption is about 2.2 ± 0.3 K.

2) Sky Contribution (5 K)

The sky contribution comes from radiation emitted from the 3 K microwave background, ionized interstellar gas, synchrotron radiation and other interstellar sources. Figure 2.1 also shows the sky radiation minimum (0.5 K) and maximum (11 K), occurring at the galactic poles and galactic center respectively[8]. A value for the sky contribution to antenna temperature is assumed to be ~ 5 ± 2.0 K, a level midway between these two limits.

3) Spillover contribution (6.1 K)

Of the five sources considered which contribute to the theoretical antenna temperature, this source was thought to be the largest, and may be explained as follows. If the

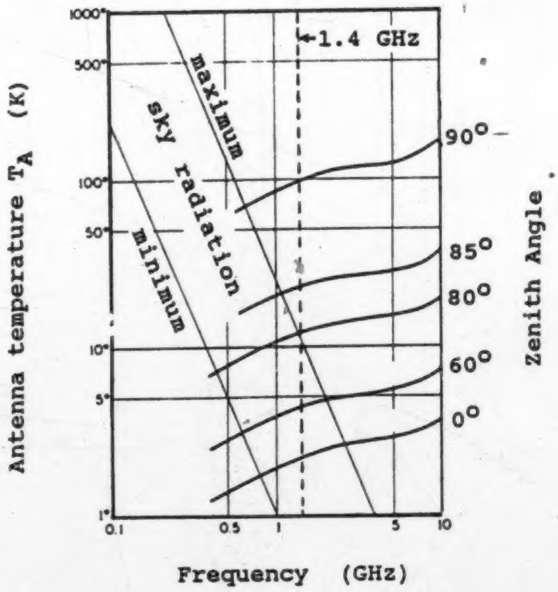

Figure 2.1
Sky and Atmospheric Noise Contributions
to Antenna Temperature

Plot showing antenna temperature T_A due to atmosphere and cosmic noise as a function of frequency (Adapted from Jordan and Balmain[8]).

receiver of an antenna is replaced by a transmitter that radiates into the dish through the feed, not all of the energy will fall on the antenna. The portion of radiation that is not intercepted by the dish is called spillover, and the receiver will receive radiation from these same angles. Since radio telescopes point to the sky, much of the spillover region of an antenna will fall on the ground, which is a thermal noise source at ~ 300 K.

Mathematically, the spillover temperature is defined by equation 1.21, where $F(\rho, \phi)$ is the power pattern of the antenna. Equation 1.21 may be modified by substituting the power pattern of the feed[9] $G(\theta, \phi)$ in place of $F(\rho, \phi)$. It then can be numerically evaluated, assuming geometric optics, to obtain antenna temperature. Table 2.1 is a listing of this calculation from $\theta = 62^\circ$ to $\theta = 97^\circ$, which are the angles to the edge of the antenna and to the horizon, respectively, as seen from the feed. The high horizon is the result of the mountains which surround the site of the observatory. $\theta = 0^\circ$ is coincident with the maximum of the power pattern of the feed and falls at the center of the parabolic reflector (see figure 1.6).

In table 2.1, the cumulative antenna temperature (CuT_A) was calculated using

TABLE 2.1 CALCULATION OF T_A DUE TO SPILLOVER

θ	$G(\theta)$	$\Delta\omega$	$\Delta\Omega$	$Cu\Delta\Omega$	CuT_A
		$2\pi \sin(\theta)\Delta\theta$	$F(\theta)\Delta\omega$	$\Sigma F(\theta)\Delta\omega$	
	$(\times 10^{-2})$		$(\times 10^{-3})$	$(\times 10^{-3})$	$(^{\circ}K)$
62–63°	2.670	0.098	2.609	2.609	0.60
64	2.350	0.099	2.316	4.925	1.13
65	1.910	0.099	1.898	6.823	1.56
66	1.820	0.100	1.823	8.646	1.98
67	1.700	0.101	1.716	10.362	2.37
68	1.550	0.102	1.576	11.937	2.73
69	1.380	0.102	1.413	13.350	3.06
70	1.120	0.103	1.154	14.504	3.32
71	1.000	0.104	1.037	15.541	3.56
72	0.891	0.104	0.929	16.470	3.77
73	0.784	0.105	0.822	17.292	3.96
74	0.741	0.105	0.781	18.073	4.14
75	0.708	0.106	0.750	18.823	4.31
76	0.676	0.106	0.719	19.542	4.48
77	0.631	0.107	0.674	20.217	4.63
78	0.589	0.107	0.632	20.848	4.77
79	0.562	0.108	0.605	21.453	4.91
80	0.537	0.108	0.580	22.033	5.05
81	0.478	0.108	0.518	22.551	5.16
82	0.447	0.109	0.485	23.036	5.28
83	0.398	0.109	0.433	23.469	5.37
84	0.363	0.109	0.396	23.865	5.47
85	0.316	0.109	0.345	24.210	5.54
86	0.295	0.109	0.323	24.533	5.62
87	0.269	0.110	0.295	24.828	5.69
88	0.234	0.110	0.256	25.084	5.74
89	0.219	0.110	0.240	25.324	5.80
90	0.200	0.110	0.219	25.543	5.85
91	0.178	0.110	0.195	25.739	5.89
92	0.170	0.110	0.186	25.925	5.94
93	0.151	0.110	0.165	26.090	5.97
94	0.145	0.109	0.159	26.249	6.01
95	0.138	0.109	0.151	26.400	6.05
96	0.135	0.109	0.147	26.547	6.08
97	0.132	0.109	0.144	26.691	6.11

$$CuT_A = \frac{Cu\Delta\Omega(300)}{\Omega_F} \qquad 2.1$$

where: $Cu\Delta\Omega$ = the cumulative solid angle of the feed starting at $\theta = 62^{\circ}$,

Ω_F = the total solid angle of the feed (1.31 steradians obtained by integrating the feed pattern given by Veidt[9]), and

300 K = the assumed ground temperature in the spillover region.

The last column in the bottom line of table 2.1 shows that the contribution to antenna temperature due to spillover using the feed power pattern in equation 1.21 is about 6.1 K. The error in this estimate is probably about ± 1.0 K.

4) Mesh Leakage Contribution (5.9 K)

The antennas of the synthesis telescope are surfaced with expanded aluminum sheeting. From table 1.1, the mesh size of the far east antenna is 1.59 cm, with an approximate diameter of 0.2 cm for the wire size in the mesh. Using a nomogram for transmission through a grid of wires[10], a value of -17 dB was obtained for the power leaking through the mesh from the ground. If the ground temperature is assumed to be 300 K, the antenna temperature due to mesh leakage is found from

$$T_{A\ \mathrm{Mesh}} = \frac{\Omega_A}{\Omega_T}(300)(10^{-17/10}) \qquad 2.2$$

where: Ω_A = the solid angle of the feed pattern that falls on the surface of the antenna (1.28 steradians), and

Ω_T = the total solid angle of the feed (1.31 steradians).

Using equation 2.2, a value of 5.9 K is obtained for the contribution to antenna temperature due to mesh leakage, with an estimated error of ± 1.0 K. This would likely be an upper bound, since the support structure for the surface of the antenna, and the steel tower located under the antenna would tend to reduce the amount of leakage.

5) Diffraction Contribution (0.6 K)

The last contribution to be considered is the diffraction of energy around the rim of the antenna from the region below the antenna. It may be approximated by assuming that the rim of the antenna acts like an infinite semi-plane which is placed between a receiver (the feed) and a transmitter (the ground at 300 K). Figure 2.2a shows the geometry of an infinite semi-plane EPY (perpendicular to the page) placed between the transmitter G and the receiver F. The height of the plane above the direct line of sight between the receiver and transmitter is EP or h. Figure 2.2b[11] shows the amplitude of the field strength caused by the infinite semi-plane as a function of the variable v, which is given by

$$v = \pm(h)\sqrt{(2/\lambda)\,(1/d_1 + 1/d_2)} \qquad 2.3$$

where: h = the height of the infinite semi-plane above (v is negative) or below (v is positive) the direct line of sight between the transmitter and receiver,

λ = the wavelength of observation,

d_1 = the distance along the line of sight from the receiver to the infinite semi-plane, and

d_2 = the distance along the line of sight from the transmitter to the infinite semi-plane.

If the geometry of figure 2.2a is superimposed on the

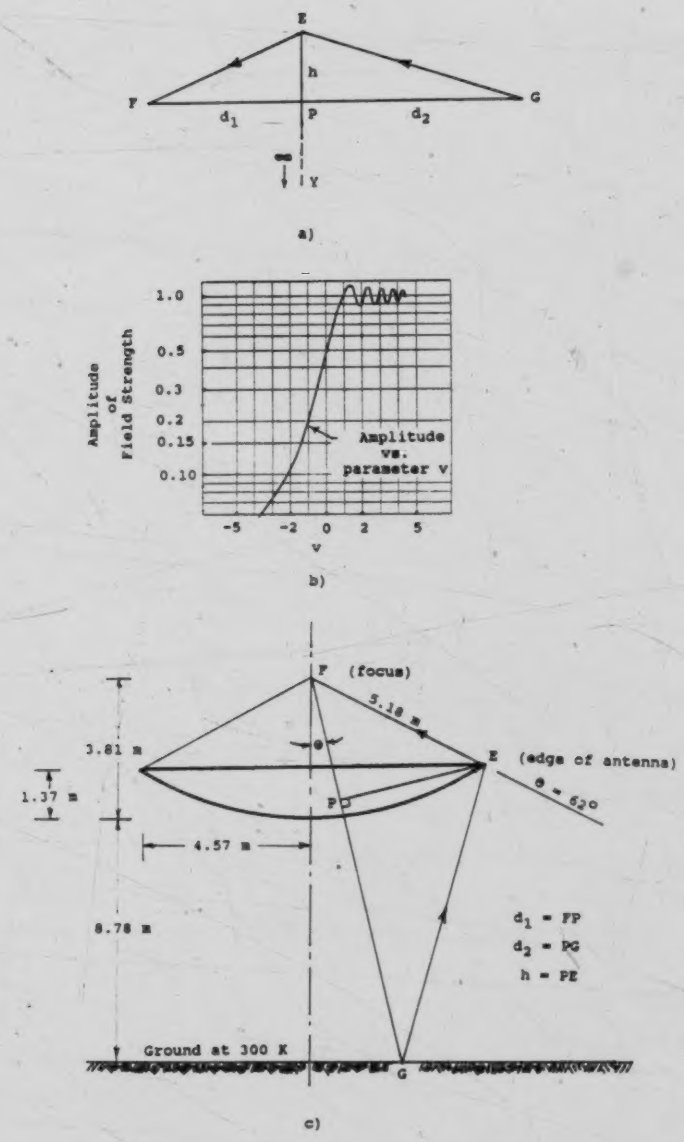

a)

b)

c)

Figure 2.2
Diffraction Around the Rim of the Far East Antenna

a) Geometry of infinite semi-plane EPY inserted between a transmitter G, and a receiver F.

b) Amplitude of field strength produced by an infinite semi-plane EPY as a function of v (Adapted from David and Voge[11]).

c) the FE antenna pointed at the zenith, with the geometry of the infinite semi-plane (shown in fig. 2.2a) superimposed, allowing the approximation of the field strength as seen by the feed due to diffraction of the ground radiation at G around the rim of the antenna E.

far east antenna, figure 2.2c is the result. In this figure, the ground G at 300 K is the transmitter and the receiver is at F, the focus of the antenna. The antenna is approximated by the infinite semi-plane. At a given angle θ, an annulus of ground of radius θ and width $\Delta\theta$ will radiate energy which will diffract around the rim of the antenna at E. The attenuation of the field by the antenna can then be found by calculating the parameter v for the angle θ using equation 2.3. For the case of the far east antenna, d_1, d_2, and h in equation 2.3 are given by

$$d_1 = 5.18 \cos(62^\circ - \theta) \qquad 2.4$$

$$d_2 = 12.58 \sqrt{\tan^2\theta + 1} - d_1 \qquad 2.5$$

$$h = 5.18 \sin(62^\circ - \theta) \qquad 2.6$$

where: θ = the angle from the maximum power response of the feed in degrees.

Table 2.2 lists the results of a numerical calculation of diffraction using equations 2.3 to 2.6.

TABLE 2.2 CALCULATION OF T_A DUE TO DIFFRACTION

θ	d_1	d_2	h	v	λ	CuT_A
62-61	5.18	20.79	0.05	-0.07	0.47	0.131
60	5.18	20.00	0.14	-0.21	0.42	0.234
59	5.18	19.27	0.23	-0.34	0.37	0.315
58	5.17	18.59	0.32	-0.48	0.33	0.377
57	5.16	17.95	0.41	-0.62	0.29	0.425
56	5.16	17.36	0.50	-0.77	0.25	0.461
55	5.15	16.80	0.59	-0.91	0.22	0.488
54	5.14	16.29	0.68	-1.05	0.19	0.509
53	5.12	15.80	0.77	-1.20	0.17	0.524
52	5.11	15.34	0.85	-1.34	0.15	0.536
51	5.09	14.91	0.94	-1.49	0.13	0.546
50	5.08	14.51	1.03	-1.64	0.12	0.553
49	5.06	14.13	1.12	-1.79	0.11	0.560
48	5.04	13.78	1.21	-1.94	0.11	0.566
47	5.01	13.45	1.30	-2.09	0.11	0.572
46	4.99	13.13	1.38	-2.24	0.10	0.576
45	4.97	12.84	1.47	-2.39	0.09	0.581
44	4.94	12.56	1.56	-2.55	0.09	0.584
43	4.91	12.30	1.64	-2.70	0.08	0.587
42	4.88	12.06	1.73	-2.86	0.08	0.590
41	4.85	11.83	1.81	-3.01	0.07	0.593
40	4.82	11.62	1.90	-3.17	0.07	0.595
39	4.79	11.42	1.98	-3.32	0.07	0.597
38	4.75	11.23	2.07	-3.48	0.06	0.599
37	4.71	11.05	2.15	-3.64	0.06	0.600
36	4.68	10.89	2.23	-3.80	0.06	0.601
35	4.64	10.73	2.31	-3.95	0.06	0.603
34	4.59	10.59	2.39	-4.11	0.05	0.604
33	4.55	10.46	2.47	-4.27	0.05	0.605
32	4.51	10.34	2.55	-4.43	0.05	0.606
31	4.46	10.22	2.63	-4.59	0.05	0.607
30	4.42	10.12	2.71	-4.75	0.05	0.607
29	4.37	10.03	2.78	-4.91	0.05	0.608
28	4.32	9.94	2.86	-5.07	0.04	0.609
27	4.27	9.86	2.93	-5.23	0.04	0.609
26	4.22	9.79	3.01	-5.39	0.04	0.610
25	4.16	9.73	3.08	-5.56	0.04	0.610
24	4.11	9.67	3.15	-5.72	0.04	0.611
23	4.05	9.62	3.22	-5.88	0.04	0.611
22	4.00	9.58	3.30	-6.04	0.04	0.611
21	3.94	9.55	3.36	-6.20	0.04	0.612
20	3.88	9.52	3.43	-6.37	0.04	0.612
19	3.82	9.50	3.50	-6.53	0.03	0.612
18	3.76	9.48	3.57	-6.69	0.03	0.612
17	3.69	9.47	3.63	-6.86	0.03	0.613
16	3.63	9.47	3.69	-7.02	0.03	0.613
15	3.57	9.47	3.76	-7.19	0.03	0.613
14	3.50	9.48	3.82	-7.36	0.03	0.613
13	3.43	9.49	3.88	-7.52	0.03	0.613
12	3.36	9.51	3.94	-7.69	0.03	0.613
11	3.29	9.53	4.00	-7.86	0.03	0.614
10	3.22	9.56	4.05	-8.04	0.03	0.614
9	3.15	9.59	4.11	-8.21	0.03	0.614
8	3.08	9.63	4.16	-8.39	0.03	0.614
7	3.01	9.68	4.22	-8.57	0.03	0.614
6	2.93	9.73	4.27	-8.75	0.03	0.614
5	2.86	9.78	4.32	-8.94	0.03	0.614
4	2.78	9.84	4.37	-9.13	0.02	0.614
3	2.71	9.90	4.42	-9.33	0.02	0.614
2	2.63	9.97	4.46	-9.53	0.02	0.614
1	2.55	10.04	4.51	-9.73	0.02	0.614
0	2.47	10.12	4.55	-9.94	0.02	0.614

For $-2.0 \leq v \leq 0.0$, the amplitude A of the field is given by equation 2.7, which is a 3rd order polynomial fitted to the curve in figure 2.2b between v = -2.0 to 0.0.

$$A = -4.17 \times 10^{-3}v^3 + 0.112v^2 - 0.403v + 0.5 \quad 2.7$$

For values of $v \leq -2.0$, the amplitude is given by[11]

$$A = -1(0.225/v) \quad 2.8$$

The incremental antenna temperature is given by

$$dT_A = \frac{[2\pi \sin \theta]}{1.31}[300][A(\theta)]^2 F(62^\circ)\, d\theta \quad 2.9$$

where:
1.31 = the solid angle of the feed for far east antenna,
300 = the assumed ground temperature in Kelvin,
$A(\theta)$ = the amplitude of the field diffracted by the rim of the antenna, and
$F(62^\circ)$ = the value for the power pattern of

the feed at the edge of the antenna (2.67×10^{-2} from table 2.1), and

$d\theta = 1^{\circ} = 1/57.3$ radian.

From table 2.2, using the method just described, a value of ~ 0.6 K is found for the contribution to antenna temperature (with a probable uncertainty of ± 0.1 K) from diffraction of energy around the rim of the antenna. It is the smallest contribution of the five considered.

When the above contributions are totaled in table 2.3, the theoretical estimate for antenna temperature for the far east antenna is 19.8 ± 2.5 K, which is 6 K lower than the measured value of antenna temperature, 25.9 ± 2.5 K.

2.2 DATA COLLECTION AND PRESENTATION

To explain the ~ 6 K discrepancy between the measured and theoretically calculated values of antenna temperature, the response pattern of the far east antenna was measured in July 1986. The data obtained give values for $F(\rho, \phi)$ in equation 1.18, which is used to calculate antenna temperature. The measured power pattern also allows a separate calculation of antenna temperature due to spillover, mesh leakage and diffraction, as well as an

TABLE 2.3 THEORETICAL VALUES FOR THE CONTRIBUTORS TO T_A (In Kelvin)

1.	Atmosphere	2.2 ± 0.3
2.	Sky	5.0 ± 2.0
3.	Spillover	6.1 ± 1.0
4.	Mesh leakage	5.9 ± 1.0
5.	Diffraction	0.6 ± 0.1

Theoretical T_A = 19.8 ± 2.5 K

estimate of antenna temperature due to feedleg scatter.

2.2.1 THE EXPERIMENTAL MEASUREMENTS

The far east antenna was chosen for this measurement because its location was relatively free of buildings, fences, and other obstructions in comparison to the other antennas of the array. The response pattern was measured by placing a point source of radio waves in the far field and scanning the antenna over the sky while recording the received power. A very similar method was used by Higgs[12] to measure the antenna characteristics of the Dwingeloo Radio Telescope at 820 MHz.

In order for the method to work, the transmitter must be at a distance greater than the minimum distance required for far field conditions. This distance is given by[13]

$$d = 2(D^2)/\lambda \qquad 2.10$$

where: D = the diameter of the antenna (9.14 m for the far east antenna, and

λ = the wavelength of observation.

Using equation 2.10, far field conditions begin at 792 m for the far east antenna operating at 1420 MHz.

A suitable hill top for the site of the transmitter was chosen to the east and slightly south of the far east antenna. The factors considered in choosing this location were: 1) it must be in the far field of the antenna, 2) the vertical angle as seen from the antenna should be as large as possible, to minimize the ground reflection, and 3) it should be reasonably accessible. The chosen hill top was a compromise among the above conditions, being at a distance of 810 m (just into the far field), with a vertical angle of ~ 12°, and having relatively easy access.

To minimize the effect of the ground reflection, vertical polarization was chosen for the transmitter. An estimate of the reflection coefficient in this case is about 0.15[14], which would make the reflected power approximately 16.5 dB below the power received from the direct wave, thus minimizing any distortion in the measured antenna pattern caused by the reflected wave.

The transmitter consisted of a stable oscillator generating about 200 mW, which was fed through a 10 dB attenuator to a rectangular horn for transmission. The oscillator, horn, and batteries which powered the transmitter, were mounted in a dead tree on the hill top about 3.5 m above the ground. In order to avoid saturating the electronic system of the telescope, the FET front end amplifier had to be disconnected. The signal from the receiving feed horn was fed directly into the bandpass filter in front of the mixer (located in the focus box). The far east antenna was configured to receive right hand circular polarization for these measurements.

The signal was recorded using a spectrum analyzer with a bandwidth of 300 KHz centered on the 30 MHz IF of the far east antenna. A 300 KHz bandwidth was chosen to minimize any effects of drift in the measuring system. Periodically, the antenna was re-positioned on the transmitter, to allow the spectrum analyzer to be recentered on the IF, which eliminated any need to correct the data for drift. A 0 to 1 volt analog output on the spectrum analyzer was connected to a chart recorder to make a permanent record of the data for later analysis. Using this system, a dynamic range of 60 dB was achieved. Figure 2.3 shows a schematic of the equipment configuration used to measure the power pattern of the far east antenna.

The antennas of the synthesis telescope are designed with equatorial mounts which made it convenient to gather the data by scanning in right ascension (RA) along lines of

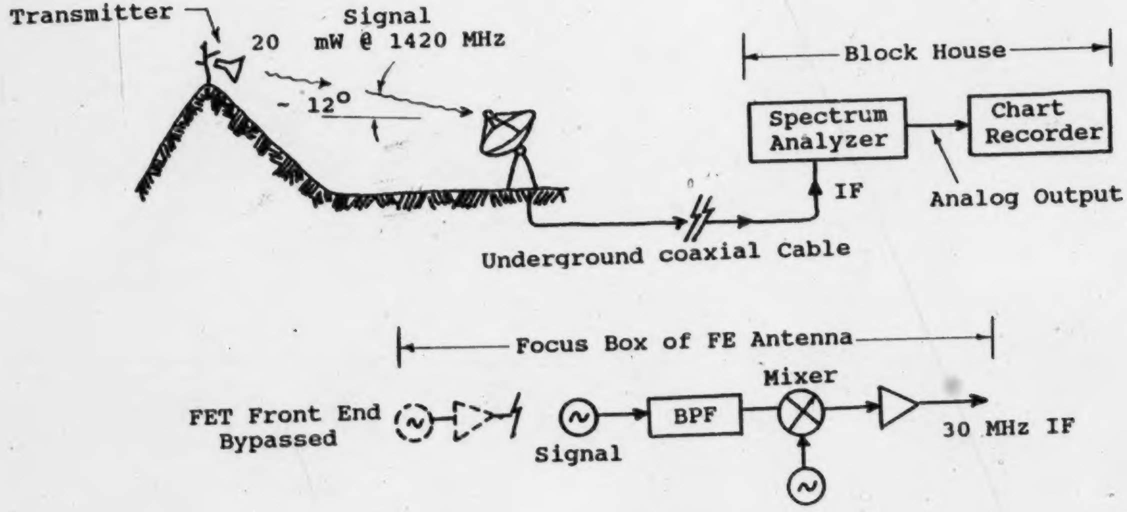

Figure 2.3
Configuration of the Equipment For Measuring the Power Pattern of the Far East Antenna

A signal from a 200mW oscillator was fed through a 10 dB attenuator to a horn and transmitted with vertical polarization. The signal was recorded using a spectrum analyzer with a bandwidth of 300 KHz centered on the 30 MHz IF.

constant declination (DEC). The half-power beam width (HPBW) of the antennas is 1.75°, which requires sampling the power pattern at a spacing of 0.875° to fulfill the Nyquist criterion. For convenience, a spacing of 0.75° in DEC was chosen for the scans along RA. The power response of the antenna was recorded over the whole sky using this spacing, with the horizon limit switches determining the east and west end points of each scan. The north pole limit switch was set to DEC = +84.25°, preventing any data collection within a radius of ~ 6° of the north pole. The scans were obtained in alternate directions, from west to east, then east to west, which minimized the time required to collect the data. A sensor, which was capable of discerning the scanning direction, was attached to the RA read-out selsyn connected to the far east antenna. It was used to activate an event marker which fixed the location of each hour of RA on the chart. Figure 2.4 shows a section of chart paper which contains a scan through the transmitter, located at RA = $19^h\ 13.7^m$, DEC = +1.47°, with 0^h on the meridian.

After the sky was scanned completely, a process requiring three days to complete, the strip charts were digitized, with the resulting data stored in a separate file for each scan. Each point in the digitization process was stored as a separate record consisting of 3 elements,

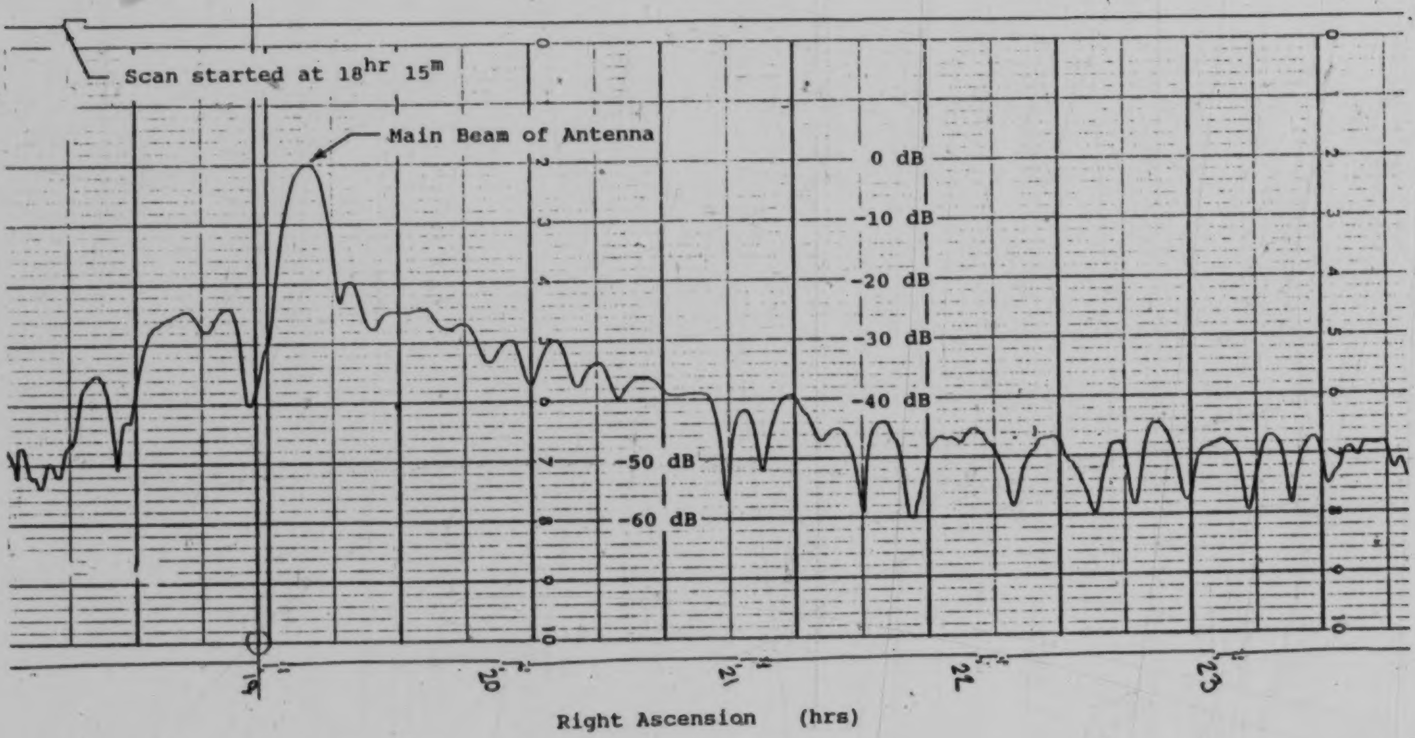

Figure 2.4
Scan Through the Main Beam

Strip chart showing a portion of a scan through the transmitter at DEC = +1.47°. Dynamic range is 60 dB.

RA, DEC, and received power in dB. About 20 % of the strip charts were digitized at DRAO on the VAX system; the remainder were done on the University of Alberta MTS system. The software for digitizing charts at DRAO was written by Dr. L.A. Higgs. The software used at the University of Alberta is part of the MTS system.

The portion of data which was digitized on the MTS system, was written to a tape and transferred to a VAX computer located in the Department of Applied Science in Medicine, at the University of Alberta. It was then combined with the data which were digitized at DRAO, with the help of Robert Morse, to form a single file consisting of approximately 69,000 data points. The complete file was then taken back to the VAX system at DRAO on a magnetic tape for further processing. Figure 2.5 shows a summary of the data reduction process from the raw data on the strip charts, to a single file containing the power pattern of the far east antenna in the RA-DEC coordinate system.

2.2.2 ACCURACY OF THE MEASUREMENTS

When estimating the accuracy of the data in the measured power pattern, several potential sources of error should be considered. Inaccuracies in the data are the result of the combined effects of the transmitter, spectrum

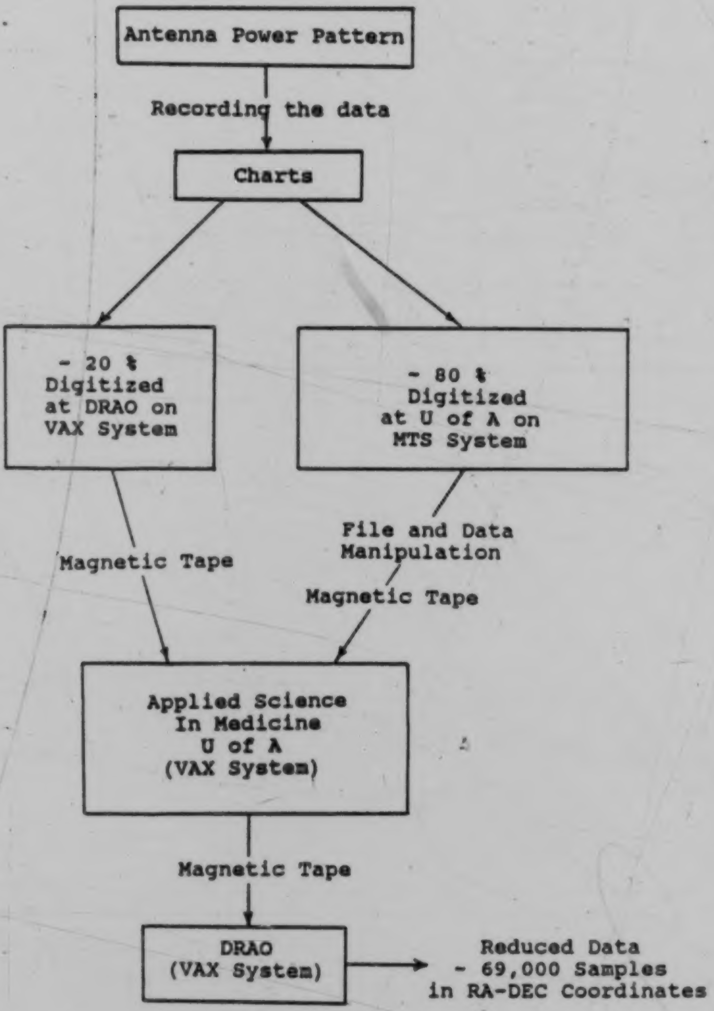

Figure 2.5

Flow Chart of Data Reduction Process.

analyzer, and chart recorder which were used in the measuring and recording process.

a) The Transmitter

The transmitter on the hill consisted of an oscillator powered by a 12 volt automotive battery. The voltage was regulated before it was applied to the oscillator to stabilize the power output. The frequency was governed by a tuned cavity which resulted in a very stable operating point at 1420 MHz. The power output, however, was likely not as stable as the frequency, due to drift of the regulation point with temperature changes throughout the day.

b) The Spectrum Analyzer

The signal was received by a spectrum analyzer centered on the 30 MHz IF, and operated with a 300 KHz bandwidth. The wide bandwidth was selected to minimize the effects of any drift in the center frequency of the spectrum analyzer, but errors occur if the passband is not flat over the frequency range of the drift.

c) The Chart Recorder

A servo chart recorder with an accuracy of ± 0.5 percent of full scale was used to make a permanent record of the data. This imposed a ± 0.5 dB accuracy limit on the data, since full scale on the chart corresponded to 100 dB.

To minimize the effects of any drift in the equipment, the antenna was periodically redirected to the transmitter so that the center frequency of the spectrum analyzer could be reset to 30 MHz. At the same time the chart recorder was rezeroed to compensate for any drift in the power levels. The system was readjusted on average every 5.6 scans, and the offsets in both the frequency and power levels were recorded. The 1 σ levels for the frequency and power offsets were 26 KHz and 0.26 dB respectively. It should be noted that any error caused by the frequency drift would be included in the ± 0.26 dB error found for the power levels.

The above shows that the readjustment process was performed often enough to limit the drift errors to less than half of the accuracy specification of the chart recorder.

d) Polarization and Ground Reflection

As stated previously, vertical polarization was used to minimize the ground reflection. However, the antenna received circular polarization, which has given the scatter lobes from the feedlegs a polarization dependence. The implications of this are discussed in section 3.3.1. For the rest of the antenna pattern any effect due to random polarization, resulting from reflections, should average out over the numerous lobes measured.

The reflection coefficient of the ground has been estimated to be about 0.15, putting levels of any reflected power ~ 16.5 dB below the direct wave. The result recorded for a given orientation of the antenna is a vector sum of the direct and reflected waves at the receiver. Any effects should average out over the measured antenna pattern.

e) Miscellaneous Sources of Errors

Adjacent scans were performed in alternate directions which has resulted in a slight offset due to backlash in the system. This was found to be ~ 0.45° by measuring the offset of the lobes in a scan which was taken in both directions. The offset corresponds to about 0.9 pixel in the east-west direction of the RA-DEC map. Since a 1° Gaussian was used in the gridding process, the effect has had little influence on the final map.

The Sun added 1.5 dB to the data whenever the main beam of the antenna passed over it. But since this condition occurred infrequently, it has been ignored.

A check on the time constant of the receiver was performed while obtaining the data. This was accomplished by pointing the antenna at the transmitter and recording the response of the system as the transmitter was turned off. It was found that the system could respond to a 60 dB change in power level in about 0.15 pixel in the RA-DEC map given the scanning rate. The response was fast enough to eliminate any concerns that fine structure in the antenna pattern was being lost because of the scanning speed.

Finally, the digitization process could be a source of some errors. However, care was taken to sample each scan adequately to limit any errors to small values, and any that did occur should average out over the many scans that were digitized.

2.2.3 DATA PRESENTATION

The power pattern of an antenna can be displayed in three different ways, each of which has an advantage, depending on how one wishes to view the results.

1) The RA-DEC Coordinate System

Since the data were taken in this coordinate system, the initial maps of the power pattern were constructed in these coordinates. The data file containing the power pattern was gridded into a 721 X 251 array using the program MDATACHK written by Dr. L.A. Higgs. A 1.0°

gaussian was chosen to smooth the data during the gridding process. The gridded array covered the full 24 hours in RA and from -35^{o} to $+90^{o}$ in DEC, in 0.5^{o} increments.

Figure 2.6 shows the power pattern of the far east antenna in the RA-DEC coordinate system. The site of the transmitter is plainly visible at RA = 19.23^{h}, DEC = $+1.47^{o}$. The horizon limit switches allowed the antenna to be pointed below the transmitter by a few degrees, which made it possible to completely sample the area around the main beam. The 6^{o} strip at the top of the plot is unsampled due to the north pole limit switch. The large blank areas in the lower left and lower right hand regions of the plot are unsampled as well, since they fall below the horizon. The spillover lobe in this plot is the broad curved structure seen in the region $2^{h} \leq \mathrm{RA} \leq 12^{h}$. The narrow curved features which extend from the main beam are caused by scatter from the feedlegs.

The data displayed in the RA-DEC format shown in figure 2.6, gives a good picture of the power received by the antenna when it is pointed at a given location in the sky, but it does not lend itself to the numerical calculation required to give antenna temperature.

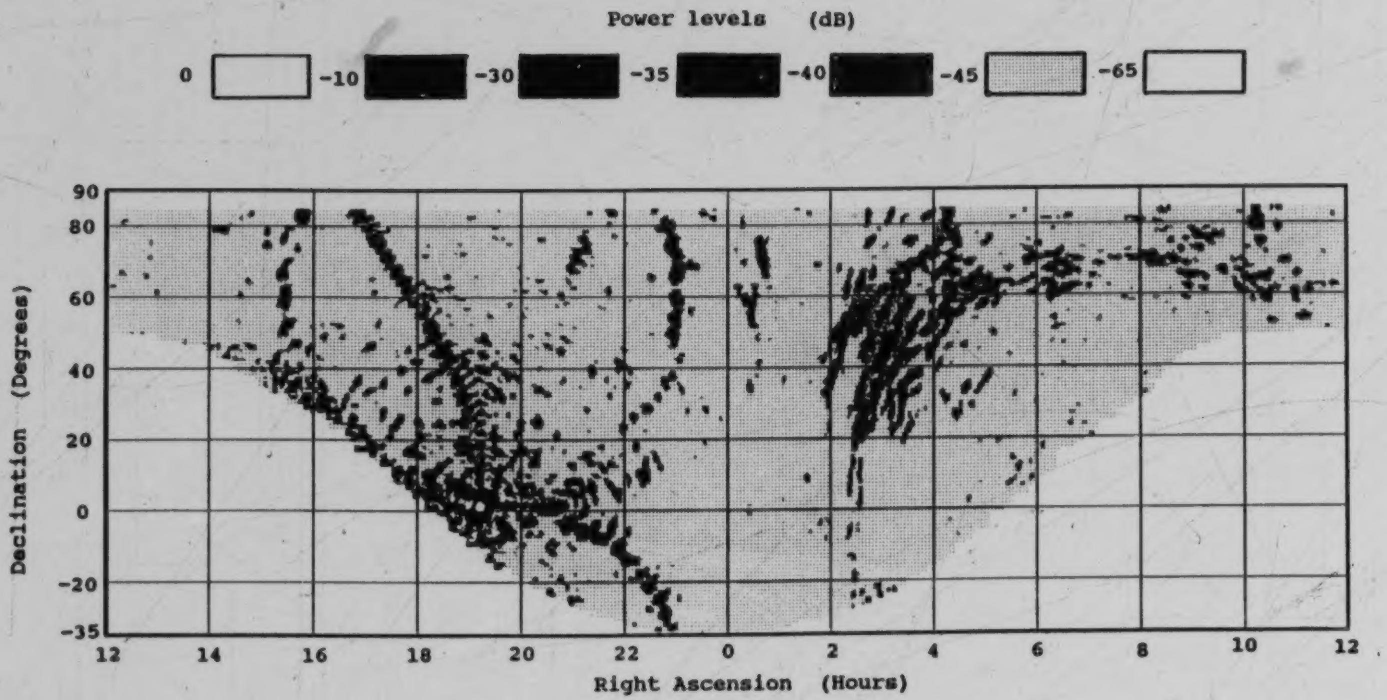

Figure 2.6
The Antenna Pattern Shown in the RA-DEC Coordinate System

The RA-DEC antenna pattern for the FE antenna. The pattern has been shaded to make the spillover lobe and the feedleg scatter lobes stand out. Levels are in dB below the main beam of the FE antenna.

2) The RHO-PHI Coordinate System in Rectangular Form

The RHO-PHI (ρ, ϕ) coordinate system is ideally suited for numerical calculations. In this system, $\rho = 0^{\circ}$ is coincident with the main beam on the axis of the antenna. $\phi = 0^{\circ}$ is oriented in the direction of the north facing feed leg, when the antenna is pointed at the zenith, and increases in the CCW direction as seen from behind. Integrations cf antenna temperature may be performed by summing up contributions in a strip of ϕ at constant ρ. Figure 2.7 shows the (ρ , ϕ) coordinate system superimposed on an antenna and a transmitter, with the antenna receiving power from $\rho = 40^{\circ}$, $\phi = 160^{\circ}$.

A spherical coordinate transformation was performed on the RA-DEC array using the program GRIDHAD written by Dr. L.A. Higgs, which mapped the data to the (ρ, ϕ) plane. Figure 2.8 shows the data mapped into a (ρ, ϕ) array with dimensions of 180 X 360 degrees in 1° increments. In this map, the main beam of the antenna is a horizontal line at $\rho = 0^{\circ}$. The linear features, which begin at the base of the plot and extend to the middle region, are the lobes resulting from feed leg scatter. The spillover region forms a horizontal band in the range $83^{\circ} \leq \rho \leq 118^{\circ}$, the limits being horizon and antenna rim respectively, as seen from the feed.

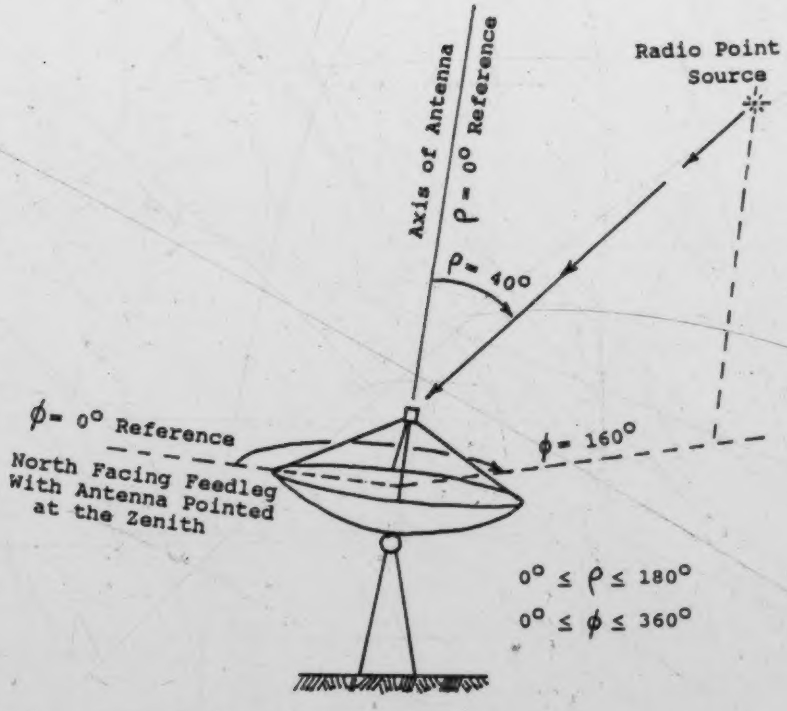
Axis of Antenna
$\rho = 0^\circ$ Reference
Radio Point Source
$\rho = 40^\circ$
$\phi = 0^\circ$ Reference
$\phi = 160^\circ$
North Facing Feedleg With Antenna Pointed at the Zenith
$0^\circ \leq \rho \leq 180^\circ$
$0^\circ \leq \phi \leq 360^\circ$

Figure 2.7
Illustration of the RHO-PHI Coordinate System

The RHO-PHI (ρ , ϕ) coordinate system showing an antenna receiving power from a radio point source at (ρ, ϕ) = (40°,160°).

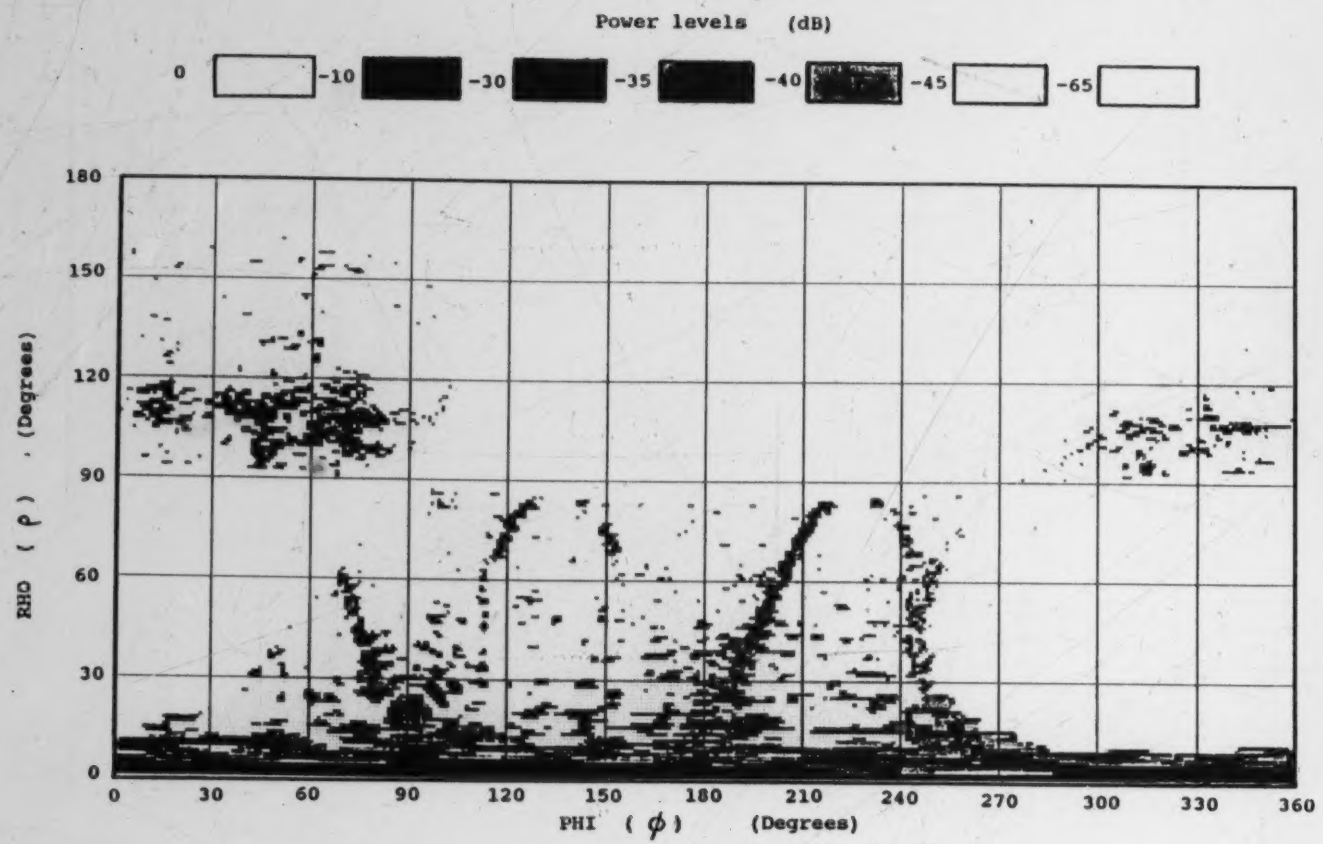

Figure 2.8
The Antenna Pattern Shown in the RHO-PHI Coordinate System

The antenna pattern for the FE antenna displayed in the the RHO-PHI (ρ, ϕ) coordinate system. Power levels are in dB below the main beam of the FE antenna.

The mapping process which converts the RA-DEC data to the (ρ, ϕ) coordinate system is graphically illustrated by figure 2.9. The top plot is the full RA-DEC array, shaded black from -35° to -85° in DEC. Strips 5° wide in DEC are also shown at the top and bottom of the array. The lower plot is the RA-DEC data transformed into the (ρ, ϕ) coordinate system with several locations labeled. The cross hatched area represents the area sampled, which may be compared with figure 2.8. Slightly less than 50 % of the power pattern of the antenna is measurable, due to a combination of the horizon and north pole limit switches on the antenna.

3) The RHO-PHI Coordinate System in Polar Form

For display purposes, the rectangular array of (ρ, ϕ) data may be re-mapped into a polar form. This operation was done using a program called POLAR written by the author. Figures 2.10 and 2.11 show the front and rear halves of the antenna pattern in polar coordinates. The front half is the part which contains the main beam, $(0^\circ \leq \rho \leq 90^\circ)$, and the rear half is the opposite hemisphere $(90^\circ \leq \rho \leq 180^\circ)$. ϕ increases in the CCW direction in the front half, and in the opposite direction in the rear half. The polar plots have the advantage of presenting the antenna pattern in a form which is easier to visualize than the (ρ, ϕ) rectangular plots, which are used

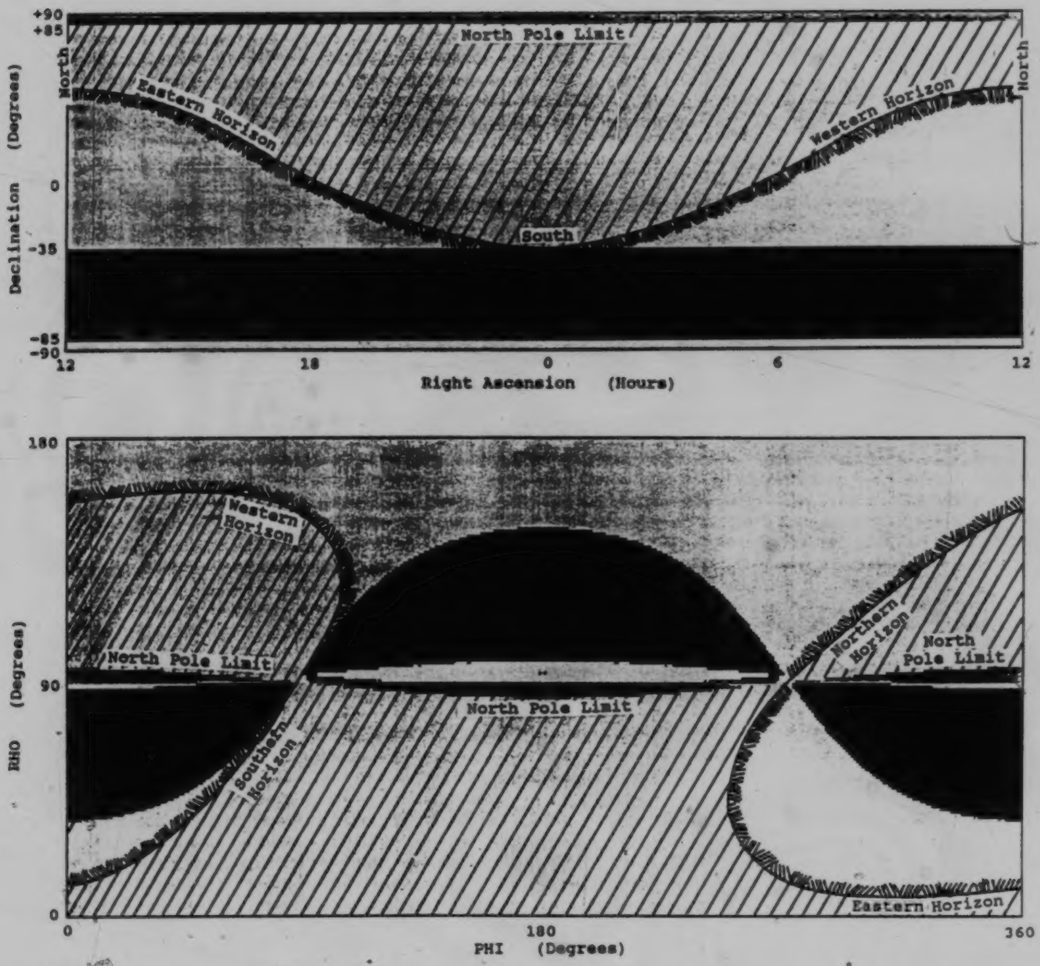

Figure 2.9
Illustration of the RA-DEC to RHO-PHI Mapping Process

The mapping process from the RA-DEC to the RHO-PHI coordinate system, with various locations labeled. The diagonal cross hatching indicates the sampled areas of the antenna pattern in each plot.

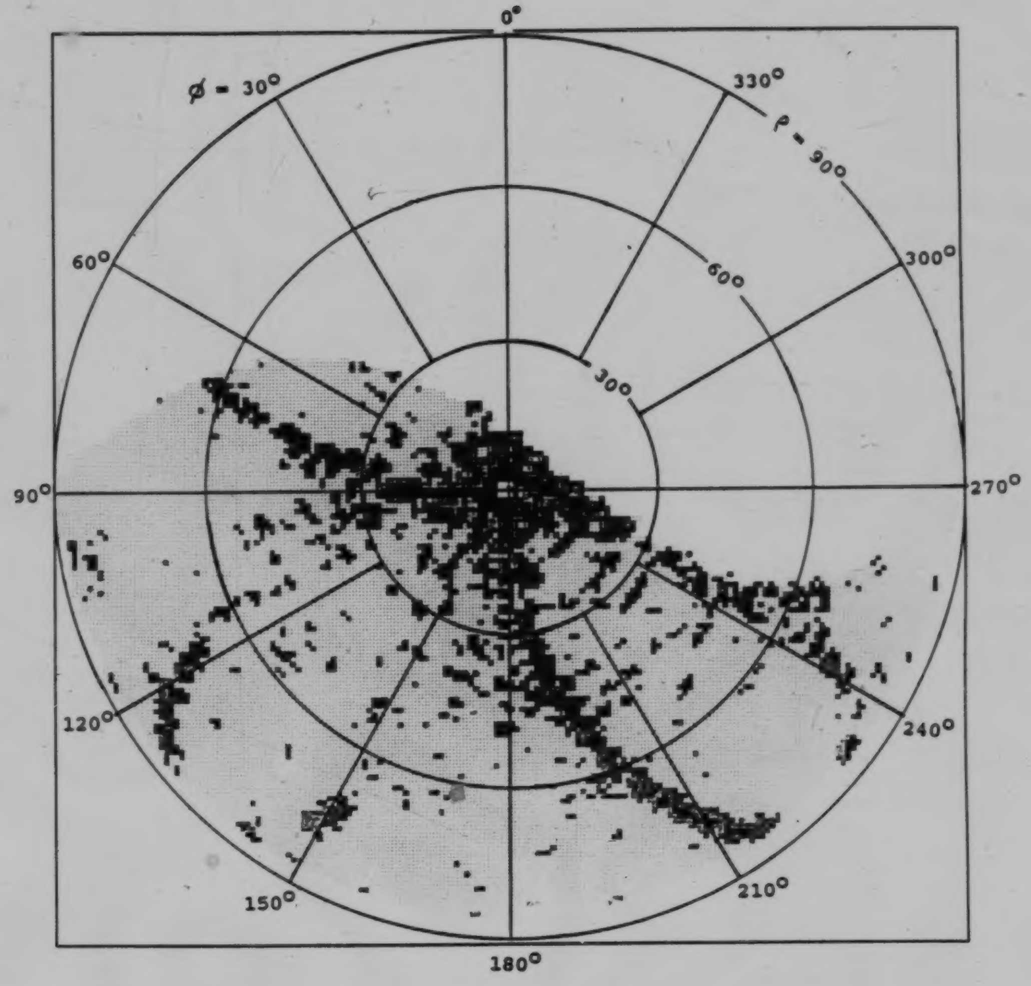

Figure 2.10

The Front Half of the Antenna Pattern for the Far East Antenna

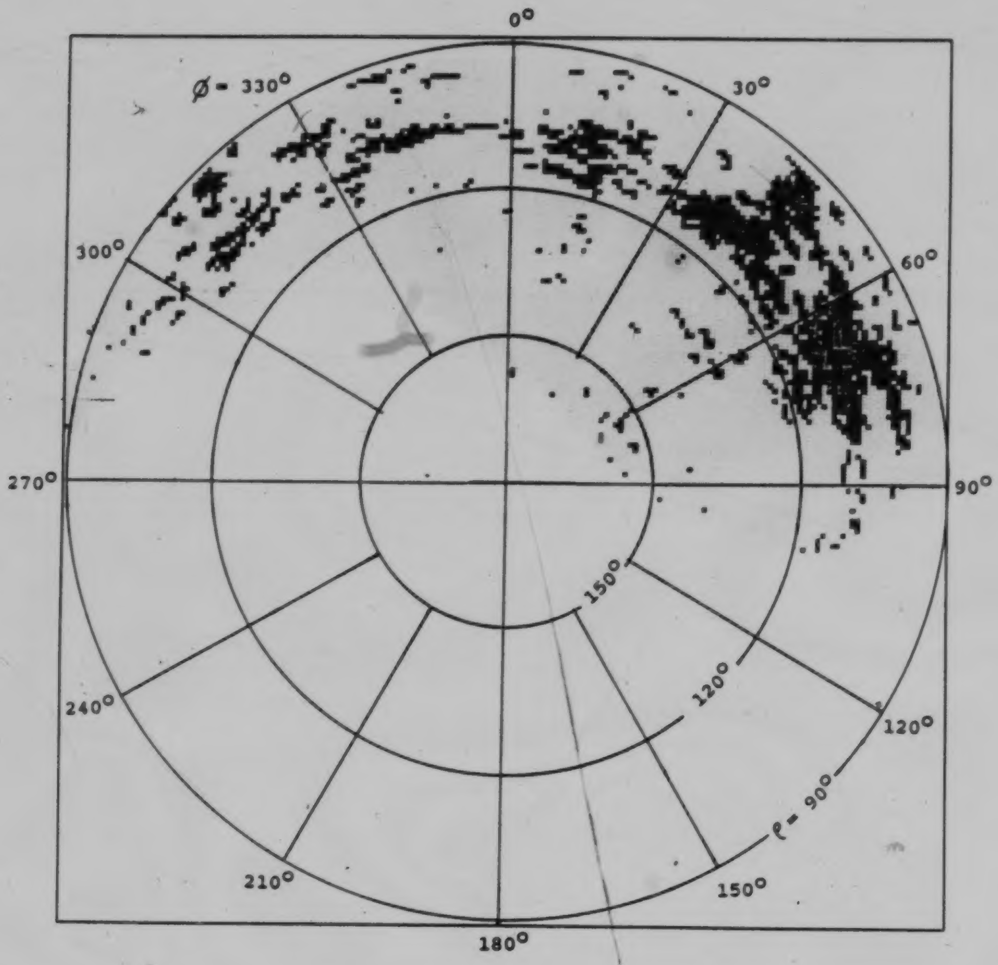

Figure 2.11

The Rear Half of the Antenna Pattern for the Far East Antenna for numerical calculations.

2.3 CALCULATION OF ANTENNA TEMPERATURE USING THE POWER PATTERN OF THE FAR EAST ANTENNA

The power pattern of the far east antenna shown in figure 2.8, allows a numerical calculation of antenna temperature using equation 2.11. The contributions from the sky and atmosphere have been excluded from this calculation for now. Equation 2.11 is the result of integrating equation 1.18 between the appropriate limits of ρ_{Horizon} and 180°, (an integration over regions 2 and 3 of figure 1.6).

$$T_A = \frac{1}{\Omega} \int_{\rho_{\text{HORIZON}}}^{180^\circ} F(\rho, \phi)\, T(\rho, \phi)\, d\omega \qquad 2.11$$

where: $F(\rho, \phi)$ = the measured power pattern shown in figure 2.8,

$T(\rho, \phi)$ = the temperature of the ground in the direction (ρ, ϕ), and

Ω = the antenna solid angle (1.23×10^{-3} steradians), obtained from

$$\Omega = \frac{\lambda^2}{A_e} \qquad 2.12$$

where: A_e = the effective area of the antenna (the product of the physical area with the aperture efficiency which has been found to be ~ 0.55 for the DRAO antennas).

2.3.1 CONSIDERATIONS REQUIRED BEFORE DETERMINING ANTENNA TEMPERATURE

In order to use equation 2.11, along with the measured power pattern of the far east antenna, to calculate antenna temperature, three things must be considered.

1) The first consideration is the fact that there is incomplete coverage in the measured power pattern shown in figure 2.8. This condition exists along the ϕ direction for all values of ρ except around the region of the main beam ($-10^\circ \geq \rho \geq 0^\circ$). The problem is illustrated by figure 2.12 which is the number of pixels which contain data values plotted as a function of ρ , the angle from the main beam of the antenna. From the plot it can be seen that for $\rho > 9^\circ$, there is a sharp decline in the number of

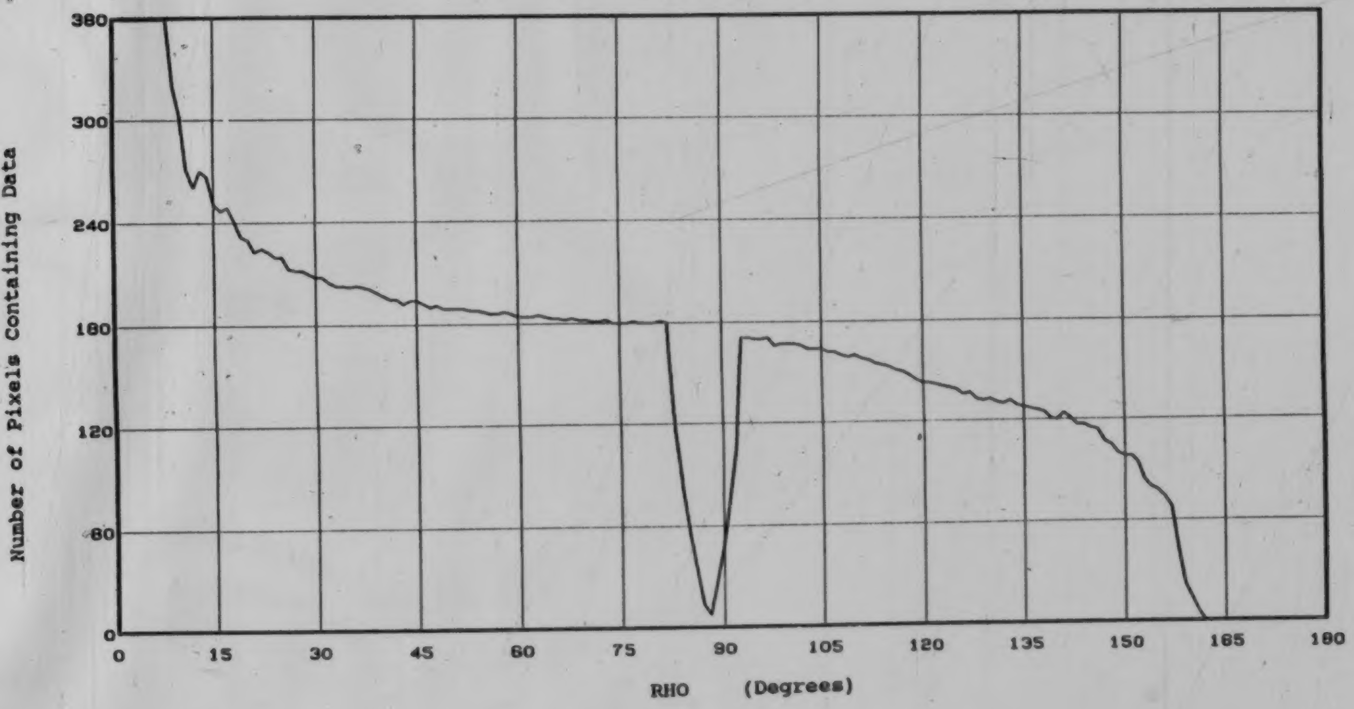

Figure 2.12

The Number of Pixels in the PHI Direction That Contain Data as a Function of RHO pixels that contain power pattern data. There is quite a deficiency of data in the region $83^\circ \leq \rho \leq 93^\circ$ as well, and a complete absence of data in the region $\rho > 162^\circ$. These features are the result of not being able to sample the power pattern of the antenna in these areas due to limit switch restrictions (the antennas cannot be pointed below the horizon to any great extent).

To use the (ρ, ϕ) data in equation 2.11 to calculate antenna temperature at a given ρ, the average power (P_{AVE}) in a strip of $\Delta\rho$ must be determined from the pixels which contain data and then applied to the whole strip. Figure 2.13 is a plot of P_{AVE} as a function of ρ for the far east antenna. This is another way of looking at the antenna pattern. In this representation the power pattern of the antenna is assumed to be symmetrical in ϕ and to have the value of P_{AVE} at the value of ρ of interest. P_{AVE} for a given ρ is calculated by summing the power levels in each of the pixels that contain data and then dividing by the number of pixels. Fill values of P_{AVE} = -47.5 dB have been inserted into the area of $\rho \geq 162^\circ$, which represent an approximation of the average power levels in this region. One cut was made through the back lobe, which gave -45 dB for the power level at $\rho = 180^\circ$.

2) Secondly, to obtain antenna temperature from equation 2.11, values of ground temperature T_G must be

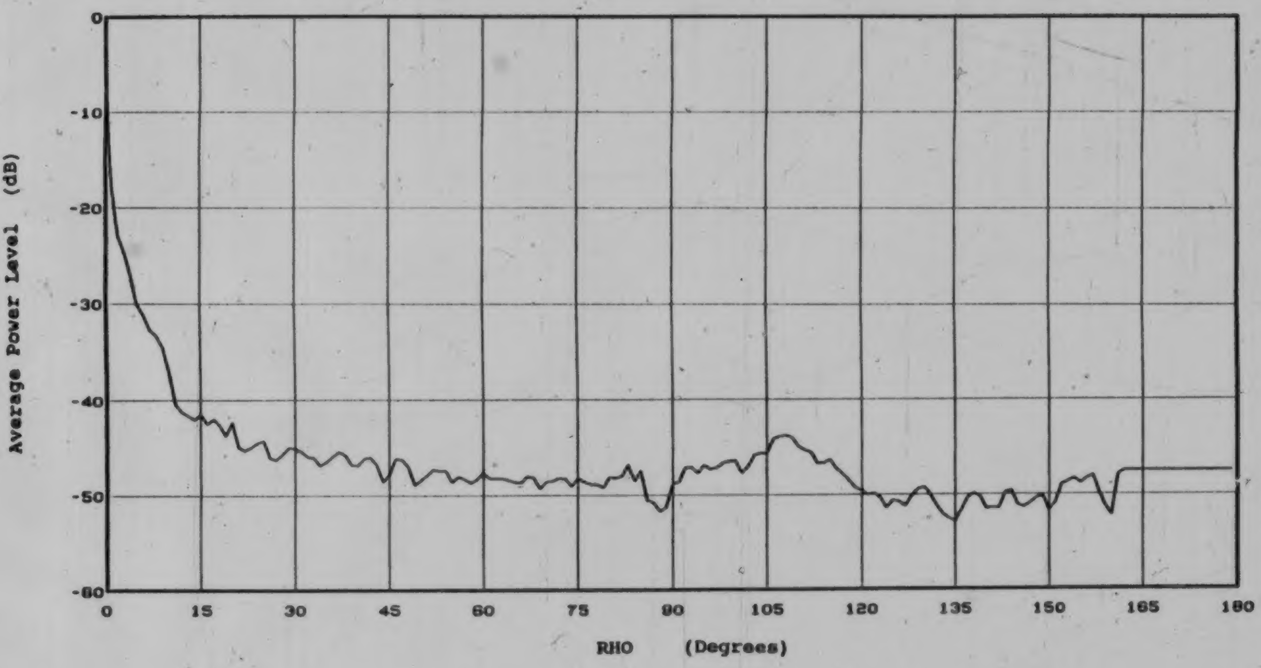

Figure 2.13

The Average Power (P_{AVE}) as a Function of RHO for the Far East Antenna known to supply values for the term $T(\rho, \phi)$. Table 2.4 contains measurements of T_G obtained by pointing the fifth antenna at the ground at a variety of locations around the observatory. A theodolite was used to find the elevation angle and the bearing to each of the sites. This information along with the elevation of the antenna enabled each of the sites to be located on a topographic map, which in turn made it possible to find the angle of incidence that the main beam had with the ground at each location. The equivalent ρ can be found by subtracting the angle of incidence from 90°. This assumes that the ground conditions in the hills surrounding the observatory are the same as those in the vicinity of the antenna. The resulting curve for ground temperature as a function of ρ is found in figure 2.14. The data point at $\rho = 180^\circ$ was obtained by connecting the receiver to a horn which was pointed at the ground, and making an allowance for the loss in the cable. Figure 2.14 assumes that T_G is symmetrical in the ϕ direction.

3) The last point to consider in applying equation 2.11 to calculate antenna temperature, is the upper limit of integration (the angle of the horizon as seen from the feed of the far east antenna). To answer this question the elevation of the horizon, as seen from the far east antenna, was obtained using a theodolite. The results were

TABLE 2.4 MEASUREMENTS OF T_G

No.	Bearing (Deg)	Elevation (Deg)	ζ (Deg)	ρ (Deg)	T_G (K)	Ground Conditions
1	124.0	3.57	26.5	116.5	250	cliff
2	156.7	4.67	12.0	102.0	245	trees
3	244.3	5.67	10.0	100.0	232	trees
4	290.7	6.70	6.5	96.5	200	bare ground
5	301.7	7.58	18.0	108.0	212	bare ground
6	312.3	5.92	17.8	107.8	234	bare ground
7	306.7	8.12	16.7	106.7	223	trees

Note: ζ = the angle of incidence.
ρ = the equivalent ρ calculated from the angle of incidence.

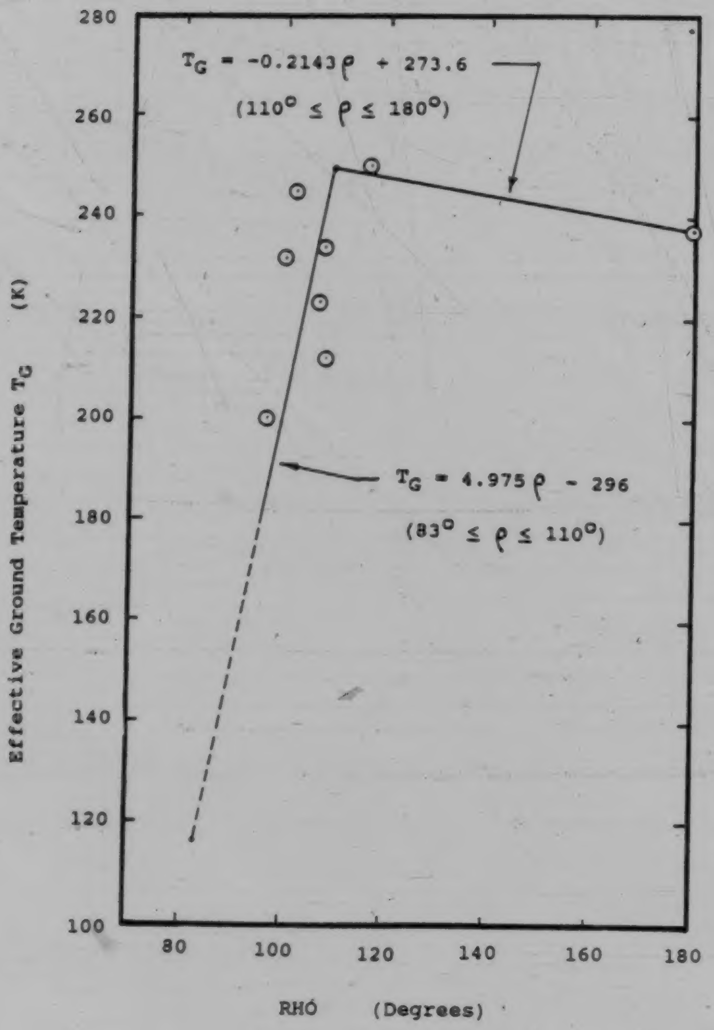

Figure 2.14

Effective Ground Temperature T_G as a Function of RHO

The effective ground temperature as a function of the angle of incidence was measured by using the fact that the observatory is in a bowel. This information was then applied to the integration process assuming flat ground.

then plotted on the (ρ, ϕ) array giving figure 2.15. In this figure any lobes of the antenna pattern that occur at values of $\rho \geq \rho_{horizon}$ will fall on the ground, whereas any that fall at $\rho \leq \rho_{horizon}$ will project into the sky when the antenna is pointed at the zenith. The lobes that fall on the ground will contribute to antenna temperature.

The average value of ρ for the horizon in figure 2.15 is ~ 83° as seen from the feed of the far east antenna, which is equivalent to an average elevation angle of 7°. Therefore 83° is used in equation 2.11 for the upper limit of integration.

2.3.2 NUMERICAL CALCULATION OF ANTENNA TEMPERATURE USING THE ANTENNA PATTERN

With the above points taken into consideration, the antenna temperature for the far east antenna was calculated, excluding contributions from the sky and the atmosphere. The antenna pattern shown in figure 2.8 was numerically integrated using a program called SPILLOVER, written by the author, with the results plotted in figure 2.16.

Integration begins at $\rho = 83^\circ$ and proceeds to $\rho =$

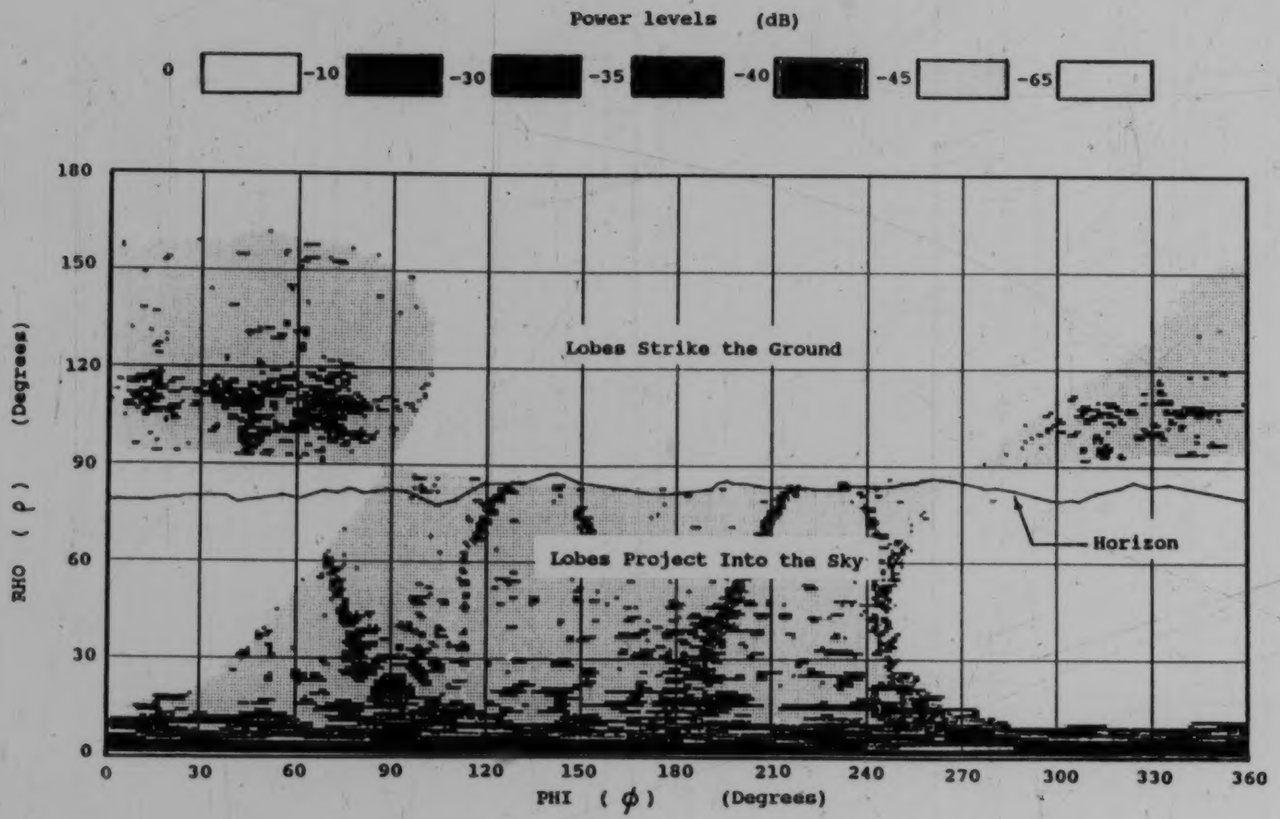

Figure 2.15

The RHO-PHI Antenna Pattern with the Horizon Superimposed

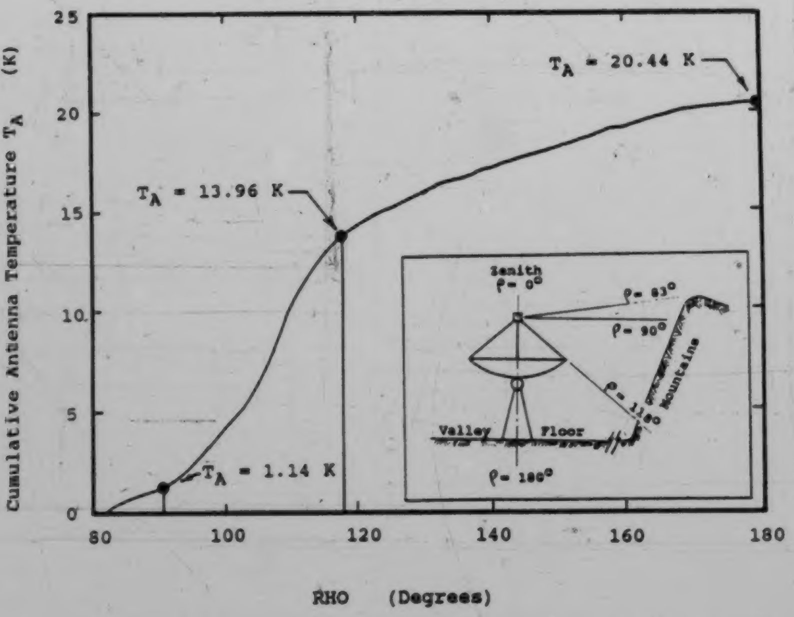

Figure 2.16

Cumulative Antenna Temperature as a Function of RHO

Plot of cumulative antenna temperature as a function of RHO calculated from figure 2.8, showing T_A at RHO = 90° (total due to mountains), 118° (total due to spillover and feedleg scatter), and at 180°, to give total T_A.

90°, giving antenna temperature = 1.14 K. This represents the contribution to antenna temperature from the surrounding mountains. At $\rho = 118^{\circ}$ (the edge of the antenna), the spillover region has been completely integrated to give antenna temperature = 13.96 K. This region (region 2 in figure 1.6) also includes contributions to antenna temperature from feedleg scatter.

The remaining region is region 3 of figure 1.6, the area behind the antenna. From figure 2.16 it can be seen that an additional 6.48 K is added to antenna temperature from integrating the antenna pattern from $\rho = 118^{\circ}$ to 180°. The antenna temperature resulting from integrating the complete pattern of the far east antenna is 20.44 K. The contribution from the sky (5.0 K), and atmosphere (2.2 K) must be added to give the value of 27.6 K for the total antenna temperature.

The determination of antenna temperature from selected areas of the antenna pattern is of interest. Three such areas which are shown in figure 2.17, have had their contributions to antenna temperature summed only if the power levels of the pixels in question fall above -45 dB. This windowing of the power levels has had the effect of selectively integrating the features which stand out above the background in figure 2.17.

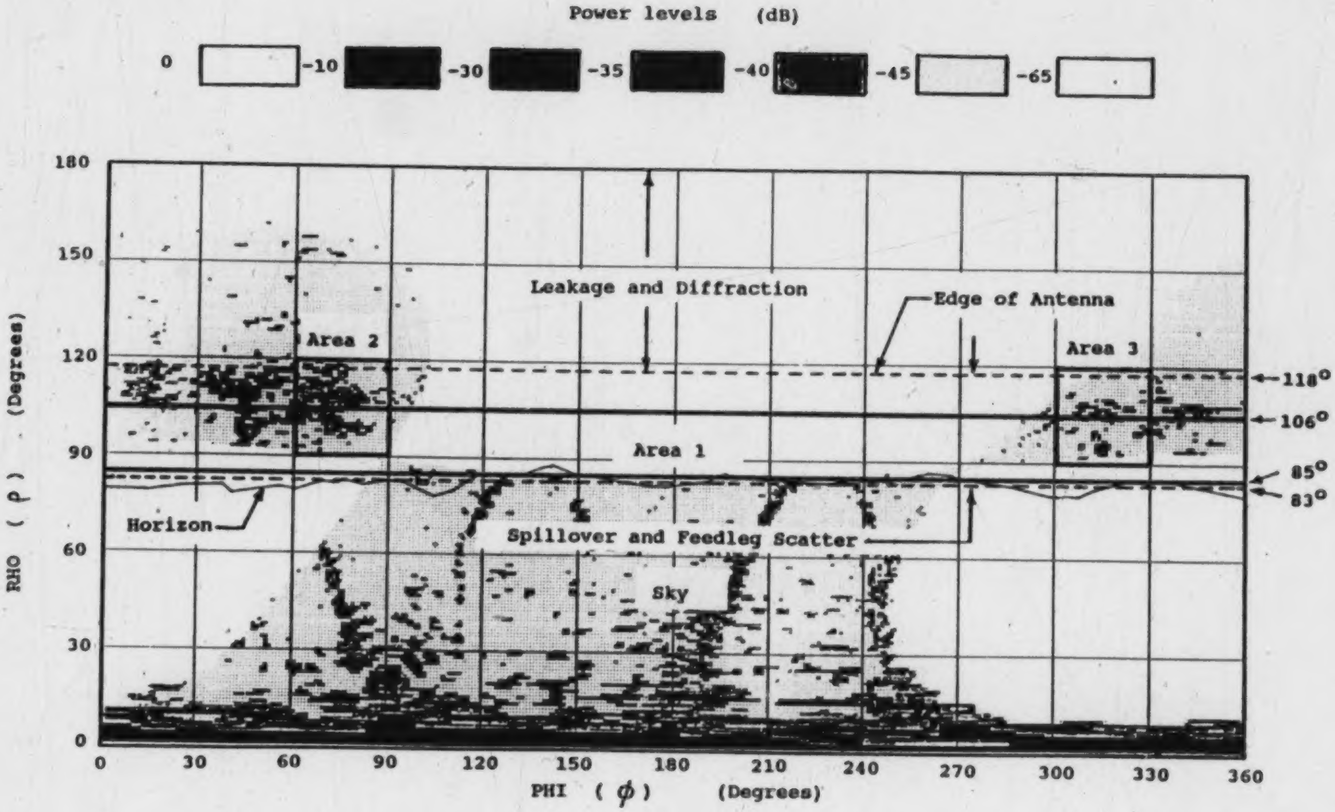

Figure 2.17
Antenna Temperature for Selected Areas of the Pattern

Plot of the RHO-PHI antenna pattern with T_A determined for selected areas. T_A for areas 1, 2, and 3 are 2.05, 1.74, and 0.5 K respectively.

Area 1 is a horizontal strip of the antenna pattern located in the range $85^\circ \leq \rho \leq 106^\circ$. The main features selected for integration in this case are the scatter lobes from the feedlegs. Antenna temperature for this strip is 1.40 K. The upper limit of integration was restricted to $\rho = 106^\circ$ to avoid including significant contributions from the spillover lobe of the antenna, seen as the darker areas in $\sim 106^\circ \leq \rho \leq 118^\circ$.

The integration of antenna temperature in the strip $106^\circ \leq \rho \leq 118^\circ$ suggests that antenna temperature due to feedleg scatter could be much higher than 1.40 K. First, the scatter lobes from the feedlegs extend into the upper regions of the spillover area in $106^\circ \leq \rho \leq 118^\circ$. This contribution was not included in the integration of area 1. Secondly, from figure 2.17 it can be seen that much of area 1 falls in an unsampled area of the antenna pattern. If the scatter lobes from the feedlegs are extended through this area, it can be seen that only a small fraction of the lobes have been integrated to obtain 1.40 K. Therefore, the contribution from feedleg scatter likely forms a significant portion of the total antenna temperature for this antenna.

Areas 2 and 3, shown in figure 2.17, have been integrated to give 1.33 K and 0.34 K respectively. These two areas are located in the sampled portion of the spillover lobe of the antenna.

From figure 2.17, it can be seen that a large portion of the spillover region falls into the unsampled area of the antenna pattern. Since the determination of antenna temperature relies on calculating the average power in a strip of ρ from the available data, and then applying it to the unsampled region, a possible problem exists. If the antenna pattern is asymmetrical in the ϕ direction, and if the sampled region of the pattern is not representative of the whole pattern , an error in the determination of antenna temperature will be the result. Areas 2 and 3 of figure 2.17 are equal in all respects except for their location in ϕ , yet the antenna temperature due to these two areas differs by a factor of ~ 4. This indicates that the antenna pattern may be asymmetrical in ϕ , which casts some doubt on the integration of antenna temperature for the spillover region.

The same applies for the leakage and diffraction region (region 3 in figure 1.6), shown in figure 2.17. However, the sampled portion of the antenna pattern in this region appears to be fairly symmetrical in the ϕ direction, which would indicate that the determined antenna temperature due to leakage and diffraction is likely more reliable than that of the spillover region.

An important check on the accuracy of the antenna pattern can be performed by integrating it and comparing the result to the known solid angle of the antenna. This was done, but the total solid angle was found to be only 0.659 X 10^{-3} sr, about half of the actual value (1.23 X 10^{-3} sr). The integration failed to give the correct result due to sampling the data on a 1° grid (too coarse for this purpose) around the main beam area, where most of the solid angle resides.

However, the check can be performed in a modified way. The pattern can be integrated for the region outside the main beam to find Ω_S, which can be used to calculate a beam efficiency given by

$$\eta_B = \frac{\Omega_A - \Omega_S}{\Omega_A} \qquad 2.13$$

where: Ω_A = the solid angle of the antenna (1.23 X 10^{-3} sr),

Ω_S = the solid angle in the region outside the main beam (0.323 X 10^{-3} sr from integrating the antenna pattern shown in figure 2.8).

Evaluating equation 2.13 gives $\eta_B = 0.74$, based on the measured power pattern of the antenna.

The beam efficiency may also be obtained using the expression[15]

$$\eta_B = \frac{\eta_a A_p \Omega_M}{\lambda^2} \qquad 2.14$$

where: η_a = the aperture efficiency of the antenna (~ 0.55),

A_p = the physical area of the antenna (65.61 m^2),

λ = the wavelength of observation (0.211 m), and

Ω_M = the solid angle in the main beam, which can be estimated from equation 2.15 assuming a Gaussian beam.

$$\Omega_M = 1.133(\text{HPBW})^2 \qquad 2.15$$

In the case of the far east antenna, for a HPBW = 103', $\Omega_M = 1.017 \times 10^{-3}$ sr. Evaluating equation 2.14 with this result gives $\eta_B = 0.82$, which compares reasonably well with $\eta_B = 0.74$ based on the measured power pattern. This result demonstrates that the antenna pattern shown in figure 2.8 is an accurate representation of the power pattern for the far east antenna. It also shows that the results of any calculations using the power pattern should be valid as long as the region of the main beam is avoided ($\rho \leq 2^{\circ}$).

2.3.3 SUMMARY OF RESULTS

The results obtained from the numerical integration of the antenna pattern can now be compared with those obtained using the theoretical methods detailed in section 2.1. Table 2.5 lists the theoretical calculations for the various components of antenna temperature, along with those determined from the integration of the power pattern of the far east antenna.

Antenna temperature due to the atmosphere and sky has been assumed to be the same in both cases. The mesh leakage and diffraction contribution determined from the antenna pattern is 6.48 K which agrees extremely well with the theoretical value of 6.5 K. This result indicates that figure 2.14 gives reasonably accurate values for ground temperature in the region $118^{\circ} \leq \rho \leq 180^{\circ}$.

TABLE 2.5 SUMMARY OF RESULTS OF ANTENNA TEMPERATURE FOR THE FAR EAST ANTENNA

Contributing Source	Theoretical Value	Value from integrating Antenna Power Pattern (plus atmosphere and sky)
Atmosphere	2.2	2.2
Sky	5.0	5.0
Spillover	6.1	13.96*
Feedleg Scatter	-	
Mesh Leakage	5.9	6.48
Diffraction	0.6	
Totals	19.8 ± 2.5 K	27.6 ± 3.0 K

(T_A measured in 1980 = 25.9 ± 2.5 K)

* includes contribution from feedleg scatter lobes

A larger discrepancy exists in the estimate for spillover and feedleg scatter. Integration of the antenna pattern yields 13.96 K, whereas the theoretical estimate (which does not include feedleg scatter) is only 6.1 K. A possible explanation of the discrepancy is that the feedleg scatter could account for up to 4 or 5 K, which would bring the theoretical value up to 24 or 25 K. The remaining difference could be the result of sampling regions of higher power in an asymmetrical antenna pattern. If this is the case, during the integration of the pattern, the average power for the strips of ρ would be assigned artificially high values, which would in turn boost the calculated value of antenna temperature for that region. This explanation is supported by the difference in antenna temperature (by a factor of ~ 4) that has been obtained by integrating areas 2 and 3 shown in figure 2.17.

One of the main results of estimating antenna temperature directly by integration of the power pattern of the far east antenna, is that it indicates that there is likely a significant contribution to antenna temperature from the scatter lobes of the feedlegs. Unfortunately, gaps in the sampling of the power pattern prevent a determination of their magnitude. However, the experiments performed on the fifth antenna, which are described in chapter 3, give some indication of how significant these contributions are, in relationship to total antenna temperature.

CHAPTER 3

TWO METHODS OF REDUCING ANTENNA TEMPERATURE

This chapter describes two experiments to reduce the antenna temperature of an antenna. The fifth antenna of the synthesis telescope was chosen for these experiments over the Far East antenna, since it was in the process of being integrated into the existing array, and not yet involved in gathering data. In addition to the description of the experiments, some discussion is devoted to the effects of the size, configuration, and material of the feedlegs on antenna temperature.

The first method used to reduce antenna temperature is that of placing a fence or shroud on the rim of the antenna parallel to its axis. The fence has the effect of reducing the amount of ground radiation that finds its way over the rim of the antenna and into the feed.

The second method used to reduce antenna temperature involves changing the shape of the feedlegs to limit the amount of ground radiation that is scattered off the feedlegs and into the antenna. The narrow curved features seen in figures 2.6 and 2.8, are the scatter lobes caused by the feedlegs. When these lobes strike the ground, noise is added to the system. The shape of the feedlegs was changed from a circular to a triangular cross-section with a rough leading edge, which had the effect of lifting the feedleg scatter lobes off the ground and placing them closer to the main beam, thus reducing the antenna temperature. Both of these experiments were performed at 1420 MHz on the fifth antenna.

3.1 THE METHOD USED TO MEASURE ANTENNA TEMPERATURE

In order to determine how effective each of the modifications was at reducing system noise, the antenna temperature was measured for each change in the configuration of the antenna.

3.1.1 THE RECEIVER

Figure 3.1a shows a block diagram of the Dicke receiver which was used on the fifth antenna for the antenna temperature measurements. The receiver was installed and tested by Phillip Phu, a DRAO summer student, who also assisted in making the measurements.

The linearity of the receiver was checked by adding a calibration noise source to the various signal levels measured throughout the range. The results of this test appear in figure 3.1b, and demonstrate that the receiver

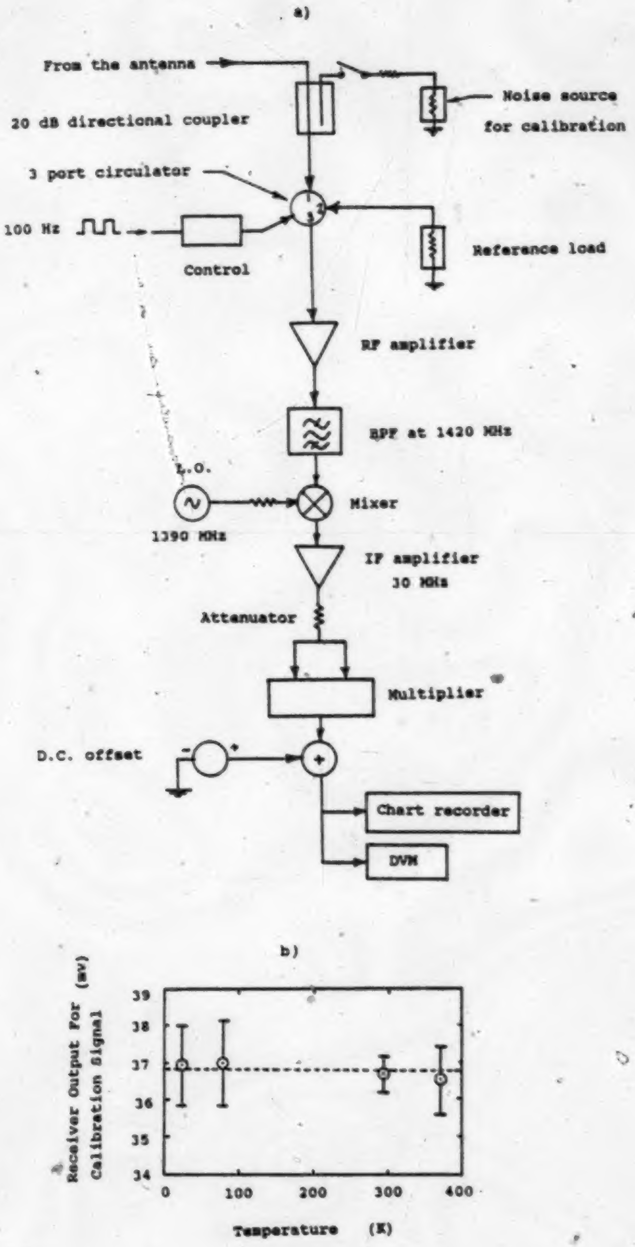

Figure 3.1
Block Diagram of the Dicke Receiver, and Results of the Linearity Test

a) Block diagram of the Dicke receiver used in the antenna temperature measurements.
b) The results of the linearity test, with error bars shown at the 1 σ level.

output can be assumed to be linear as a function of antenna temperature over the range of measurements taken.

This type of receiver works by switching between the antenna and a comparison load at a rate high enough that the effects of any gain variations in that time are minimized. The output of the receiver is proportional to the difference between the input from the antenna and the reference load. The output was recorded on a digital voltmeter and a chart recorder was used to provide a permanent record of the measurements.

3.1.2 THE MEASUREMENT METHOD

To measure the antenna temperature, the antenna was disconnected from the receiver and replaced with high quality hot and cold 50 ohm loads held at 373 K and 80 K respectively. The instrument (Ailteck Model 70 reference load) which supplied these two references used liquid nitrogen, and electrical heating to accurately maintain the cold and hot load temperatures. The output of the receiver was recorded using a digital voltmeter for both the hot and cold loads. From equation 3.1 it can be be seen that the power output of the load is linear with temperature, therefore the ratio of K/volt can be calculated:

$$P = kTB \quad 3.1$$

where k = Boltzmann's constant,

T = absolute temperature, and

B = the bandwidth.

After the outputs for the hot and cold loads were recorded, the antenna was reconnected and the receiver output was measured with the antenna pointed at the zenith. From these measurements, the absolute antenna temperature is found. Several readings were averaged for each measurement of the zenith, and the hot and cold loads to minimize the effects of drift in the system. However, the individual readings used in the averages had variations that would cause the antenna temperature to vary by ± 3.0 K if the extremes were used in the calculations. Figure 3.2 shows a plot of one determination of antenna temperature for the fifth antenna using averaged values of 0.5541, 0.9553 and 0.4740 volts for the cold, hot, and zenith measurements respectively.

The antenna temperature given for each configuration of the antenna is the average of two or more measurements,

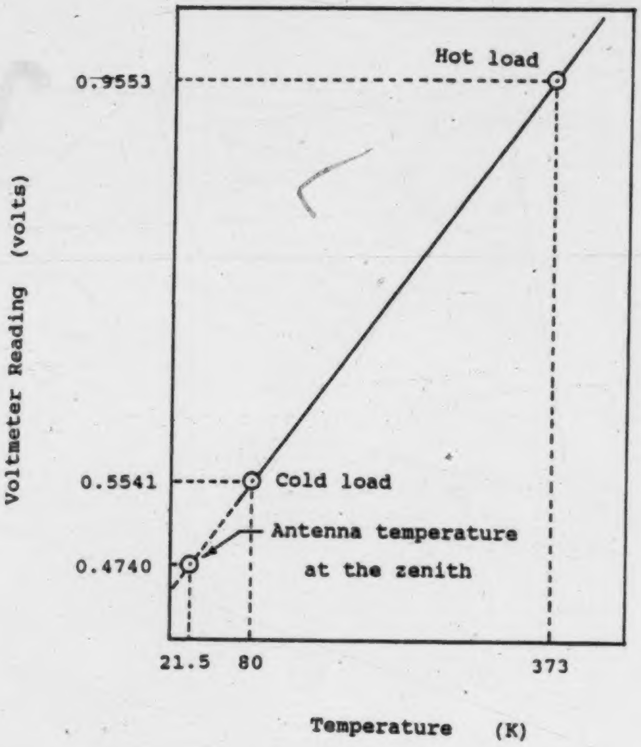

Figure 3.2
A Determination of Antenna Temperature

A plot showing the details of one determination of antenna temperature for the fifth antenna made on August 20, 1987. An antenna temperature at the zenith of 21.5 K is found using a straight line extrapolation through the calibration points obtained from the hot and cold loads.

and is given with a ± error estimate. The error listed is standard error (α), which is defined by

$$\alpha = \sigma / \sqrt{n} \qquad 3.2$$

where: n = the number of measurements, and

σ = the standard deviation of the measurements given by

$$\sigma = [\ (1/(n-1)) \sum_{i=1}^{n} (x_i - \overline{x})^2]^{1/2} \qquad 3.3$$

where: x_i = the i^{th} measurement, and

$\overline{x}$ = the mean of the measurements.

Using a cold load with liquid helium in place of liquid nitrogen would increase the accuracy of these measurements. Since the helium load would be at ~ 4.3 K, the antenna temperature would be between the calibration points and the extrapolation shown in figure 3.2 would be avoided.

3.2 EXPERIMENTAL REDUCTION OF ANTENNA TEMPERATURE USING A FENCE

One effective and low cost method of reducing the antenna temperature of an antenna is to place a fence or shroud around its rim to block ground radiation from entering the feed. An analysis of shrouds has shown that a paraboloid with a shroud shows better suppression of the far sidelobe levels than a paraboloid without one[16]. It is in this range of $\sim 90^\circ \leq \rho \leq 180^\circ$ that a reduction of the power levels of the antenna will reduce the antenna temperature, since lobes in this range of ρ strike the ground when the antenna points at the zenith.

Figure 2.13, which plots the average power in the antenna pattern as a function of ρ, shows the spillover lobe in $83^\circ \leq \rho \leq 118^\circ$. If a 0.91 m fence was added to the far east antenna, it would subtend about 10° ($108^\circ \leq \rho \leq 118^\circ$) as seen from the feed. The amount of ground radiation entering the antenna from this region would then be reduced, which would result in a lower antenna temperature. Figure 3.3 shows an antenna with a fence, and the area which is shielded from ground radiation as a result.

To assess the effectiveness of this method a 0.91 m

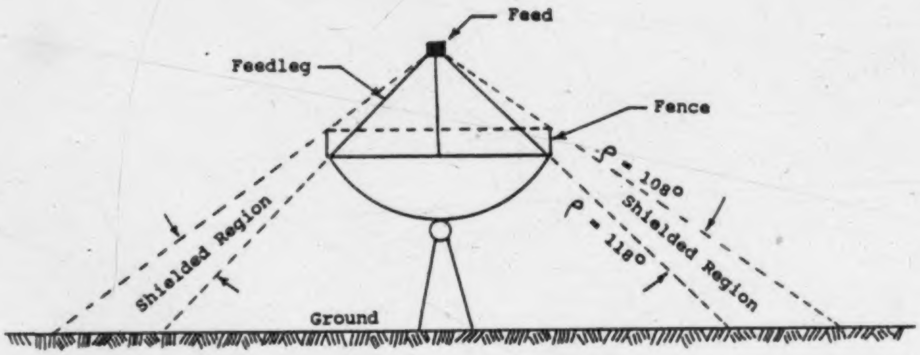

Figure 3.3
An Antenna with a Fence

A drawing of an antenna with a fence showing the area from which ground radiation is suppressed. Values of ρ are shown for the far east antenna.

high fence was placed on the fifth antenna. The fence material was a screen with mesh size of 1.27 cm made from 0.1 cm diameter galvanized wire. The screen dimensions allow only ~ 2.5 percent of the incident power to leak through, an estimate obtained by using a nomogram for transmission through a grid of wires[17]. The screen was held in place on the rim of the antenna with 2.54 X 2.54 cm aluminum angles which were in turn attached to the backing structure of the antenna with metal hose clamps. The addition of the fence did not affect the driving operations of the antenna, since its total weight was only ~ 27 kg. As well, because of the mesh nature of the material, the fence offered little resistance to the wind.

Several measurements of antenna temperature with and without the addition of the fence were made. These are listed in table 3.1. From the data in table 3.1 it can be seen that five measurements of the antenna without the fence were made, two of which average to 30.1 ± 0.3 K, the remaining three averaging to 26.3 ± 0.3 K. The only apparent difference in these two sets of measurements is the ambient temperature on the days on which the measurements were done. The measurements made on July 14/87 had an ambient temperature of 32.4 ^{o}C, 10 ^{o} C warmer than those made on August 20/87. The higher antenna temperature measured on July 14/87 probably resulted partly

TABLE 3.1
ANTENNA TEMPERATURE MEASUREMENTS FOR THE FIFTH ANTENNA AT THE ZENITH WITH AND WITHOUT A FENCE

Date (1987)	Ambient Temperature (^{o}C)	Antenna Config.*		Antenna Temperature (K)
July 14	32.4	1		30.3
		1		29.8

			Ave:	30.1 ± 0.3 K
Aug. 20	22.4	1		25.8
		1		26.3
		1		26.9

			Ave:	26.3 ± 0.3 K
July 28	23.2	2		19.5
		2		17.6
		2		15.9

			Ave:	17.7 ± 1.0 K
July 30	23.0	2		19.5
		2		17.9
		2		17.7

			Ave:	18.4 ± 0.6 K
	Average for antenna with fence :			18.0 ± 0.6 K

* 1: Bare antenna, (no modifications)
2: Fence added to antenna

Note: The ± errors listed are standard errors (α) given by equation 3.2.

from the ground being warmer than it was on the cooler day in August.

Six measurements of antenna temperature were made with the fence in place, three each on July 28 and July 30, 1987. The averages for each day were 17.7 ± 1.0 K and 18.8 ± 0.6 K respectively, with an overall average of 18.0 ± 0.6 K. The ambient temperature on both these days was about 23 °C.

Since the ambient temperature of August 20 is nearly the same as it was on July 28 and 30, the antenna temperature obtained on August 20 has been used as the reference for the antenna without modifications. Therefore, using 26.3 ± 0.3 K as the reference, an 8.3 ± 0.7 K improvement is obtained with the addition of the fence. This represents a 31.6 % reduction of the antenna temperature for the fifth antenna of the array. This is slightly higher than the total predicted spillover value of 6.1 K from table 2.1, obtained by integrating the feed pattern. The value of 8.3 K includes some of the contribution from feedleg scatter, which the fence has suppressed. From table 2.1 one would expect the fence to reduce the antenna temperature by about 4 K.

3.3 REDUCTION OF ANTENNA TEMPERATURE USING FEEDLEGS WITH A TRIANGULAR CROSS-SECTION

In section 2.1 the values of the individual contributors to antenna temperature were discussed which resulted in an estimated total of 19.8 ± 2.5 K for the antennas of the DRAO synthesis telescope. From the measured power pattern of the far east antenna shown in figure 2.8, it is evident that the scatter lobes from the feedlegs could form a significant contribution to antenna temperature, and therefore should not be ignored.

3.3.1 CHARACTERIZATION OF THE FEEDLEG LOBES IN THE ρ - ϕ PLANE

If the location, width, and power levels of the scatter lobes from the feedlegs are known, an estimate of their contribution to antenna temperature is possible. This would be useful in deciding if it is worth trying to reduce the contribution to antenna temperature from this source.

1) LOCATION OF THE SCATTER CONES IN THE (ρ, ϕ) SYSTEM

The scatter lobes from a feedleg take the shape of a cone with a half-vertex angle β , where β is the angle between the feedleg and the boresite direction of the antenna[18]. The geometry of the resulting cone is shown in figure 3.4. Knowing the shape of the cones, a theoretical calculation of their location may be performed. This was done using a program called FLCONES.BAS (written by the author), which calculates the locus of the scatter cones caused by the feedlegs in the (ρ, ϕ) coordinate system.

To calculate the location of the feedleg scatter cones one must look at the spherical triangle (shown in figure 3.5) formed between points (A) the main beam, (B) any point on the scatter cone, and (C) the (ρ, ϕ) location of the axis of the feedleg. The (ρ, ϕ) coordinates of any point B on the locus of the scatter cone are given by

$$(\rho, \phi)_{\text{point B}} = (c,\ \phi_{AC} - \alpha) \qquad 3.4$$

where: α = the angle that is formed between sides b and c of the triangle ABC as point B is moved along the locus of the cone (positive in the direction indicated in figure 3.5), and

c = the length of the side joining the main beam (A) to any point on the scatter cone.

In equation 3.4, side c is given by

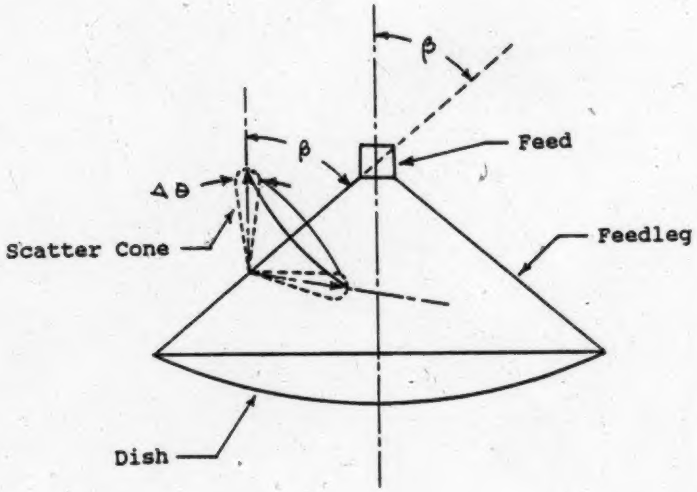

Figure 3.4

The Geometry of a Scatter Cone from one of the Feedlegs

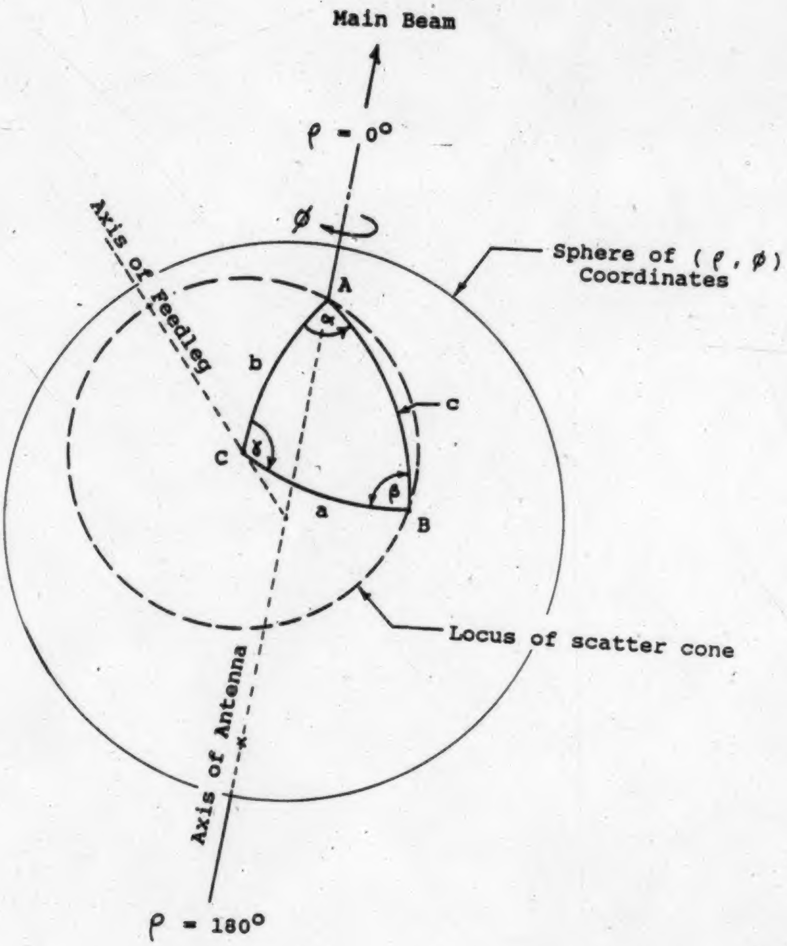

Figure 3.5
Determining the Location of the Scatter Cones in the RHO-PHI System

Diagram showing the spherical triangle used to calculate the locations of the scatter cones in the RHO-PHI coordinate system.

$$c = \cos^{-1}(\cos a \cos b + \sin a \sin b \cos \gamma) \qquad 3.5$$

where: a and b = the length of the two remaining sides of the spherical triangle ABC shown in figure 3.5 (both equal to 57.3° in the case of the far east antenna), and

γ = the angle between sides a and b.

The expression for α in equation 3.4 is given by

$$\alpha = \sin^{-1}[\ \sin \gamma (\sin a \ / \ \sin c)] \qquad 3.6$$

Both equations 3.5 and 3.6 have been derived from expressions given for spherical triangles[19].

The program FLCONES.BAS steps the angle γ in increments of 10° and evaluates equations 3.5 and 3.6 to obtain the corresponding (ρ, ϕ) coordinates of the scatter cone in question. Table 3.2 lists the results of the calculations for the four feedlegs of the far east antenna. Figure 3.6 is a plot of the theoretical locations of the

TABLE 3.2

LOCATION OF THE FEEDLEG LOBES FOR THE FE ANTENNA

γ	α	Rho	Phi			
			Feedleg			
			N	E	S	W
10	87.3	8.4	92.7	182.7	272.7	2.7
20	84.6	16.8	95.4	185.4	275.4	5.4
30	81.8	25.2	98.2	188.2	278.2	8.2
40	78.9	33.5	101.1	191.1	281.1	11.1
50	75.9	41.7	104.1	194.1	284.1	14.1
60	72.7	49.8	107.3	197.3	287.3	17.3
70	69.3	57.7	110.7	200.7	290.7	20.7
80	65.6	65.5	114.4	204.4	294.4	24.4
90	61.6	73.0	118.4	208.4	298.4	28.4
100	57.2	80.3	122.8	212.8	302.8	32.8
110	52.3	87.2	127.7	217.7	307.7	37.7
120	46.9	93.6	133.1	223.1	313.1	43.1
130	40.8	99.4	139.2	229.2	319.2	49.2
140	34.0	104.5	146.0	236.0	326.0	56.0
150	26.4	108.7	153.6	243.6	333.6	63.6
160	18.1	111.9	161.9	251.9	341.9	71.9
170	9.2	113.9	170.8	260.8	350.8	80.8
180	0.0	114.6	180.0	270.0	360.0	90.0
190	-9.2	113.9	189.2	279.2	9.2	99.2
200	-18.1	111.9	198.1	288.1	18.1	108.1
210	-26.4	108.7	206.4	296.4	26.4	116.4
220	-34.0	104.5	214.0	304.0	34.0	124.0
230	-40.8	99.4	220.8	310.8	40.8	130.8
240	-46.9	93.6	226.9	316.9	46.9	136.9
250	-52.3	87.2	232.3	322.3	52.3	142.3
260	-57.2	80.3	237.2	327.2	57.2	147.2
270	-61.6	73.0	241.6	331.6	61.6	151.6
280	-65.6	65.5	245.6	335.6	65.6	155.6
290	-69.3	57.7	249.3	339.3	69.3	159.3
300	-72.7	49.8	252.7	342.7	72.7	162.7
310	-75.9	41.7	255.9	345.9	75.9	165.9
320	-78.9	33.5	258.9	348.9	78.9	168.9
330	-81.8	25.2	261.8	351.8	81.8	171.8
340	-84.6	16.8	264.6	354.6	84.6	174.6
350	-87.3	8.4	267.3	357.3	87.3	177.3

Note: Units for each column above are degrees.

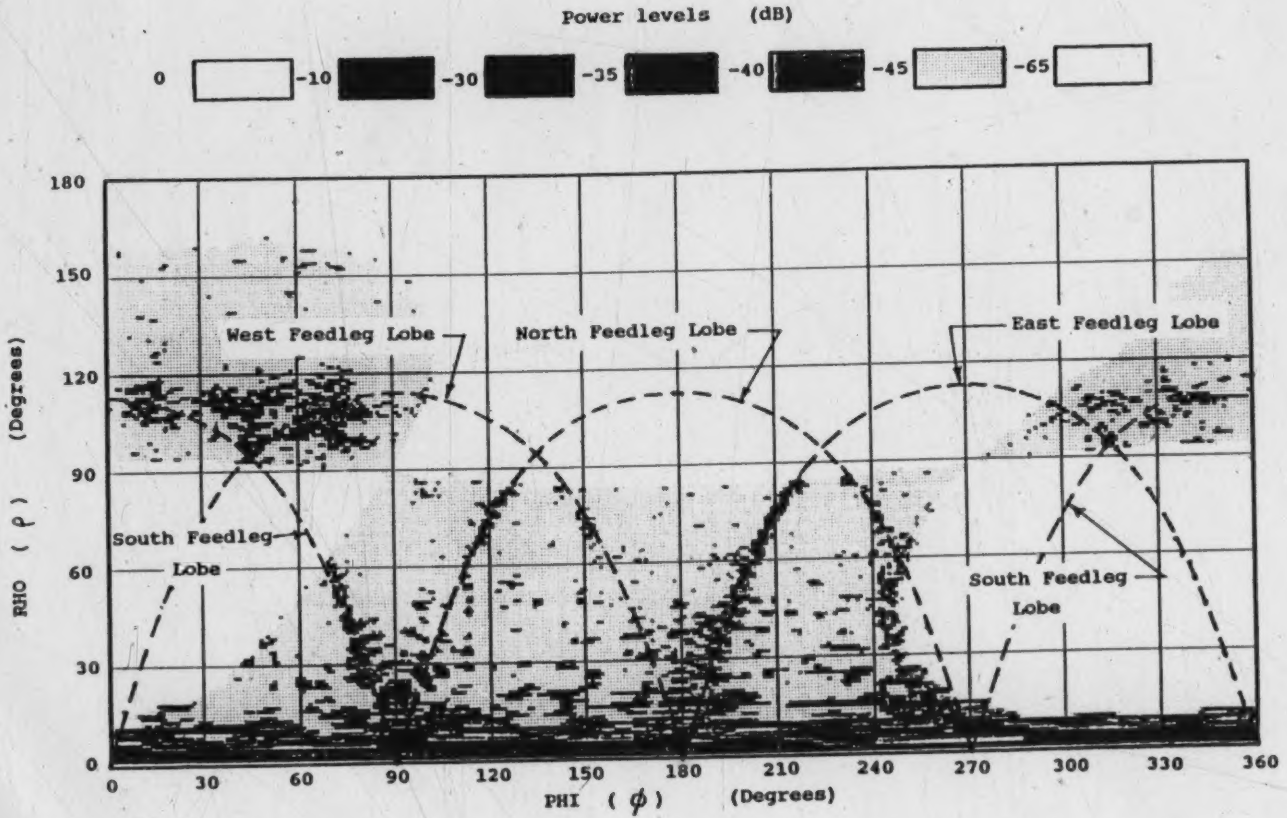

Figure 3.6
Theoretical Locations of the Feedleg Lobes
in the RHO-PHI System

The antenna pattern for the far east antenna displayed in the RHO-PHI (ρ , ϕ) coordinate system, with the theoretical locations of the feedleg lobes superimposed.

feedleg scatter cones, superimposed on the power pattern for the far east antenna. Excellent agreement exists between the measured and theoretical positions of the scatter cones.

2) WIDTH OF THE SCATTER CONES

The width of the scatter cone lobe is governed by the projected length of the feedleg. The expression for the approximate first-null to first-null width is given by[20]

$$\Delta\Theta \sim 2\lambda / (L \sin\beta) \qquad 3.7$$
$$= 2\lambda \,/\, \text{projected length}$$
$$= 2\lambda \,/\, \text{radius of the antenna}$$

where: β = the angle between the main beam and the axis of the feedleg,

L = the length of the feedleg (5.07 m for the far east antenna), and

λ = the wavelength of observation (.211 m)

($\Delta\Theta$ is approximately equal to twice the width of the main beam)

Equation 3.7 predicts a first-null to first-null width of 5.7°. The measured widths for the scatter cones can be obtained from the power pattern of the far east antenna shown in figure 2.8. A section of the scatter cone from the east feedleg was used for these measurements with cross-sections taken at ρ = 70, 75, and 80° between ϕ values of 200 and 220°. The cross-sections are plotted in figure 3.7. Table 3.3 is a summary of the measured widths of the scatter cones at both the -3 dB points, and at the first null points. The average of the first-null to first-null widths in table 3.3 closely matches the theoretical value of 5.7° predicted by equation 3.7.

3) AVERAGE POWER LEVELS IN THE SCATTER CONES

Assuming that the cross-sections plotted in figure 3.7 are representative of the scatter cones in the spillover region, one way of estimating the power levels is to assume that the average power in the cone is equal to the -3 dB level, which is -42 dB in this case. This appears to be a reasonable estimate, since most of the scatter cone lobes seen in figure 2.8 appear to fall in the range of -40 to - 45 dB.

A second method which may be used to estimate the

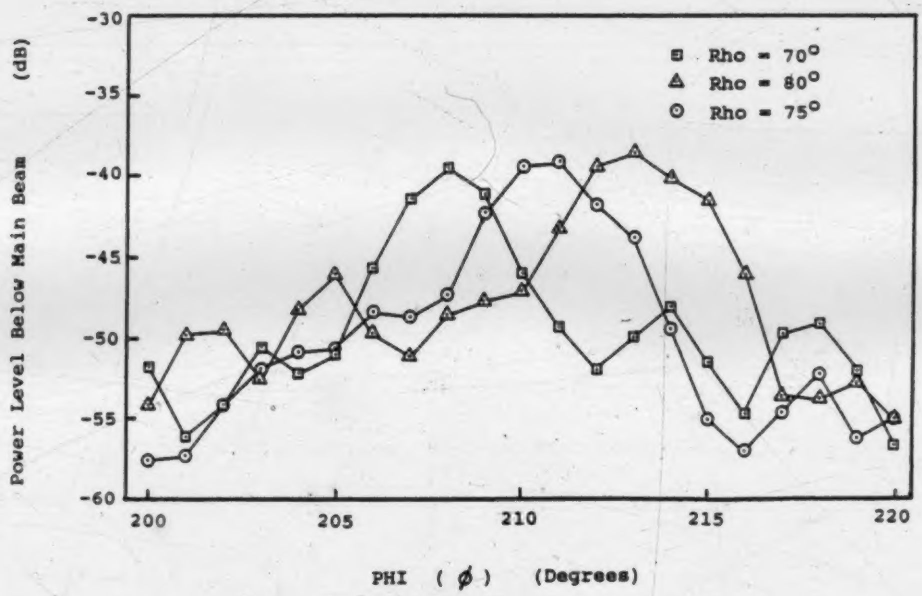

Figure 3.7 .
Cross-Sections Through the Feedleg Scatter Lobes

Cross-sections through the scatter cones from the east feedleg in the range 200° $\leq \phi \leq$ 220°.

TABLE 3.3
MEASURED WIDTHS OF SCATTER CONE LOBES FROM FAR EAST ANTENNA

(Measured from cross-sections through cone from east feedleg in $200^\circ \leq \phi \leq 220^\circ$)

CROSS-SECTION LOCATION (Degrees)	HPBW (Degrees)	1^{ST} NULL TO 1^{ST} NULL (Degrees)
70	2.1	4.2
75	2.7	5.4
80	3.0	6.0
Averages:	2.6	5.2

Note: 1^{st} null to 1^{st} null widths assumed to be twice the HPBW.

power levels in the scatter cones is the Induced Field Ratio (IFR) method. In this method the feedleg is considered to be an infinite cylinder immersed in a plane wave, and the scattering from the cylinder is calculated theoretically. The term IFR is defined from "When an infinite cylinder is immersed in an incident plane wave, its induced field ratio (IFR) is defined as the ratio of the forward-scattered field to the hypothetical field radiated in the forward direction by the plane wave in the reference aperture of width equal to the shadow of the geometrical cross section of the cylinder on the incident wavefront".[21]

Estimates of the power levels in the feedleg scatter lobes may be obtained by using the IFR design curves for circular shaped feedlegs shown in figures 3.8 and 3.9.[22] Figure 3.8 shows a plot of |IFR| values for circular metallic feedlegs as a function of the normalized width of the feedleg w' which is given by[23]

$$w' = w \cos(\gamma)/\lambda \qquad 3.8$$

where: w = the width of the feedleg,

γ = the angle that the feedleg makes with the

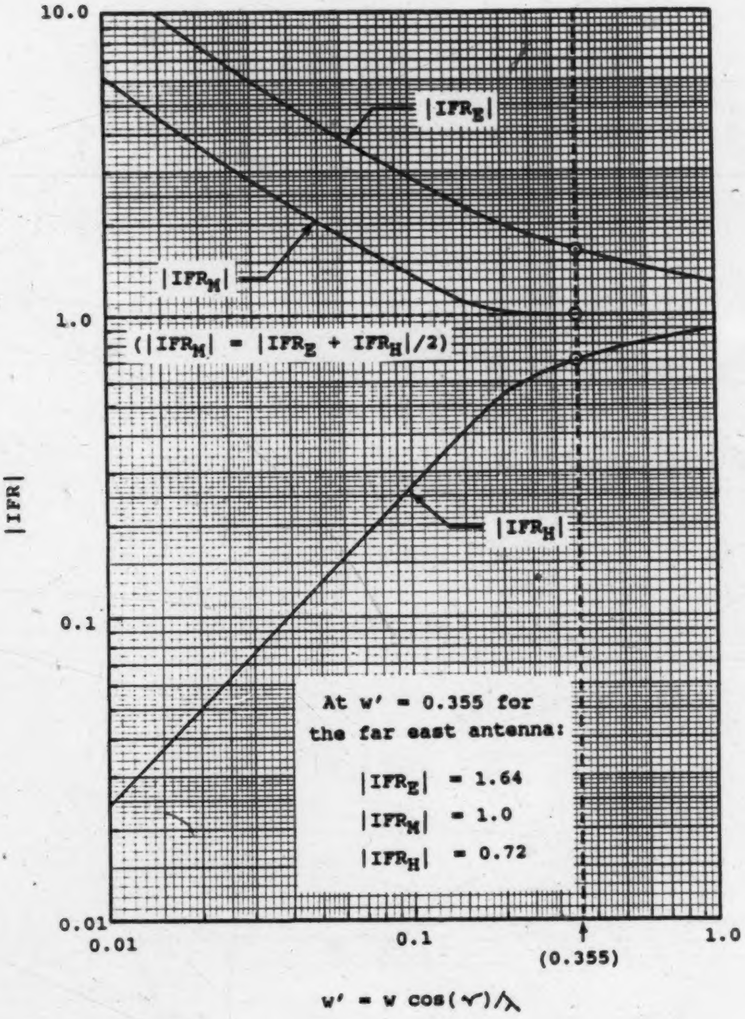

Figure 3.8
IFR Values for Metallic Cylinders

Plot of IFR values for metallic cylinders of width w, showing values of $|IFR_E|$, $|IFR_M|$, and $|IFR_H|$ for the far east antenna. (Adapted from Kildal, Olsen, and Aas.[22])

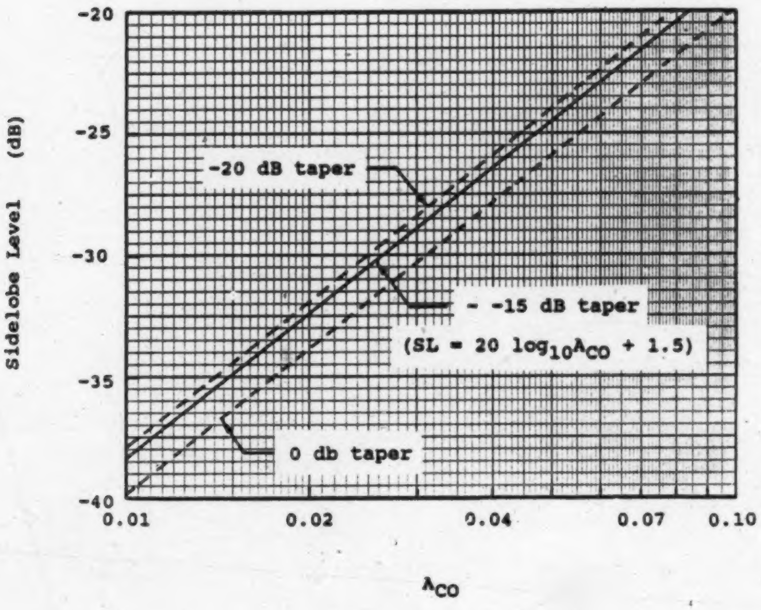

Figure 3.9
Sidelobe Levels as a Function of the Parameter λ_{CO}

Plot of asymptotic side lobe levels due to feedlegs for 0 dB, -15 dB and -20 dB tapers as a function of the parameter λ_{CO}. (Adapted from Kildal, Olsen, and Aas.[22])

aperture plane, and

λ = the wavelength of observation.

In the case of the far east antenna, w = 8.89 cm and $\gamma = 90^\circ - 57.3^\circ = 32.7^\circ$ (table 1.1), giving w'= 0.355 from equation 3.8. Then using figure 3.8, values of $|IFR_M| = 1.0$, $|IFR_E| = 1.64$, and $|IFR_H| = 0.72$ are found. The next step in using the design curves is to calculate the copolar side lobe level parameter A_{CO}, which is given by[24]

$$\begin{aligned} A_{CO} &= |IFR_i|\ (N_p\ w\ \rho_o / \pi \rho_o^2) \qquad 3.9 \\ &= |IFR_i|\ \text{(fractional blockage)} \end{aligned}$$

where: N_p = 1 when considering the effect of a single feedleg

w = the width of the feedlegs,

ρ_o = the radius of the antenna, and

$|IFR_i| = |IFR_M|$ for circular polarization,

$= |IFR_E|$ for linear polarization parallel to the projection of the feedleg,

$= |IFR_H|$ for linear polarization orthogonal to the projection of the feedleg,

$= |IFR_M|$ for linear polarization at 45° to the projection of the feedleg, identical to the value for circular polarization.

For the far east antenna, with circular polarization

$$A_{CO} = 1.0\ [\ (1)(8.89)/\pi(457)\ ] = 0.0062.$$

The sidelobe levels in the scatter cones are then obtained using figure 3.9, with the above value of A_{CO}. From the plot, a value of -42.7 dB is found, which nearly agrees with the measured value of -42 dB based on the cross sections shown in figure 3.7.

The above estimate using the IFR method is for circular polarization. However, linear (vertical) polarization was used for the measurement of the antenna pattern shown in figure 3.6, which has had the effect of giving the scatter cones a polarization dependence. For linear polarization, the values of $|IFR_i|$ in equation 3.9 become a function of the angle between the polarization and the projection of the feedleg. Polarization effects are clearly seen in the antenna pattern shown in figure 3.6, where the brightness of the feedleg scatter lobes is a function of the position along the cones.

The power levels in the scatter cones for linear polarization can be estimated by using values of $|IFR_E|$ and

$|IFR_H|$ found in figure 3.8 and following the procedure detailed above. When this is done, values of -38.4 dB and -45.5 dB are found for the power levels in the scatter cones for parallel and orthogonal projections of the feedleg to the polarization. As one moves the observation point along the locus of a scatter cone, the polarization becomes parallel and orthogonal to the projection of the feedleg two times, separated by 180°. Therefore for linear polarization, the IFR method predicts that the power levels in the cones should vary between ~ -38.4 dB and -45.5 dB, with two maxima and two minima along the length, with 90° separating the maximum and minimum. As well, the power level should be ~ -42.7 db, the same as the estimate for circular polarization at the point at which the projection of the feedleg is at 45° to the polarization. From figure 3.6, the power levels of the scatter cones appear to have maximum values just over -40 dB, and minima that blend in with the lower levels of the background radiation in the antenna pattern. The prediction therefore appears to be fairly accurate, and the scatter cones appear to go through the predicted alternate maxima and minima along their lengths.

For purposes of obtaining an estimate of the power levels in the feedleg scatter cones, the IFR estimate of -42.7 dB for circular polarization should be used, since the antennas receive circular as opposed to linear polarization. If circular polarization had been used in the measurement of the antenna pattern, the feedleg lobes would have had a much more uniform response along their loci, which would have enabled a more accurate determination of their power levels by direct measurement.

From the discussion above, estimates of ~-42 dB and ~ -42.7 dB have been obtained for the power levels in the scatter cones using the cross-sections shown in figure 3.7, and the IFR method for circular polarization. Since the estimate of -42 dB has been complicated by the use of linear polarization, the estimate of -42.7 dB for the power levels in the scatter cones is perhaps closer to the actual values present in the pattern, although both are in close agreement with each other. The error in this estimate is probably about ± 1 dB.

3.3.2 AN ESTIMATE OF ANTENNA TEMPERATURE DUE TO FEEDLEG SCATTER

With the location, width, and strength of the scatter cones characterized, an estimate can be made of their contribution to antenna temperature. From table 3.2, it is seen that the maximum value of ρ that the cones reach is

114.6°, which means that they clear the edge of the far east antenna at 118° by about 3.4°. Since the horizon is located at $\rho \sim 83^\circ$ one can determine the portion of the cone that intersects the ground. This value works out to be 0.423. Using a HPBW of 2.6°, and the value of -42.7 dB estimated from above for the power level in the cone, the solid angle of each of the four cones is approximately

$$\Omega_c \sim 0.423(\Delta\omega)P_c \qquad 3.10$$

where: 0.423 = the portion of the feedleg cone which strikes the ground,

$\Delta\omega = 2(\pi)\sin(\beta)\Delta\theta$; where $\Delta\theta$ is the width of the scatter cone (2.6°), and

P_c = the average power in the cone (-42.7 dB).

Evaluation of equation 3.10 using $P_c = -42.7$ dB gives

$$\Omega_c \sim 0.423(2\pi)\sin(57.3^\circ)(2.6/57.3)10^{-42.7/10},$$

$$\sim 5.45 \times 10^{-6} \text{ Sr} \quad \text{for each cone, or}$$

$\Omega_{Tc} \sim 2.18 \times 10^{-5}$ Sr in total for the four cones.

An estimate of antenna temperature due to the feedleg scatter lobes can then be found using equation 3.11 below.

$$T_{A\ cones} \sim \frac{\Omega_{Tc}}{\Omega_A}(T_G) \qquad 3.11$$

where: Ω_{Tc} = total solid angle in the cones which strike the ground,

Ω_A = solid angle of the antenna (~ 1.23×10^{-3} sr for the DRAO antennas), and

T_G = the effective ground temperature seen by the cones.

Using 213 K as the average value of effective ground temperature (determined from figure 2.14), evaluation of equation 3.11 gives 3.8 ± 1 K for the antenna temperature due to feedleg scatter.

If the estimate of -42.7 dB is representative of the lobes in the spillover region, the value of 3.8 ± 1 K is a significant addition that needs to be included in the estimate of antenna temperature shown in table 2.3. When added to the total in the table, the new estimate for antenna temperature is 23.6 ± 2.7 K, bringing it within the error estimates of the value of 25.9 ± 2.5 K which was measured in 1980.

For purposes of comparison, table 3.4 shows estimates of antenna temperature due to feedleg scatter for two effective ground temperatures, 300 K and 213 K. The table was generated for a range of average power levels using equation 3.10 and 3.11.

From the above discussion, it seems that the previous discrepancy between the theoretical and measured values of antenna temperature was the result of not considering the contribution to antenna temperature from feedleg scatter. Since it appears to be significant (~ 3.8 K) efforts should be made to try to reduce it.

3.3.3 REDUCTION OF ANTENNA TEMPERATURE BY MODIFYING THE SHAPE OF THE FEEDLEGS

In order to lower the contribution to antenna temperature caused by the feedleg scatter cones, it is necessary to prevent them from striking the ground when the antenna is pointed at the sky. Feedlegs with triangular

TABLE 3.4

ANTENNA TEMPERATURE FOR THE FAR EAST ANTENNA DUE TO THE FEEDLEG LOBES FOR A RANGE OF AVERAGE POWER LEVELS

(Given for ground temperatures of 300 K and 213 K)

Power Level (dB)	Antenna Temperature (K) (300)	(213)
-50.00	0.99	0.70
-49.00	1.24	0.88
-48.00	1.57	1.11
-47.00	1.97	1.40
-46.00	2.48	1.76
-45.00	3.13	2.22
-44.00	3.94	2.79
-43.00	4.95	3.52
-42.00	6.24	4.43
-41.00	7.85	5.58
-40.00	9.89	7.02
-39.00	12.45	8.84
-38.00	15.67	11.13
-37.00	19.73	14.01
-36.00	24.84	17.63
-35.00	31.27	22.20

shaped cross-sections have been employed on large earth station antennas to suppress the far sidelobe responses from feedleg scatter with good results[25]. To assess how effective this method would be when applied to the DRAO antennas, the cross-section of the feedlegs on the fifth antenna was changed from a circular to a triangular shape.

The method works by taking the power that was distributed in the cone, and concentrating it into two areas located along the locus of the original cone. The new locations of the scatter lobes are governed by the angle of incidence that the wave makes with the feedleg, and the half-vertex angle of the triangle which forms the feedleg. The direction of the scattered wave is given by[26]

$$\Phi = \tan^{-1}[1/(\cos\theta \tan\delta)] \qquad 3.12$$

and

$$\Theta = 2\sin^{-1}[\sin\theta \sin\delta] \qquad 3.13$$

where:

θ = the angle between the direction of the incident wave and the long axis of the feedleg, and

δ = the half-vertex angle of the triangular shaped feedleg.

The coordinates Φ and Θ , which are defined in figure 3.10, can be converted to the (ρ , ϕ) system by the following relationships to determine the new locations of the scatter lobes.

$$\phi = \phi_{fiq} + 180^{\circ} \pm \Phi \qquad 3.14$$

$$\rho = \Theta \qquad 3.15$$

where: ϕ_{fiq} = ϕ for the feedleg in question, (ie. 90° for the east feedleg with the antenna pointed at the zenith).

Table 3.5 lists the direction of the scatter lobes for triangular shaped feedlegs which have an angle of incidence equal to 57.3° (the same as the far east antenna), as a function of various half-vertex angles. The table demonstrates that as the half-vertex angle decreases, the scatter lobes move closer to the main beam direction. It is desirable to have the lobes close enough to the main beam so that they remain off the ground for a large portion of the zenith angles that the antennas can assume. For this reason a half-vertex angle of 15° was chosen for the shape of the wedges which were added to the feedlegs of the

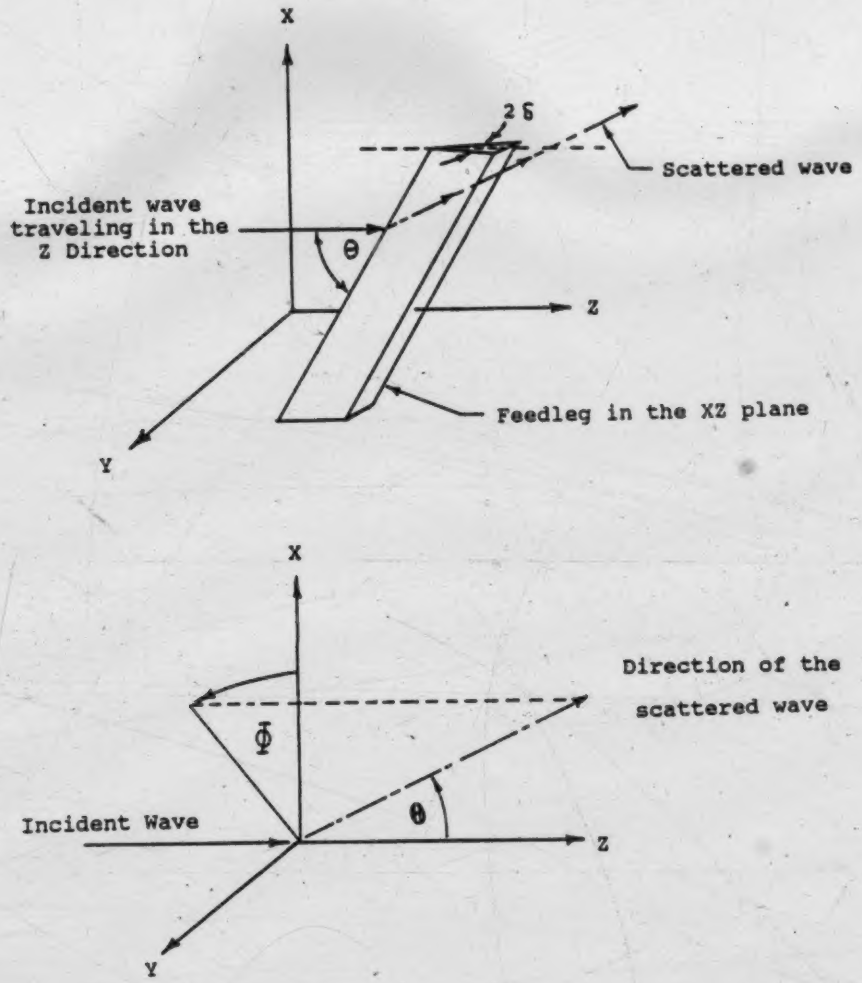
X
2δ
Scattered wave
Incident wave traveling in the Z Direction
θ
Z
Feedleg in the XZ plane
Y
X
Direction of the scattered wave
Φ
Incident Wave
θ
Z
Y

Figure 3.10
The Direction of the Scattered Wave
from a Triangular Feedleg

Diagram showing a triangular shaped feedleg in the XZ plane and the direction of the scattered wave. Φ is the angle from the the X axis (in the XY plane) to the scattered wave, and Θ is the angle to the direction of the scattered wave from the Z axis. (Adapted from Satoh et al.[25])

TABLE 3.5
THE DIRECTION OF THE SCATTERED WAVE FROM TRIANGULAR SHAPED FEEDLEGS FOR VARIOUS HALF-VERTEX ANGLES
(Angle of incidence: $\theta = 57.3^{\circ}$)

Half Vertex Angle	Direction of Scattered Wave	
δ	Θ	Φ
5.0	8.4	87.3
10.0	16.8	84.6
15.0	25.2	81.8
20.0	33.5	78.9
25.0	41.7	75.9
30.0	49.8	72.7
35.0	57.7	69.3
40.0	65.5	65.6
45.0	73.0	61.6
50.0	80.3	57.2
55.0	87.2	52.3
60.0	93.6	46.9
65.0	99.4	40.8
70.0	104.5	34.0
75.0	108.7	26.4
80.0	111.9	18.1
85.0	113.9	9.2
90.0	114.6	0.0

Note: All the above values are given in degrees.

fifth antenna. This angle along with the fixed angle of incidence of 57.3°, places the scatter lobes at $(\Theta, \Phi) = (25.2^{\circ}, 81.8^{\circ})$, the values in the third row of table 3.5. For these values, the zenith angle would have to approach ~ 60° before the centers of the scatter lobes began to intersect the ground.

If the directions of the scatter lobes listed in table 3.5 are plotted (shown in figure 3.11), it is seen that their locations are along the locus of the cone which is scattered from a circular shaped feedleg, given the same angle of incidence. The circular shaped feedleg is equivalent to having the half-vertex angle δ continuously varied from 0° to 180°, which results in the radiation being scattered along the cone, rather than being concentrated in two areas as it is for a fixed half-vertex angle.

A further improvement to the triangular shaped feedlegs can be made. It has been found that a feedleg with a saw-tooth plate attached to the pointed triangular edge facing the reflector is more effective at suppressing the far sidelobes than is the triangular shape by itself[27]. The triangular feedleg still has a linear edge along its vertex which will cause some energy to be scattered into the original cone. With the saw-tooth plate added, the incident wave now sees a half-vertex angle of ~ 0° along

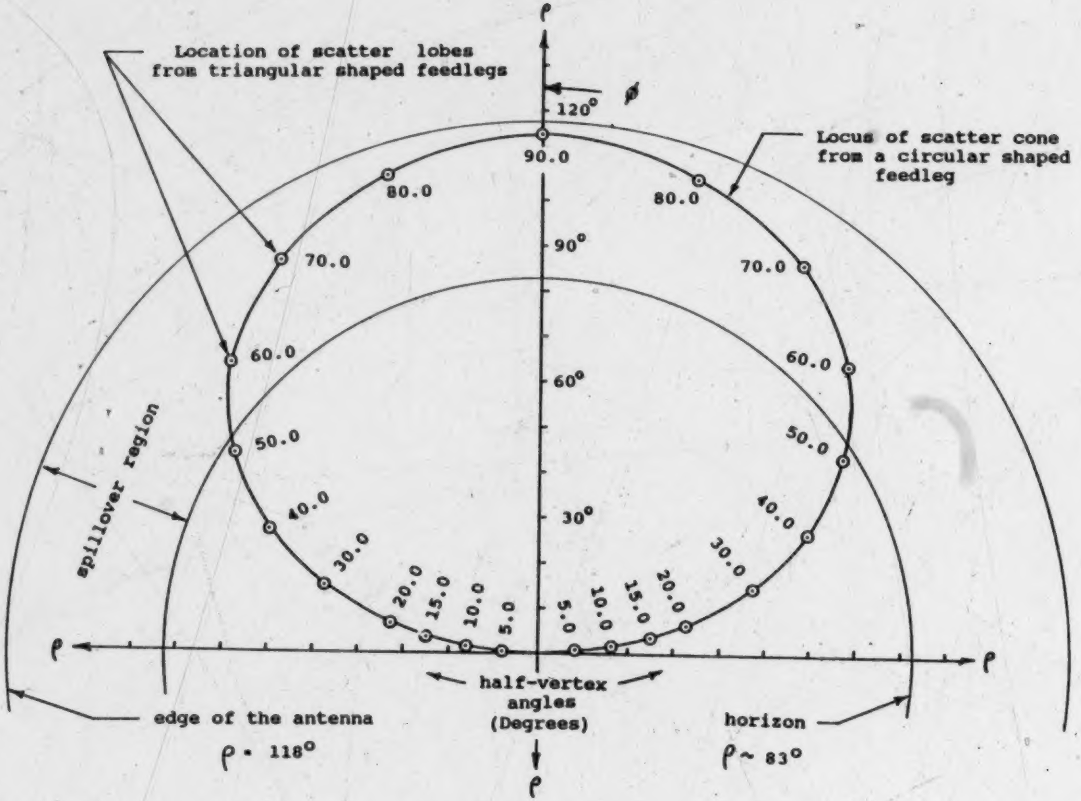

Figure 3.11
Direction of the Scattered Wave for Various Half-Vertex Angles

Location of the centers of the scatter lobes for various half-vertex angles of triangular shaped feedlegs with an angle of incidence of 57.3°. Coordinate system is a polar plot of the (ρ, ϕ) system.

the axis of the feedleg, so the scattered wave should have its peaks in the vicinity of the main beam. But the energy will now be scattered in rings with radii determined by the new angle θ' that the edges of the teeth make with the incoming wave. For the reasons discussed above, it was decided to add teeth to the feedlegs of the fifth antenna as well. They were designed so that the incident wave would strike the sides of the teeth at an angle of 17.3°, which would result in scatter cones which would intersect the main beam and have a maximum distance from the main beam of $\sim 34.6^{\circ}$. Figure 3.12 shows the details of the triangular cross section and the teeth which were added to the feedlegs of the fifth antenna. To be effective, the dimensions were chosen to be greater than the wavelength of observation, 21.1 cm.

The modifications to the feedlegs were added to the antenna, and measurements of antenna temperature were taken to judge their effectiveness. The first set of measurements was done with both the fence and the feedleg modifications in place, then a second set was obtained after the fence had been removed, giving results for the feedleg modifications alone. The two sets of measurements are listed in table 3.6.

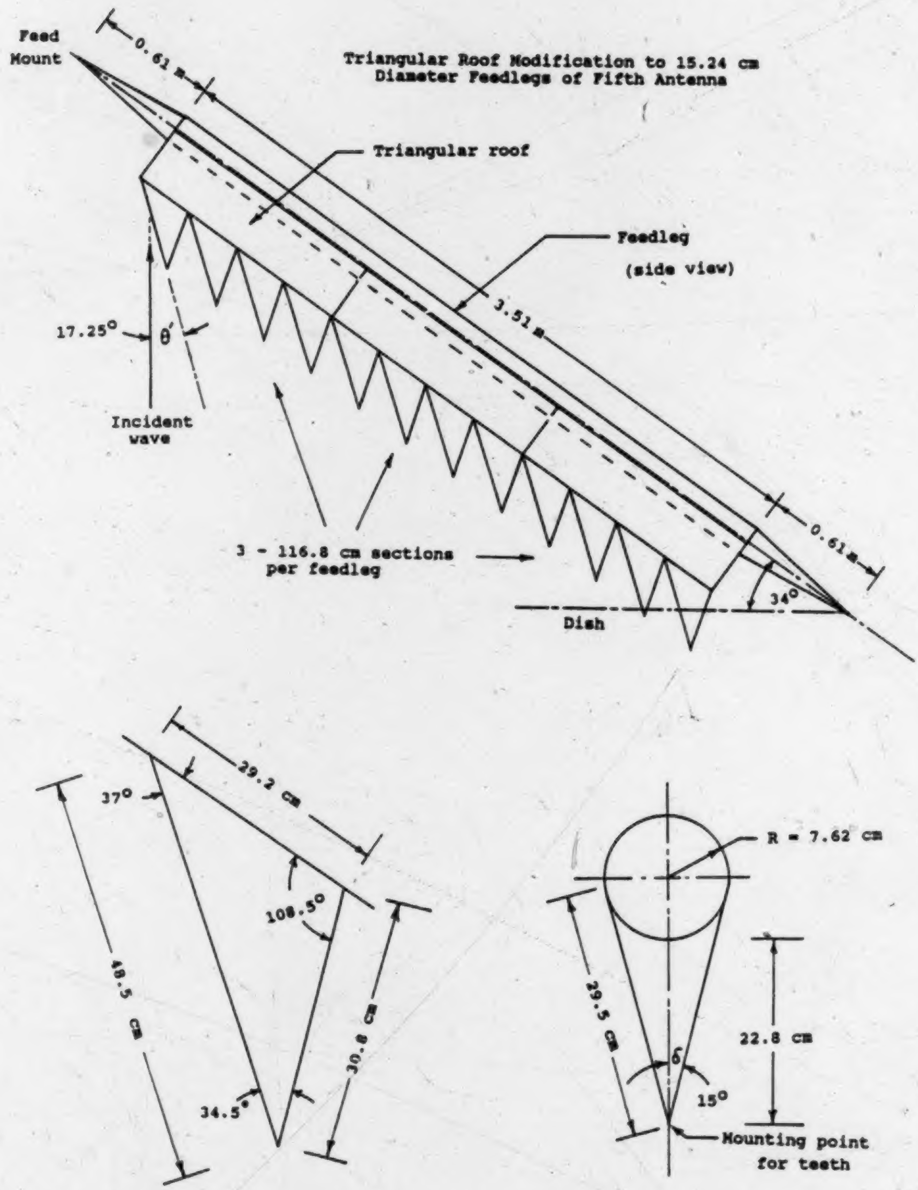

Tooth Design (side view)

Design of Triangular Roof
(cross-section)

Figure 3.12

The Modifications Added to the Feedlegs
of the Fifth Antenna.

TABLE 3.6
ANTENNA TEMPERATURE MEASUREMENTS FOR THE FIFTH ANTENNA AT THE ZENITH WITH FEEDLEG AND FENCE MODIFICATIONS

Date (1987)	Ambient Temperature (°C)	Antenna Config.*		Antenna Temperature (K)
Aug. 18	26.0	3		14.0
		3		19.8
		3		17.7
		3		16.2

			Ave:	16.9 ± 1.2 K
Aug. 20	20.4	4		21.5
		4		20.7
		4		24.3
		4		18.2

			Ave:	21.2 ± 1.3 K

* 3: Antenna with fence and the feedleg modifications.
4: Antenna with the feedleg modifications only.

Note: The ± errors listed are standard errors (α) given by equation 3.2.

3.3.4 RESULTS

The measurements listed for August 18, 1987 in table 3.6 give an antenna temperature of 16.9 ± 1.2 K for the fifth antenna with both the fence and the feedleg modifications in place. This represents a 1.1 ± 1.2 K improvement over the antenna temperature with the fence alone (table 3.1). The relatively small improvement using the feedleg modifications in conjunction with the fence is due to the fence acting to keep a large portion of the feedleg lobes from striking the ground. The measurements were performed on the fifth antenna , but the same fence placed on the far east antenna should have a similar effect. The fence would subtend an angle of about 10°, putting its top edge at $\rho \sim 108^{\circ}$, which would reduce the portion of the feedleg lobes that strike the ground to ~ 0.25 Sr from 0.42 Sr. The portion that remains would strike the ground at a shallow angle of incidence, and would therefore cause a smaller contribution to antenna temperature due to the lower effective ground temperature.

To assess the effect that the feedleg modifications had by themselves, a group of four measurements was obtained on August 20, 1987, after the fence had been removed. These are listed in table 3.6, and have an average of 21.2 ± 1.3 K, which represents a 5.1 ± 1.3 K improvement on the antenna with no modifications (see section 3.2). The results in table 3.6 show that changing the shape of the feedlegs has a significant effect on lowering the antenna temperature of the antennas that make up the synthesis telescope at DRAO.

3.4 FEEDLEG SCATTER AS A FUNCTION OF SIZE, CONFIGURATION, AND MATERIAL OF THE FEEDLEGS

The estimate of antenna temperature in section 3.3.2 obtained by using the IFR method was made for the far east antenna which has a quadrupod arrangement of feedlegs, with widths of 8.89 cm. The same method can be used to predict what effect a change in feedleg diameter will have, for both a tripod and quadrupod arrangement. As well, the effect of changing the feedleg material from a metal to a dielectric can be found for the same range of diameters, for both support structures. The IFR method described above has been used to generate three sets of tables which predict antenna temperature due to feedleg scatter for the above variations. It should be noted that the IFR design curve method used here, and in section 3.3.2, can be used to describe scattering from a feedleg when approximately[28]

$$\sin \rho < \lambda / 2w \qquad 3.16$$

where: ρ = the angle from the main beam,
λ = the wavelength of observation, and
w = the width of the feedleg.

Therefore in the tables, as the width of the feedlegs increases, the range of angles from the main beam for which accurate predictions can be obtained decreases. The tables list antenna temperatures for feedleg diameters up to 20 cm which allows estimates for the DRAO antennas which have feedlegs in a tripod arrangement (diameters of 15.2 cm). However, predictions for the larger feedleg diameters probably become increasingly unreliable, since the power estimates obtained have been applied to areas outside those given by equation 3.16. But the results for feedleg diameters of ~ 10 cm and less should be accurate, which makes it possible to do comparisons between the tables for these sizes.

The first column of each table lists the width of the feedleg. The second gives the normalized width obtained from equation 3.8. The column headed with F has the values of the multiplier of IFR from equation 3.9. The product of IFR (from figure 3.8) and F gives A_{CO}, which then is used with figure 3.9 to give the sidelobe levels in the cones. Then the solid angle of the cones striking the ground Ω_{CG}, was calculated and used in equation 3.11 to obtain the estimate of antenna temperature due to feedleg scatter.

Tables 3.7 and 3.8 give estimates of antenna temperature for an antenna with metallic feedlegs in a tripod and quadrupod arrangement for antenna diameters of 8.53 and 9.14 m respectively. The estimates of antenna temperature for the tripod predict a lower value than that of a quadrupod, for a given diameter of feedleg. For instance, table 3.7 and 3.8 predict a 16 percent reduction of antenna temperature for the far east antenna if the same size feedlegs were used in a tripod configuration on the 8.53 m antennas. This would give about 3.3 K, if feedleg scatter contributes 3.8 K to antenna temperature on the 9.14 m antenna with a quadrupod arrangement of feedlegs. Currently, the antennas with the tripods have feedleg diameters of 15.2 cm. If narrower feedlegs are able to support the focus box of the quadrupod antennas in a tripod arrangement, a lowering of antenna temperature should be the result. Table 3.7 predicts that the antennas with the tripods should have contributions to antenna temperature of ~ 9.6 K for feedleg diameters of 15.2 cm. But this estimate is probably in error since the conditions given in equation 3.16 have been violated.

TABLE 3.7

ESTIMATES OF ANTENNA TEMPERATURE DUE TO TRIPOD FEEDLEG ARRANGEMENT USING IFR METHOD (angle of incidence = 57.3°, average ground temperature = 213 K, antenna dia. = 8.53 m.)

w (cm)	w' (cm)	F	IFR	Power level (dB)	Ω_{CG}	T_A (K)
1	0.040	0.0007	2.33	-53.68	0.130E-05	0.23
2	0.080	0.0015	1.50	-51.51	0.215E-05	0.37
3	0.120	0.0022	1.23	-49.66	0.328E-05	0.57
4	0.160	0.0030	1.12	-48.05	0.477E-05	0.83
5	0.200	0.0037	1.05	-46.61	0.663E-05	1.15
6	0.239	0.0045	1.02	-45.33	0.891E-05	1.54
7	0.279	0.0052	1.00	-44.17	0.116E-04	2.01
8	0.319	0.0060	1.00	-42.97	0.153E-04	2.66
9	0.359	0.0067	1.00	-41.95	0.194E-04	3.36
10	0.399	0.0075	1.00	-41.03	0.240E-04	4.15
11	0.439	0.0082	1.00	-40.21	0.290E-04	5.02
12	0.479	0.0090	1.00	-39.45	0.345E-04	5.97
13	0.519	0.0097	1.00	-38.76	0.405E-04	7.01
14	0.559	0.0104	1.00	-38.11	0.470E-04	8.13
15	0.599	0.0112	1.00	-37.51	0.539E-04	9.34
16	0.638	0.0119	1.00	-36.95	0.613E-04	10.62
17	0.678	0.0127	1.00	-36.43	0.692E-04	11.99
18	0.718	0.0134	1.00	-35.93	0.776E-04	13.44
19	0.758	0.0142	1.00	-35.46	0.865E-04	14.98
20	0.798	0.0149	1.00	-35.01	0.958E-04	16.60

TABLE 3.8

ESTIMATES OF ANTENNA TEMPERATURE DUE TO QUADRUPOD FEEDLEG ARRANGEMENT USING IFR METHOD (angle of incidence = 57.3°, average ground temperature = 213 K, antenna dia. = 9.14 m.)

W (cm)	w' (cm)	F	IFR	Power level (dB)	Ω_{CG}	T_A (K)
1	0.040	0.0007	2.33	-54.28	0.151E-05	0.26
2	0.080	0.0014	1.50	-52.11	0.249E-05	0.43
3	0.120	0.0021	1.23	-50.26	0.381E-05	0.66
4	0.160	0.0028	1.12	-48.65	0.553E-05	0.96
5	0.200	0.0035	1.05	-47.21	0.770E-05	1.33
6	0.239	0.0042	1.02	-45.93	0.103E-04	1.79
7	0.279	0.0049	1.00	-44.77	0.135E-04	2.34
8	0.319	0.0056	1.00	-43.57	0.178E-04	3.08
9	0.359	0.0063	1.00	-42.55	0.225E-04	3.90
10	0.399	0.0070	1.00	-41.63	0.278E-04	4.82
11	0.439	0.0077	1.00	-40.81	0.337E-04	5.83
12	0.479	0.0084	1.00	-40.05	0.401E-04	6.94
13	0.519	0.0091	1.00	-39.36	0.470E-04	8.14
14	0.559	0.0098	1.00	-38.71	0.545E-04	9.44
15	0.599	0.0104	1.00	-38.11	0.626E-04	10.84
16	0.638	0.0111	1.00	-37.55	0.712E-04	12.33
17	0.678	0.0118	1.00	-37.03	0.804E-04	13.92
18	0.718	0.0125	1.00	-36.53	0.901E-04	15.61
19	0.758	0.0132	1.00	-36.06	0.100E-03	17.39
20	0.798	0.0139	1.00	-35.61	0.111E-03	19.27

Tables 3.9 and 3.10 give the predictions for feedlegs made from glass-fiber reinforced polyester (70 percent by weight glass content) with a relative dielectric constant of 5.2. Tables 3.11 and 3.12 give the same information for polystyrene with a relative dielectric constant of 2.5. The dielectric feedlegs are hollow tubes with a thickness equal to 0.15 of their width. Again, the same percentage improvement is seen when going from the quadrupod to tripod arrangement for feedlegs of a given diameter. The IFR values for the dielectric were obtained by fitting fourth order polynomials to the design curves published by Kildal et al.[29]

The information contained in tables 3.7 to 3.12 is summarized in figure 3.13. It is a plot of the antenna temperature produced by the dielectric feedlegs divided by the antenna temperature which results from metallic feedlegs of the same diameter. The plot shows that the feedlegs made from polystyrene ($\epsilon_r = 2.5$) are superior to those made from fiberglass ($\epsilon_r = 5.2$). The plot also shows that fiberglass feedlegs are preferable to metallic ones for sizes up to about 6.2 cm, and that polystyrene is better than metal for sizes up to about 16 cm. The strength of dielectric feedlegs would have to be determined and compared to aluminum ones, to see if a switch to a dielectric material would be possible.

TABLE 3.9
ESTIMATES OF ANTENNA TEMPERATURE DUE TO TRIPOD OF DIELECTRIC FEEDLEGS USING IFR METHOD

(angle of incidence = 57.3°, average ground temp. = 213 K, relative epsilon = 5.2, antenna diameter = 8.53 m.)

w (cm)	w' (cm)	F	IFR	Power level (dB)	Ω_{CG}	T_A (K)
1	0.040	0.0007	0.16	-77.02	0.603E-08	0.00
2	0.080	0.0015	0.32	-64.87	0.989E-07	0.02
3	0.120	0.0022	0.49	-57.60	0.528E-06	0.09
4	0.160	0.0030	0.67	-52.48	0.172E-05	0.30
5	0.200	0.0037	0.84	-48.60	0.420E-05	0.73
6	0.239	0.0045	0.99	-45.54	0.849E-05	1.47
7	0.279	0.0052	1.13	-43.06	0.150E-04	2.60
8	0.319	0.0060	1.25	-41.01	0.241E-04	4.17
9	0.359	0.0067	1.36	-39.30	0.357E-04	6.18
10	0.399	0.0075	1.44	-37.86	0.497E-04	8.61
11	0.439	0.0082	1.51	-36.64	0.659E-04	11.42
12	0.479	0.0090	1.56	-35.60	0.838E-04	14.51
13	0.519	0.0097	1.59	-34.71	0.103E-03	17.81
14	0.559	0.0104	1.62	-33.95	0.123E-03	21.21
15	0.599	0.0112	1.62	-33.30	0.142E-03	24.63
16	0.638	0.0119	1.62	-32.75	0.162E-03	27.97
17	0.678	0.0127	1.61	-32.28	0.180E-03	31.14
18	0.718	0.0134	1.59	-31.89	0.197E-03	34.09
19	0.758	0.0142	1.57	-31.56	0.212E-03	36.75
20	0.798	0.0149	1.53	-31.29	0.226E-03	39.09

TABLE 3.10
ESTIMATES OF ANTENNA TEMPERATURE DUE TO QUADRUPOD OF DIELECTRIC FEEDLEGS USING IFR METHOD

(angle of incidence = 57.3°, average ground temp. = 213 K, relative epsilon = 5.2, antenna diameter = 9.14 m.)

w (cm)	w' (cm)	F	IFR	Power level (dB)	Ω_{CG}	T_A (K)
1	0.040	0.0007	0.16	-77.62	0.700E-08	0.00
2	0.080	0.0014	0.32	-65.47	0.115E-06	0.02
3	0.120	0.0021	0.49	-58.20	0.613E-06	0.11
4	0.160	0.0028	0.67	-53.08	0.199E-05	0.35
5	0.200	0.0035	0.84	-49.20	0.487E-05	0.84
6	0.239	0.0042	0.99	-46.14	0.986E-05	1.71
7	0.279	0.0049	1.13	-43.66	0.175E-04	3.02
8	0.319	0.0056	1.25	-41.61	0.280E-04	4.84
9	0.359	0.0063	1.36	-39.90	0.415E-04	7.18
10	0.399	0.0070	1.44	-38.46	0.578E-04	10.00
11	0.439	0.0077	1.51	-37.24	0.766E-04	13.26
12	0.479	0.0084	1.56	-36.20	0.973E-04	16.85
13	0.519	0.0091	1.59	-35.31	0.119E-03	20.68
14	0.559	0.0098	1.62	-34.55	0.142E-03	24.64
15	0.599	0.0104	1.62	-33.90	0.165E-03	28.60
16	0.638	0.0111	1.62	-33.35	0.188E-03	32.48
17	0.678	0.0118	1.61	-32.88	0.209E-03	36.17
18	0.718	0.0125	1.59	-32.49	0.229E-03	39.59
19	0.758	0.0132	1.57	-32.16	0.246E-03	42.68
20	0.798	0.0139	1.53	-31.89	0.262E-03	45.40

TABLE 3.11
ESTIMATES OF ANTENNA TEMPERATURE DUE TO TRIPOD OF DIELECTRIC FEEDLEGS USING IFR METHOD

(angle of incidence = 57.3°, average ground temp. = 213 K, relative epsilon = 2.5, antenna diameter = 8.53 m.)

w (cm)	w' (cm)	F	IFR	Power level (dB)	Ω_{CG}	T_A (K)
1	0.040	0.0007	0.06	-84.85	0.994E-09	0.00
2	0.080	0.0015	0.12	-73.08	0.149E-07	0.00
3	0.120	0.0022	0.19	-65.94	0.773E-07	0.01
4	0.160	0.0030	0.26	-60.77	0.254E-06	0.04
5	0.200	0.0037	0.33	-56.74	0.644E-06	0.11
6	0.239	0.0045	0.40	-53.45	0.137E-05	0.24
7	0.279	0.0052	0.47	-50.69	0.259E-05	0.45
8	0.319	0.0060	0.54	-48.33	0.446E-05	0.77
9	0.359	0.0067	0.61	-46.28	0.715E-05	1.24
10	0.399	0.0075	0.67	-44.48	0.108E-04	1.88
11	0.439	0.0082	0.73	-42.88	0.156E-04	2.71
12	0.479	0.0090	0.79	-41.46	0.217E-04	3.77
13	0.519	0.0097	0.85	-40.17	0.292E-04	5.06
14	0.559	0.0104	0.90	-39.01	0.382E-04	6.61
15	0.599	0.0112	0.95	-37.96	0.487E-04	8.43
16	0.638	0.0119	1.00	-37.00	0.607E-04	10.52
17	0.678	0.0127	1.04	-36.12	0.743E-04	12.87
18	0.718	0.0134	1.07	-35.31	0.895E-04	15.50
19	0.758	0.0142	1.11	-34.57	0.106E-03	18.37
20	0.798	0.0149	1.14	-33.89	0.124E-03	21.49

TABLE 3.12
ESTIMATES OF ANTENNA TEMPERATURE DUE TO QUADRUPOD OF DIELECTRIC FEEDLEGS USING IFR METHOD

(angle of incidence = 57.3°, average ground temp. = 213 K, relative epsilon = 2.5, antenna diameter = 9.14 m.)

w (cm)	w' (cm)	F	IFR	Power level (dB)	Ω_{CG}	T_A (K)
1	0.040	0.0007	0.06	-85.45	0.115E-08	0.00
2	0.080	0.0014	0.12	-73.68	0.173E-07	0.00
3	0.120	0.0021	0.19	-66.54	0.898E-07	0.02
4	0.160	0.0028	0.26	-61.37	0.295E-06	0.05
5	0.200	0.0035	0.33	-57.34	0.747E-06	0.13
6	0.239	0.0042	0.40	-54.05	0.159E-05	0.28
7	0.279	0.0049	0.47	-51.29	0.301E-05	0.52
8	0.319	0.0056	0.54	-48.93	0.518E-05	0.90
9	0.359	0.0063	0.61	-46.88	0.830E-05	1.44
10	0.399	0.0070	0.67	-45.08	0.126E-04	2.18
11	0.439	0.0077	0.73	-43.48	0.182E-04	3.15
12	0.479	0.0084	0.79	-42.06	0.252E-04	4.37
13	0.519	0.0091	0.85	-40.77	0.339E-04	5.88
14	0.559	0.0098	0.90	-39.61	0.443E-04	7.68
15	0.599	0.0104	0.95	-38.56	0.565E-04	9.79
16	0.638	0.0111	1.00	-37.59	0.705E-04	12.21
17	0.678	0.0118	1.04	-36.72	0.863E-04	14.95
18	0.718	0.0125	1.07	-35.91	0.104E-03	18.00
19	0.758	0.0132	1.11	-35.17	0.123E-03	21.34
20	0.798	0.0139	1.14	-34.49	0.144E-03	24.96

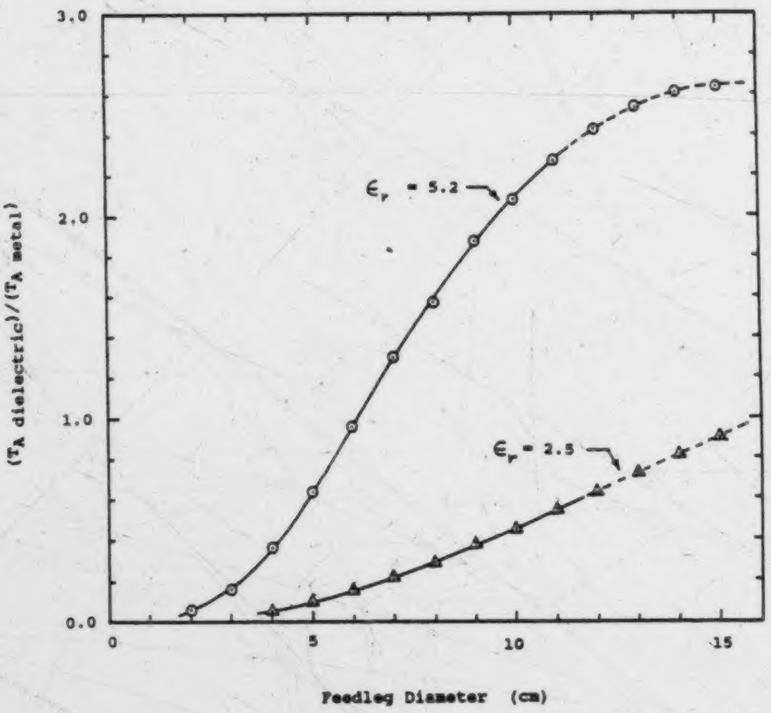

Figure 3.13
Comparison of Metallic and Dielectric Feedlegs

Plot of $(T_{A\ \mathrm{dielectric}})/(T_{A\ \mathrm{metal}})$ as a function of feedleg diameter for an angle of incidence = 57.3°.

3.5 SUMMARY OF THE ANTENNA WORK

The experiments performed on the far east antenna have given results that fall into two main areas. The first is the satisfactory explanation of the measurements of antenna temperature (~ 25K to 26 K) for the antennas of the synthesis telescope. The second is in the area of lowering the antenna temperature of the antennas. The experiments with the fence and the feedleg modifications have demonstrated that the antenna temperature can be lowered significantly with fairly simple modifications to the antennas.

3.5.1 ANTENNA MEASUREMENT DISCREPANCY EXPLAINED

At the beginning of this work, estimates of antenna temperature were made by adding up the contributions made from the various sources listed in table 2.3. The total for these estimates was about 20 K, approximately 5 or 6 K lower than the value of ~ 26 K which had been previously measured.

The experiments performed on the fifth antenna have shown that the difference between the two values of antenna temperature can be explained by the scatter lobes from the feedlegs hitting the ground. The contribution from this source accounts for most of the missing 5 or 6 K.

Table 3.13 is a summary of estimates and measurements of antenna temperature for the synthesis telescope. The first entry of 19.8 ± 2.5 K is the estimate from table 2.3 which does not include feedleg scatter. If the estimate for feedleg scatter (section 3.3.2) is included, the antenna temperature becomes 23.6 ± 2.7 K, as shown by item two in the table. This value agrees reasonably well with the two measured values of 25.9 ± 2.5 K and 26.3 ± 2.5 K, items five and six respectively of table 3.13.

Item three in the table shows an antenna temperature of 24.6 ± 2.5 K. It was arrived at by a method which uses the measurement of the antenna temperature of the fifth antenna with the feedleg modifications (21.2 ± 1.3 K), and without them (26.3 ± 0.3 K). The two measurements show that a minimum of 19.4 percent of the total antenna temperature can be attributed to feedleg scatter. Using this and assuming that the contributions listed in table 2.3 form 80.6 percent of the total, the additional 19.4 percent due to feedleg scatter gives 24.6 ± 2.5 K for the antenna temperature of the antennas similar in design to the fifth antenna. The estimate is based on the assumption that the feedleg modifications have completely eliminated

TABLE 3.13

COMPARISON OF ESTIMATES AND MEASUREMENTS OF ANTENNA TEMPERATURE FOR THE ANTENNAS OF THE SYNTHESIS TELESCOPE

	Details	Antenna Temperature
1.	Estimate from table 2.3 (Without feedleg scatter)	19.8 ± 2.5 K
2.	Estimate from table 2.3 (Including feedleg scatter)	23.6 ± 2.7 K
3.	Estimate from table 2.3 including 19.4 % for feedleg scatter	24.6 ± 2.5 K
4.	Integration of far east antenna pattern	27.6 ± 3.0 K
5.	Measured in 1980 (Far east antenna)	25.9 ± 2.5 K
6.	Measured in 1987 (Fifth antenna)	26.3 ± 2.5 K

the contribution to antenna temperature by the feedleg lobes. The estimate of 24.6 K is slightly below but still within the error bars of the two values which were measured in 1980 and 1987.

The fourth item of the table is an estimate of antenna temperature based on integrating the antenna pattern of the far east antenna (figure 2.8). It gives 27.6 ± 3.0 K which is slightly above the measured values but again still within the uncertainty. The value of 27.6 K is made up of 13.96 K for spillover and feedleg scatter, 6.48 K for leakage and diffraction (both from figure 2.16), and estimates of 5.0 K and 2.2 K for the contributions from the sky and atmosphere respectively. These are in fairly good agreement with the estimates of the individual contributors listed in table 2.3, if the addition of 3.8 ± 1 K for the feedleg scatter is included in the table.

The first two estimates of table 3.13 apply to both the far east and fifth antennas, whereas the third estimate would apply more to the fifth antenna. Also, the error of ± 2.5 K given for item number 6 is larger than the error listed in table 3.1 (± 0.3 K), to account for possible systematic errors in the measurement. The values listed in tables 3.1 and 3.6 are used to find differences in antenna temperature, and therefore the systematic errors should cancel.

The general agreement of items two to six in table 3.13 indicates that the effects of the individual contributors to antenna temperature are known fairly accurately. It also shows that the antenna temperatures of the far east and the fifth antennas are essentially the same. Figure 3.14 shows a summary of the individual components of antenna temperature based on table 2.3, the measurements obtained from the fifth antenna, and the measurement of the power pattern of the far east antenna. It gives the best estimate of the breakdown of the antenna temperature for the antennas of the synthesis telescope at DRAO, assuming an antenna temperature = 26.0 K.

3.5.2 RESULTS OF THE ANTENNA MODIFICATIONS

The second area that has been explored is the reduction of antenna temperature due to spillover and feedleg scatter. The experiments with the fence and feedleg modifications have shown that significant gains in sensitivity can be achieved by implementing the fence or the feedleg modifications.

Table 3.14 gives a summary of the antenna temperature measurements performed on the fifth antenna. From the

Far East Antenna

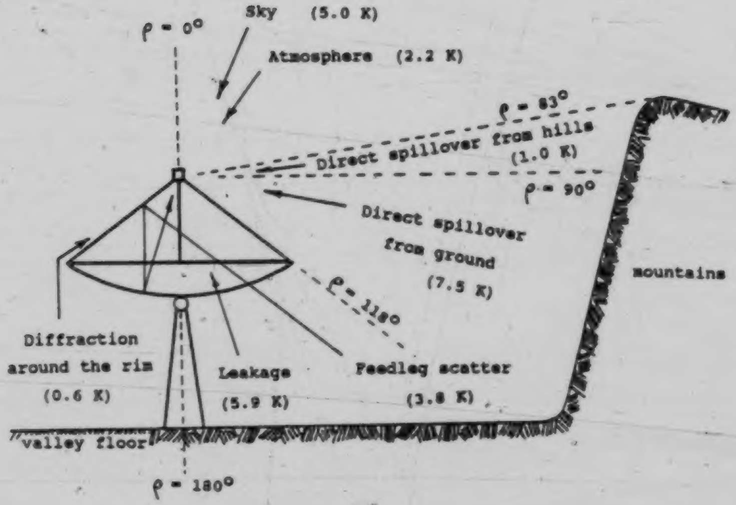

Fifth Antenna

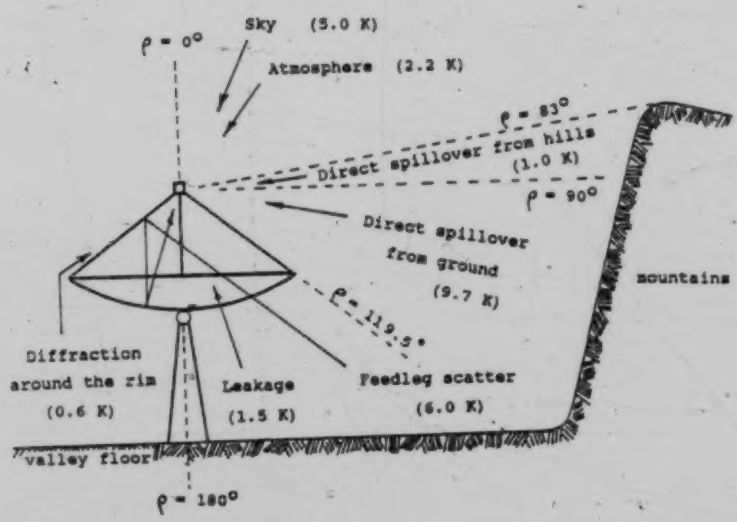

Figure 3.14
Contributors to Antenna Temperature

Estimation of the individual contributors to antenna temperature for the far east and fifth antennas at DRAO, assuming an antenna temperature = 26.0 K in both cases.

TABLE 3.14 SUMMARY OF ANTENNA TEMPERATURE MEASUREMENTS
(fifth antenna)

	Antenna Configuration	T_A (K)	Improvement T_A (K)	%
1.	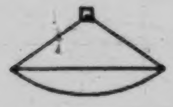	26.3 ± 0.3	/	0.0
2.	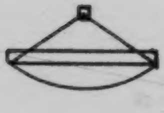	18.0 ± 0.6	8.3 ± 0.7	31.6
3.	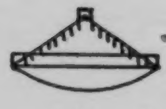	16.9 ± 1.2	9.4 ± 1.2	35.7
4.	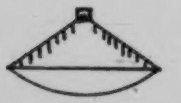	21.2 ± 1.3	5.1 ± 1.3	19.4

Note: 1: Bare antenna (no modifications).
2: Fence added to antenna.
3: Fence and feedleg modifications added to antenna.
4: Feedleg modifications only added to antenna.

table, it can be seen that the most effective individual modification is the fence. The feedleg modifications have a smaller benefit, giving ~ 61 % of the reduction that the fence does. Only a marginal improvement results from having both modifications added to the antenna at the same time.

The improvements in antenna temperature that have been achieved can now be looked at in relation to the interferometer pair, which is the basis of the synthesis telescope. The system temperature of each of the two halves of the interferometer pair is given by equation 1.16 and has a value of about 80 K. If the very small loss that occurs in the waveguide which connects the antenna to the preamplifier is assumed to be zero, then equation 1.16 simplifies to

$$T'_{sys} = T_A + T'_N \qquad 3.17$$

where: T_A = the antenna temperature of an antenna that forms half of the interferometer, and

T'_N = the noise temperature of the preamplifier of the antenna.

Using equations 3.17 and 1.14, the percentage improvement in the minimum detectable correlation temperature can be calculated for an interferometer pair having the various modifications implemented which are listed in table 3.14. They are 10.4 %, 11.8 % and 6.4 % for antenna configurations 2,3,and 4 respectively.

3.5.3 RECOMMENDATIONS

From the measurements listed in table 3.14, two options for improving antenna temperature present themselves. Either the fence or the feedleg modifications could be added to the antenna. Since there is only a slight improvement in the antenna temperature (1.1 ± 1.3 K) when the feedleg modifications are added to the antenna with the fence in place, it is probably not significant enough to warrant both modifications at the same time. This is especially so given the fact that the improvement is less than the estimated errors (1.3 K) of the measurements.

The fence appears to be the most attractive modification, since it reduces the antenna temperature by 8.3 ± 0.7 K, as opposed to 5.1 ± 1.3 K gained with the feedleg modifications. However, the telescope operates at both 1420 MHz, the frequency at which all the measurements and experiments were performed, and at 408 MHz. Since the height of the fence is greater than the wavelength at 408 MHz, it will have a significant effect at that frequency as well. Preliminary measurements of the power pattern of one of the antennas at 408 MHz indicate the presence of high sidelobe levels in the front half of the pattern. With the fence added to enhance the performance at 1420 MHz, some of the energy that would have been spillover at 408 MHz would be redirected into the front area of the antenna pattern, further raising the sidelobe levels. This could cause a degradation of the performance of the telescope at 408 MHz, since presently, without any modifications, interference from strong sources that are outside the 408 MHz field has been a problem. An MSc. project currently underway is investigating the performance of the DRAO antennas at 408 MHz. The results of this project should enable the effect of the fence at 408 MHz to be determined, and therefore help decide if the modification should be implemented.

However, the feedleg modifications have dimensions significantly smaller than the wavelength at 408 MHz (0.735 m), and therefore they should have little effect at that frequency. Because of this, and the unknown effect that the fence would have at 408 MHz, modifying the feedlegs seems to be the best choice to implement to reduce the antenna temperature at this time. It is an easy modification to the existing feedlegs of the antennas now in use, and should be easy to implement on the new antennas being added to the array. As well, the modified feedlegs would have little effect on the mechanical performance of the antennas. The fence could present a problem by catching large amounts of snow in a heavy, wet snowfall, which would result in weight being temporarily added to the antennas.

The half-vertex angle δ of the triangular cross-section of the feedleg modification should be kept small. The value of 15° chosen for the experiments on the fifth antenna worked well, although the power levels in the scattered sidelobes increase as the half-vertex angle is decreased. From the measurements it would appear that most of the feedleg lobes were redirected away from the ground. As well, by using 15° the centers of the scatter lobes are placed close to the main beam ($\rho = 25.2^{\circ}$), which allows the antennas to assume large zenith angles ($\sim 60^{\circ}$) before the centers of the lobes begin to intersect the ground. This has the effect of helping to keep the antenna temperature constant throughout an observation run, as the telescope tracks from east to west.

The half-vertex angle of 15° as opposed to a larger angle has the effect of increasing the height of the triangular modification placed on a circular feedleg of a given diameter. It is advantageous to do this since the effectiveness of the modification depends on the dimension being greater than the wavelength of observation. In the case of the far east and far west antennas which have a quadrupod arrangement of smaller diameter feedlegs (table 1.1), a 15° half-vertex angle would give a height of only ~ 1/2 wavelength for the roof at 1420 MHz. For these antennas, a smaller half-vertex angle for the modifications could be used with the existing feedlegs to lengthen the height of the triangular sections.

The calculations from section 3.4 predict that changing the feed support system from a quadrupod to a tripod arrangement would reduce the antenna temperature somewhat. However, if the triangular shaped feedlegs have been implemented such a change should have a minimal effect on antenna temperature, since the feedleg lobes would all be directed away from the ground into the region close to the main beam.

Finally, the information contained in figure 3.14 indicates that after spillover and feedleg scatter, leakage contributes a significant portion of the total antenna temperature. An effort could be made to reduce this source in the future, possibly by lining the existing surface of the antennas with a metal foil. Such a modification should lower the antenna temperature by about 5 or 6 K.

CHAPTER 4

INTRODUCTION TO SHARPLESS 183

The second topic of this thesis is an investigation of the nature of the galactic nebula, Sharpless 183 (S183), based on observations with the DRAO synthesis telescope. It is a 60' X 40' region of radio emission at RA = $00^h\ 51.5^m$, Dec = 65.5^o. A number of observations have been made of this object in the past which have resulted in it being classified both as an HII region and a supernova remnant (SNR).

An HII region is an area of space where the interstellar medium has become ionized due to the absorption of ultraviolet radiation from one or more nearby young O and B type stars. The areas have sizes that can range up to several parsecs across, and shapes which vary from circular to irregular depending on the distribution of the material in and around the cloud. The thermal radiation given off by an HII region is the result of the ions and electrons colliding within the cloud.

A supernova remnant is a blast wave propagating through the interstellar medium following the explosion of a star. The radiation is non-thermal, and results from electrons, which have been accelerated by the supernova or by the supernova remnant blastwave, interacting with magnetic fields.

Supernova remnants and HII regions can be distinguished from each other by using a number of their observable differences. Two of the main differences are: 1) radiation brightness from a SNR decreases with increasing radio frequency while it remains flat or increases for an HII region, and 2) a SNR does not show recombination line emission, whereas the opposite is true in an HII region.

4.1 PREVIOUS OBSERVATIONS OF S183

The above differences have been used to try to classify S183, but uncertainty remains mainly due to the low resolution of the previous observations. Details of these surveys are given below.

Sharpless classified the object as an HII region on the basis of its appearance on the Palomar prints, and included it in his catalog "A Catalog of HII Regions"[30].

S183 also appears in the Effelsberg 21 cm Galactic Plane Survey[31], a section of which appears in figure 4.1. S183 appears in the upper right hand corner at $l = 123.2^{\circ}$ and $b = +2.9^{\circ}$.

In 1968 Galt and Kennedy[32] observed this source with the DRAO 26 m telescope at 1400 MHz with HPBW = 36', and

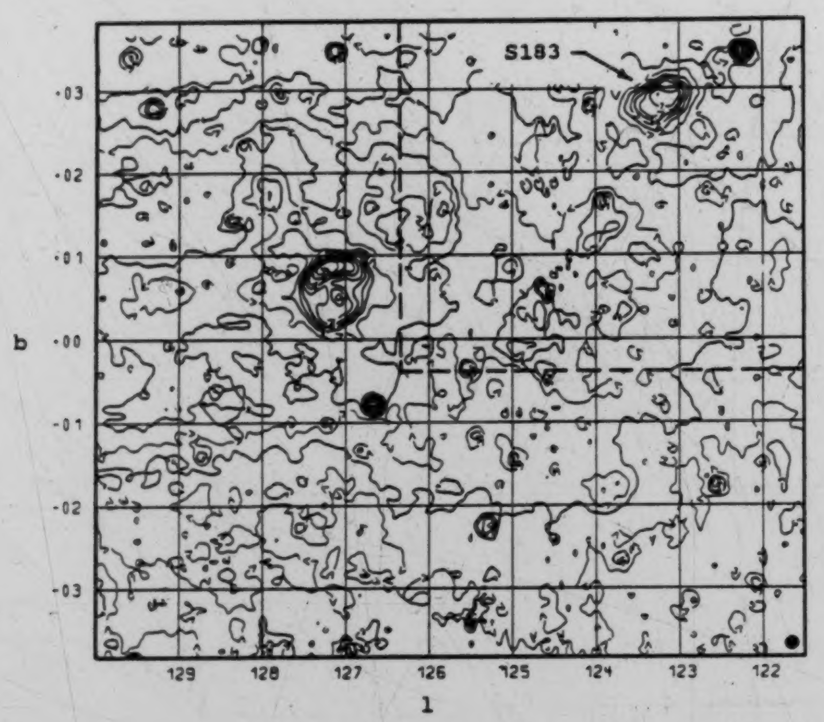

Figure 4.1
A 1420 MHz Map which Includes S183

A section of the Effelsberg 21 cm Galactic Plane Survey containing S183 (Adapted from Kallas and Reich[31]). Two boundaries of the 408 MHz DRAO field are shown by dotted lines.

found its flux density to be 4.8 ± 1 Jy. It appears as source No. 24 in the DA catalog.

The object was mapped in 1972 at 1400 MHz by Felli and Churchwell[33] with HPBW = 10' (shown in figure 4.2). In their map the emission from S183 appears to be centrally peaked with no obvious edge brightening. The flux density for S183 from this observation is 7.1 ± 2.5 Jy.

Churchwell and Walmsley[34] observed S183 at 2695 MHz with 18' resolution in 1973, but were unable to state whether it had a thermal or nonthermal spectrum. Assuming that S183 was an HII region, they searched for an exciting O or B star, but found none. Their 2695 MHz flux density is 5.0 ± 1.5 Jy.

In 1979 Bonsignori-Facondi and Tomasi[35] mapped S183 at 408 MHz with the EW (east-west) arm of the Bologna Cross. Drift scans through the source were made at 0.5° intervals in declination with a beam shape of 4.2' EW X 110' NS. Figure 4.3 shows their map of S183, with the shaded portion indicating the scan through the source. They found a "shell-like structure" and a flux density of 11.5 ± 1.7 Jy. From this measurement and those of Felli and Churchwell (1972) and Churchwell and Walmsley (1973), a spectral index of $\alpha = 0.48$ was obtained (see section 6.1.1 for the definition of spectral index). From its "shell-

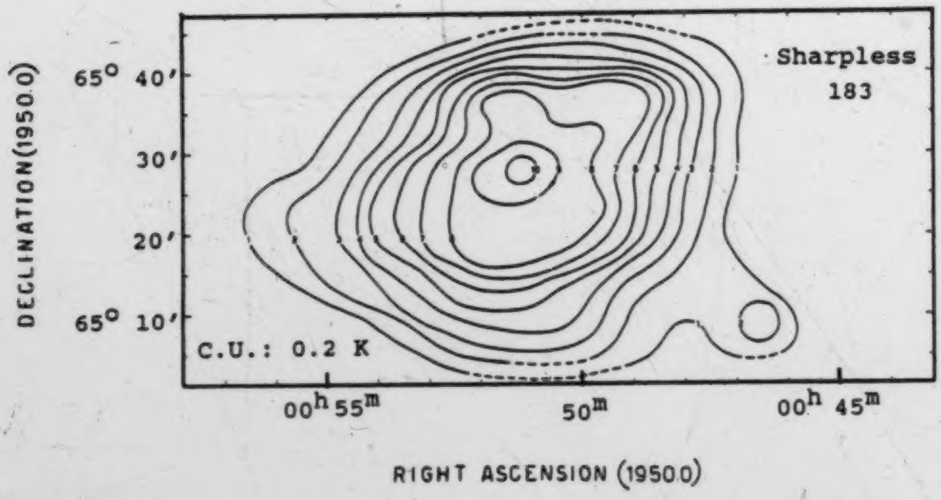

Figure 4.2
A 1400 MHz Map of S183

A 1400 MHz map of S183 with angular resolution of 10′ (Adapted from Felli and Churchwell[33]).

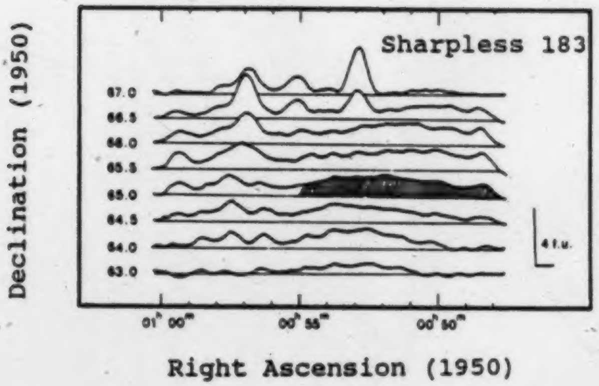

Figure 4.3
Map of Fan Beam Scans in the Region of S183

408 MHz fan beam scans at constant declination from the BGE 0051 + 65 map of S183 (Adapted from Bonsignori-Facondi, and Tomasi[35]). The resolution is 4.2′ EW X 110′ NS.

like structure" and steep spectral index Bonsignori-Facondi and Tomasi considered S183 to be a supernova remnant. Using the surface brightness - diameter (Σ - D) relation from Clark and Caswell[36], they estimated the distance of S183 to be about 3.6 kpc.

The Σ - D relation is a method of obtaining the distance to a supernova remnant. The relation (surface brightness as a function of diameter) has been obtained statistically from a number of remnants whose distances, and hence diameters are independently known. The relation is used to find the physical diameter of an SNR using the measured surface brightness obtained from a radio map of the object. Then, with the diameter and the measured apparent size, the distance to the object is calculated.

More recently in 1984, Fich and Blitz[37] have detected CO emission from the direction of S183. This observation is an indication that S183 may not be a supernova remnant, despite its steep spectral index, but may instead be an HII region. This is because HII regions are ionized regions around young stars, and new stars form in dense regions. CO is a tracer or indicator of high density. However, O and B stars are short-lived, due to their high mass, and eventually become supernovas. The CO velocity was found to be -10.3 km s^{-1}, giving a kinematic distance of 0.74 ± 0.51

kpc to S183. This distance is based on a rotation curve of the Galaxy, and the assumption that all objects are undergoing only circular motion in the Galaxy.

The uncertainty concerning S183 at the start of this investigation was the main motive for obtaining better data. Therefore, a survey using the DRAO synthesis telescope was undertaken in February and March of 1987. The resolution of the synthesis telescope at both 408 MHz and 1420 MHz is better than any of the previous maps of this object, and has enabled a reliable classification of S183 as an HII region as opposed to a supernova remnant. As well, modeling has resulted in estimates of some of the physical parameters of S183.

CHAPTER 5

THE S183 SURVEY

5.1 OBSERVATIONS AND DATA REDUCTION

S183 was observed with the synthesis telescope at DRAO during February and March of 1987. The observations took about 33 days to complete using 66 different locations for the two movable antennas of the array. Details of the survey are listed in table 5.1 along with some of the parameters of the telescope.

5.1.1 PRELIMINARY DATA REDUCTION

Before an observer arrives at the observatory, the staff have performed the initial steps of data reduction to produce preliminary maps. First, the visibility records which result from the correlation of pairs of antennas of the telescope are calibrated and edited. Any sections that have obvious interference from satellites or radio noise produced by other sources on the ground are removed.

Next, the visibility records which lie along elliptical tracks in the uv-plane are gridded onto an array suitable for the Fast Fourier Transform (FFT) algorithm. A convolution is performed to fill in the visibility function

TABLE 5.1
TELESCOPE PARAMETERS AND SURVEY DETAILS FOR S183

	408 MHz	1420 MHz
Field Center	RA = $0^h\ 51^m\ 30.0^s$	DEC = $65^\circ\ 30'\ 0.0''$
Date of Survey	February - March 1987	
Calibrators	3C 147 (48.0 Jy) 3C 295 (54.0 Jy)	3C 147 (21.29 Jy) 3C 309.1 (7.73 Jy)
uv Plane Coverage (0 - 604 m)	0 - 820 λ	0 - 2860 λ
Field of View	7.4° to 26% point	2.1° to 34% point
Angular Resolution	3.5' X 3.8' (EW X NS)	1.0' X 1.1' (EW X NS)
Sensitivity (rms) (per beam)	3 mJy	0.8 mJy
Polarization	Right Circular	Left Circular
Short Spacings	Haslam et al.[38] (Jodrell Bank) (0 - 30 λ)	Kallas & Reich[39] (Effelsberg) (0 - 152 λ)

at the defined grid points in the uv-plane.

The preliminary maps have dimensions of 1024 X 1024 pixels and are produced by using the inverse FFT on the array of gridded visibilities. Figure 5.1 shows the 1024 X 1024 preliminary map of the S183 field at 408 MHz. Each pixel in the map represents 105" making the map about 30° on each side. It is at this point that the observer arrives at the observatory to continue the data reduction process.

5.1.2 CLEANING THE MAPS

The preliminary maps produced by a synthesis telescope have several defects that are not inherent to the map. The most obvious features in figure 5.1 are the large elliptical ring-like structures which are centered on the strong point sources in the field. They are called grating rings, and are a result of the way in which the data are obtained. The DRAO antennas are repositioned on a daily basis to create new baselines for correlation, with a regular spacing interval D of 4.286 meters. The spacing interval results in large grating ring responses at angles of $n \lambda /D$ from the beam center, where n is an integer and λ is the wavelength of observation. At 408 MHz the first grating ring is at a radius of 9.83° from the

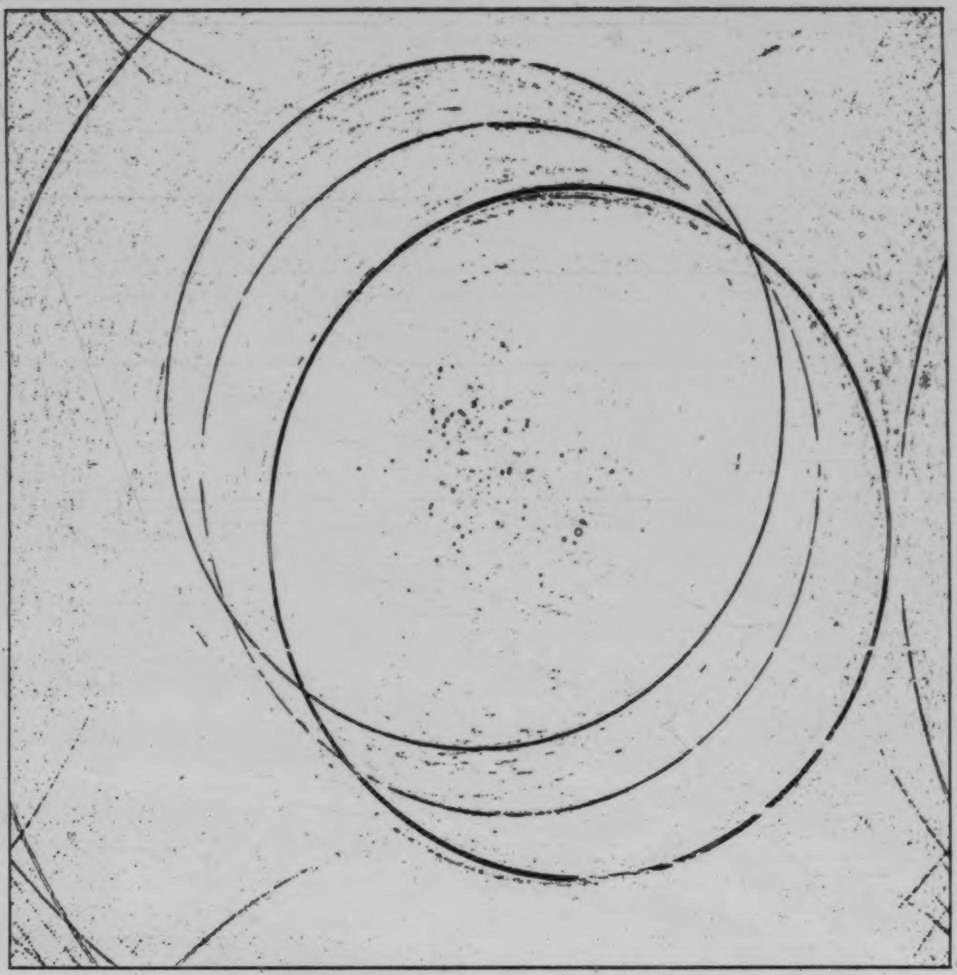

Figure 5.1
The Preliminary 1024 X 1024 408 MHz Map

Contours are shown from -40.0 to 520.0 mJy/ba in steps of 140.0 mJy/ba. Each pixel represents 105" making the map 29.9^{0} square. The field center is at RA = 0^{h} 51^{m} 30.0^{s}, DEC = 65^{o} 30' 0.0". North is at the top of the map.

synthesized main beam, and in the 1420 MHz case it lies at a radius of 2.82°. The spacing interval has been selected to place the first grating ring well away from the area of interest at the center of the field.

Figure 5.1 also shows the effects of aliasing from the replicated images that are adjacent to this map. This is caused by the gridding or sampling of the data in the uv plane at the regular intervals required for the FFT algorithm. The choice of the gridding interval has kept the aliased features away from the central portion of the 1024 X 1024 map.

Figures 5.2 and 5.3 show the central 512 X 512 region of the 408 MHz and 1420 MHz preliminary maps respectively. In these maps, along with the grating ring responses, there are numerous smaller diameter ring-like features surrounding the stronger point sources. These are caused by the sidelobe structure of the synthesized beam and are superimposed on the weak underlying features in the field. In addition to the ring-like features, there are several prominent linear defects attached to the stronger point sources in the field. They are oriented in a N-S direction and result from a 5° strip of data missing at 12 hours. S183 was observed through lower culmination and the limit switches prevented a small segment of the sky from being observed.

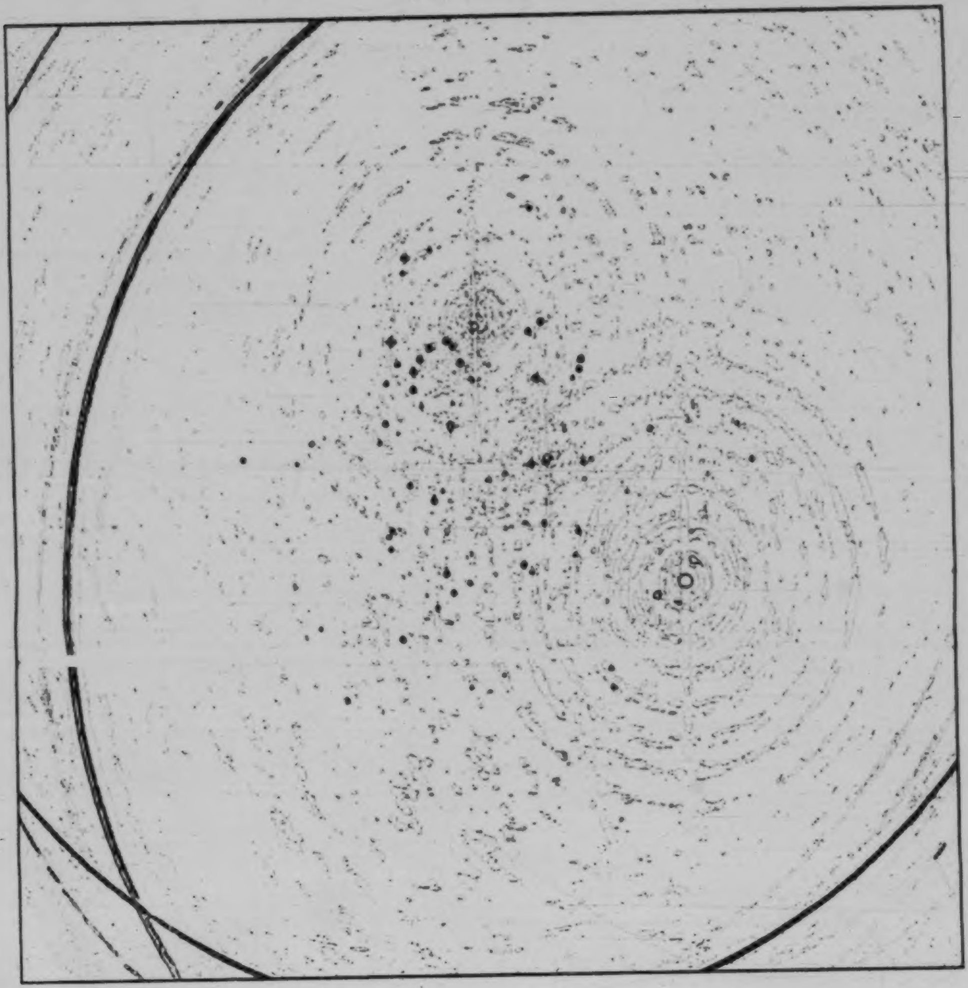

Figure 5.2
The Preliminary 512 X 512 408 MHz Map

The central 512 X 512 area of the 408 MHz preliminary map. Contours are shown from -40.0 to 660.0 mJy/ba in intervals of 140 mJy/ba. Each pixel represents 105" making the map 14.9^{0} square. The field center is at RA = 0^{h} 51^{m} 30.0^{s}, DEC = 65^{0} 30' 0.0". North is at the top of the map.

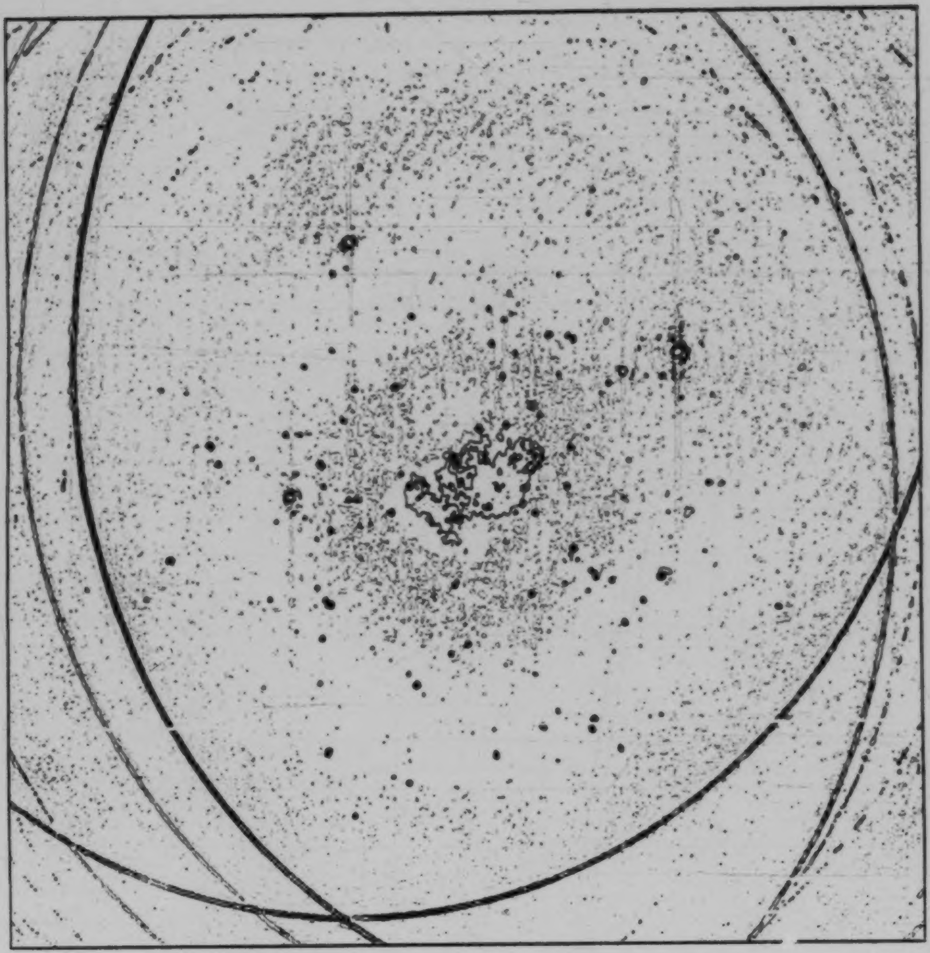

Figure 5.3
The Preliminary 512 X 512 1420 MHz Map

The central 512 X 512 section is shown with contours from -4.0 to 23.0 mJy/ba in steps of 3.0 mJy/ba. Each pixel represents 30" making the map 4.3° square. The field center is at RA = 0^h 51^m 30.0^s, DEC = 65° 30′ 0.0".

If the point sources are strong, the sidelobe features often will distort the map to the point where the real features are hard to identify. In the case of the 408 MHz map shown in figure 5.2, this is somewhat the case. For this reason the preliminary map is often referred to as the "dirty map".

Iterative procedures (first developed by Hogbom[40]) have been implemented to remove distortions due to sidelobe responses and are generally referred to as "cleaning" a map. A version of the CLEAN algorithm which was developed by Steer et al.[41] is used at DRAO.

Briefly, a map is cleaned in the following manner. First, the maximum brightness of the map is found. Usually this will be a point source with the unwanted sidelobe structure surrounding it. The synthesized "dirty beam" is normalized to the maximum value of the source and superimposed on it. The dirty beam is the Fourier transform of the aperture plane sampling function (= 1 where an observation has been made and equals 0 where an observation is missing). Some fraction of the dirty beam, usually 1/2, is then subtracted from the map. The procedure is repeated until that point source becomes lower than the next brightest source in the field. The operation is then applied to that source, and subsequent sources until one of the following conditions is met: 1) the value of the maximum intensity of the map is reduced below a specific value, 2) the number of iterations performed exceeds a set limit, or 3) the value of maximum brightness in the map stops decreasing.

At this point, the dirty map has been decomposed into a sum of beam functions whose locations and amplitudes are stored in a computer file. The clean map is then created by adding together a sum of clean beams whose amplitudes and positions have been specified in the file. The clean beam has no side lobes and is usually a Gaussian equal in size to the main lobe of the dirty beam. The residuals left over after the decomposition are added back. If the conditions used to terminate the process are well chosen, the sidelobe features will have been reduced to values comparable to the noise on the map. Full details of the DRAO procedure to clean a map may be obtained by referring to CLEAN in the DRAO help file documentation.

During the cleaning process, beam functions are subtracted from the inner 512 X 512 region only. If a strong source falls outside the central 512 X 512 section but inside the 1024 X 1024 region, its sidelobes are not removed by cleaning. The reason for this is illustrated by figure 5.4. If a strong source is located at A, the corner

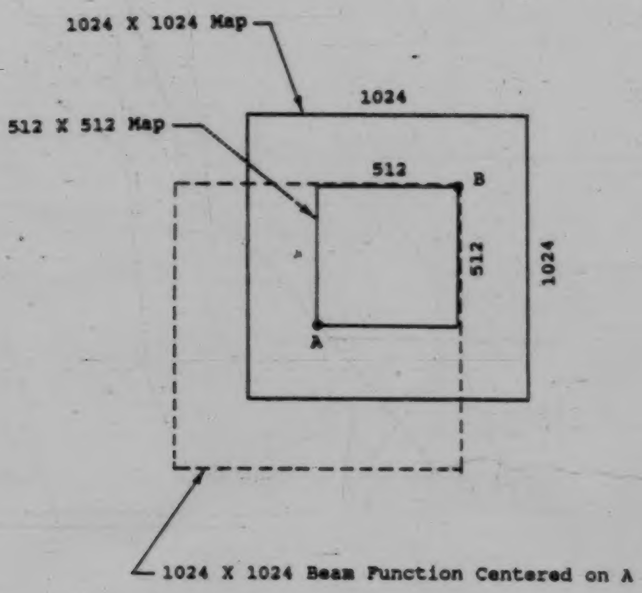

Figure 5.4
The Beam Function Superimposed on the Map for Cleaning

The 1024 X 1024 beam function superimposed on point A in the 1024 X 1024 map, demonstrating that only the inner 512 X 512 area can be cleaned.

of the 512 X 512 box, the beam function extends only as far as B. Therefore, with a 1024 X 1024 beam, only the central 512 X 512 section can be cleaned.

Figures 5.5 and 5.6 show the cleaned 408 MHz and 1420 MHz map respectively. The improvement over the dirty maps is evident by comparing them with the maps shown in figures 5.2 and 5.3. However, several defects are still visible in these maps.

In the 408 MHz map (figure 5.5) the narrow curved features are grating rings which belong to point sources located outside the inner 512 X 512 region, and as a result they are not cleaned off. As well, there are several broader curved features of low intensity that have the north celestial pole as their center. These are caused by 408 MHz interference which was not removed from the visibility data in the editing process. There is still some sidelobe structure surrounding the bright point sources but its level is comparable to the noise on the map. Finally, several thin horizontal areas are visible in the map which do not contain contour information. These features have been caused by the electrostatic printing process which was used to make the map.

The 1420 MHz map (figure 5.6) is free of any interference bands and grating rings, but still some weak

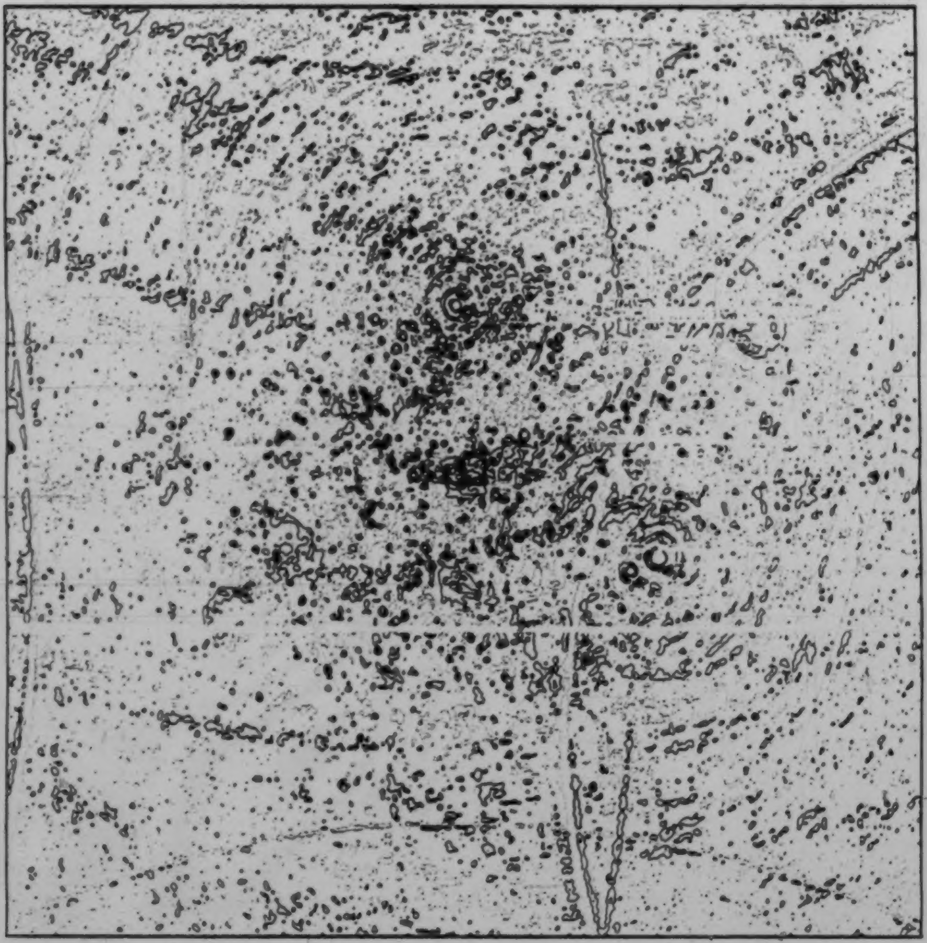

Figure 5.5
The Clean 408 MHz Map

The central 512 X 512 section is shown with contours from -10.0 to 170.0 mJy/ba in steps of 20.0 mJy/ba. Each pixel represents 105" making the map 14.9° square. The field center is at RA = $0^{h}\ 51^{m}\ 30.0^{s}$, DEC = $65^{\circ}\ 30'\ 0.0''$.

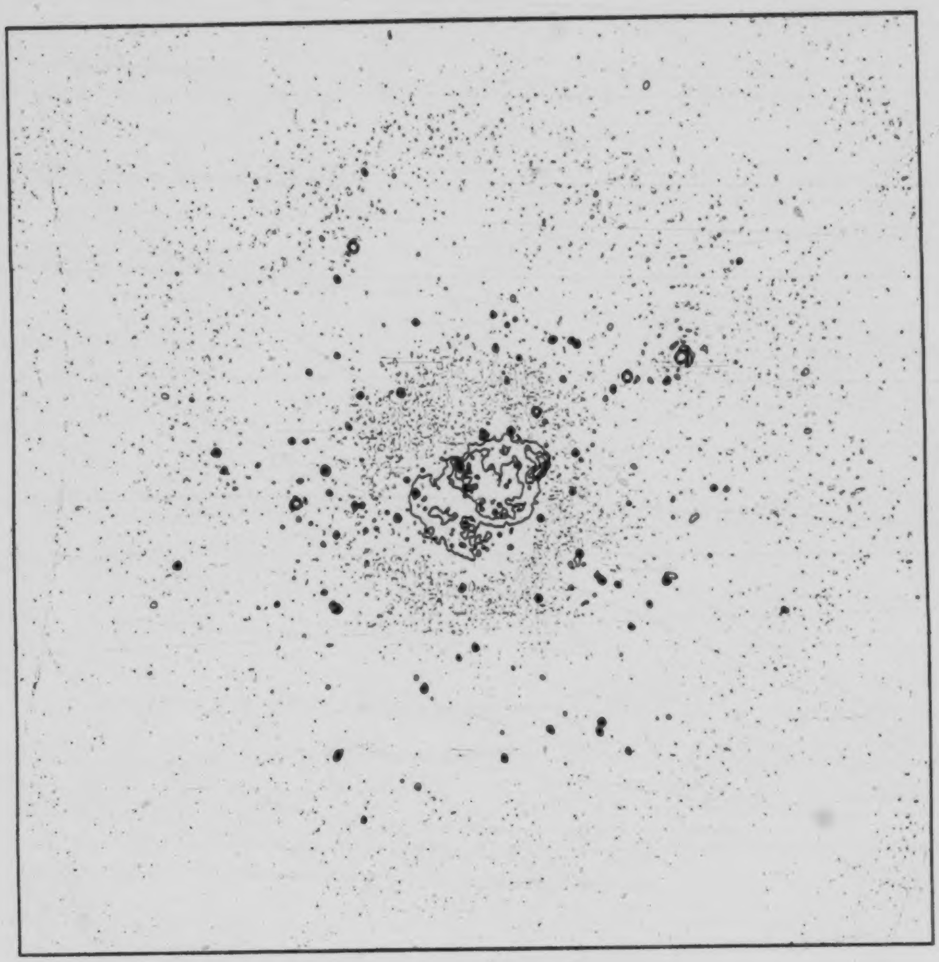

Figure 5.6
The Clean 1420 MHz Map

The central 512 X 512 section is shown with contours from -4.0 to 23.0 mJy/ba in steps of 3.0 mJy/ba. Each pixel represents 30" making the map 4.3° square. The field center is at RA = $0^h\ 51^m\ 30.0^s$, DEC = 65° 30′ 0.0".

sidelobe structure surrounds the strong point sources, and is probably due to instrumental phase and amplitude errors. In addition, some faint ringing is evident resulting from the primary response pattern of the antennas which are used to make up the array.

The above features should not influence the interpretation of the data, since they: 1) are fairly faint, 2) have not been superimposed on S183, or 3) will be removed when the background is subtracted prior to the determination of the flux densities.

5.1.3 ADDING THE LOW ORDER SPACINGS

After cleaning, the next step in producing final maps is to add in the low order spacings. The response from an interferometer pair is a set of fringes that are superimposed on the sky (figure 1.4) with a period of 1/b radians, where b is the projected length of the baseline in wavelengths. The fringe pattern measures the Fourier component of the sky brightness distribution for that particular orientation of the baseline. Measurement of the broad or d.c. component with an interferometer would require shorter spacings between the antennas than are physically possible. This makes it impossible to measure components of sky brightness whose angular frequencies are lower than some value set by the minimum spacing D of the interferometer pair. The spacings in this category are called the low order spacings. Since spacings from 0 to D meters are sampled with an antenna of D meters in diameter, the missing spacings can be obtained from observations made with an antenna whose diameter is greater than or equal to this value.

The low order spacings for the 408 MHz map were taken from a survey done by Haslam et al.[38] in 1982. The 1420 MHz low order spacings were obtained from the Effelsberg 21 cm Galactic Plane Survey by Kallas and Reich[39]. Both surveys are available in digitized form on disk at DRAO.

The process of adding the low order spacings to the interferometer data requires several steps. For the 408 MHz case a low order map of the field was extracted from the digitized Haslam data using SURVEY, an interpolation and gridding program. This map was then corrected for the primary beam of the telescope which was used to acquire the data. The correction is necessary because the low order data is the sky filtered through the transfer function shown in figure 5.7a (the higher spatial frequencies have been attenuated). The correction to obtain the flat transfer function shown in figure 5.7b is accomplished by dividing the low order data in the uv plane by the Fourier transform of a Gaussian of the same size as the beam of the

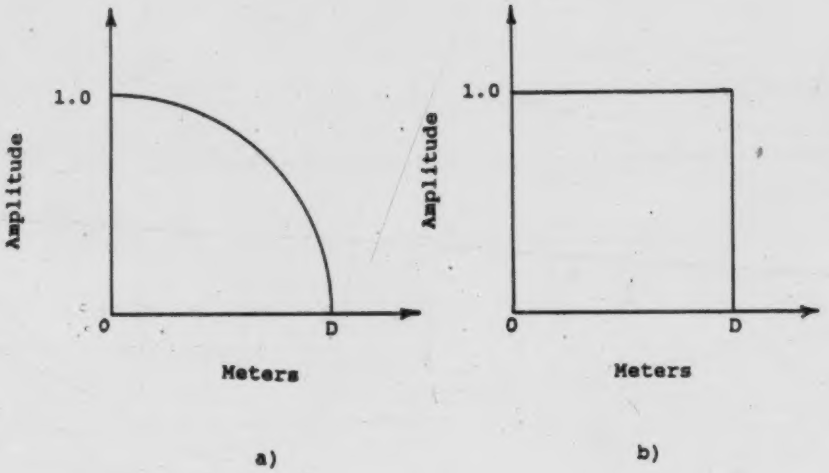

Figure 5.7
Telescope Transfer Functions

a) The uncorrected transfer function of an antenna D meters in diameter, which attenuates the higher spatial frequencies,
b) The corrected transfer function.

primary element of the telescope (HPBW = 51' in the case of the Haslam survey). The visibilities in the uv plane were then transformed back to obtain the corrected low order map. Figure 5.8 shows the 408 MHz low order map.

The high order map requires the same correction since it has been multiplied by the transfer function of the primary element in the interferometer. The transfer function is a gaussian with the value 1.0 at the center and having low values near the edge of the map. Its effect can be seen in figures 5.5 and 5.6. Numerous point sources and fine detail are visible near the center of the map. However toward the edges the number of point sources drops to zero and the detail is lost in the noise.

The correction was made by dividing the map data by the primary pattern of the interferometer element. This operation increases the noise away from the map center since one is dividing by a function which drops to a small value at the edges of the field. Therefore, outside a certain radius, where the noise begins to dominate the map, the pixels have been set to zero. The 408 MHz map has been zeroed beyond a radius = 380'. For comparison, the FWHM of the 408 MHz polar diagram is 318'.

At this point, the uv data for both the low and high order maps require a filtering operation which regulates

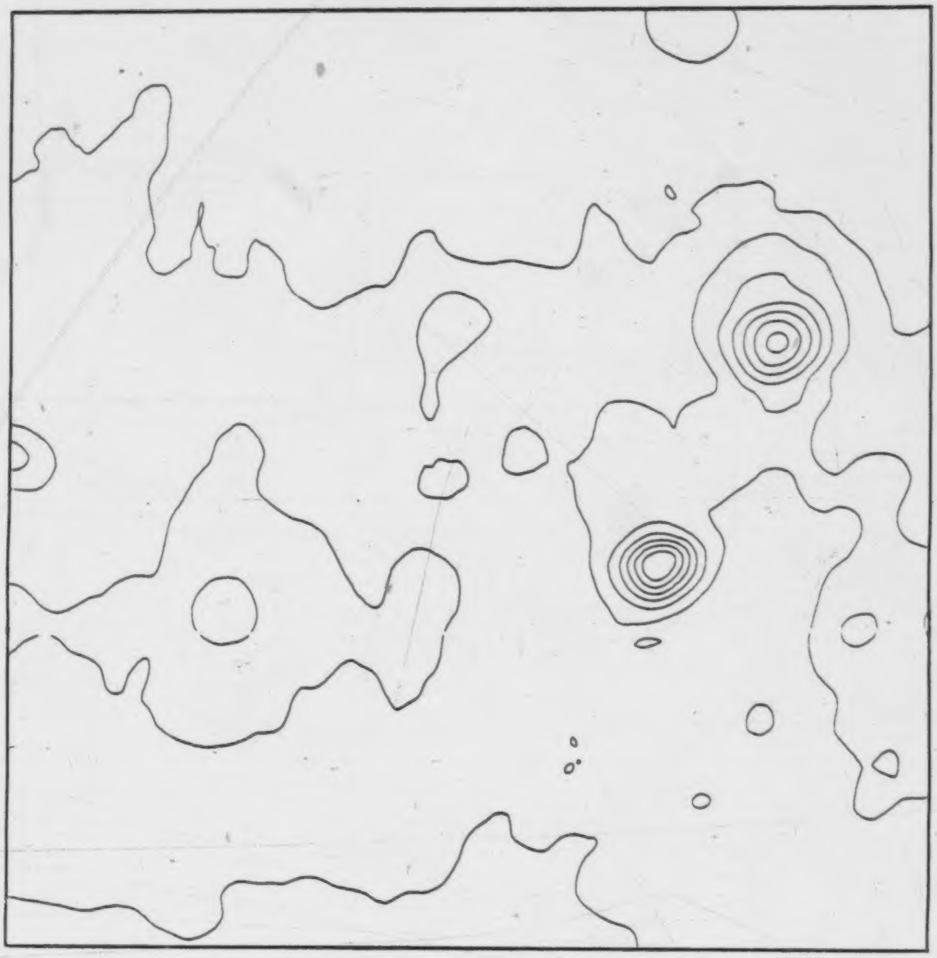

Figure 5.8
The Low Order 408 MHz Map

The low order 512 X 512 408 MHz map extracted from the survey published by Haslam et al.[30]. Contours are shown from 30.0 to 120.0 K (Tb) in steps of 10.0 K (Tb). The resolution is 51.0′. Each pixel represents 105″ making the map 14.9° square. The field center is at RA = 0^{h} 51^{m} 30.0^{s}, DEC = 65° 30′ 0.0″.

the amount of overlap in the uv data for the combined map. The visibilities of the low order map are clustered around the center of the plane and fall to zero at a radius of D meters. The high order visibilities fill the plane out to the maximum size of the array, but avoid the central region. As mentioned above, the central hole is caused by not being able to correlate antenna pairs at spacings less than an antenna diameter. At DRAO this happens at about 9 m. The low order spacings are used to supply the missing visibilities in the center of the high order map.

Since the ranges of the low and high order visibilities overlap in the uv-plane, careful filtering must be done on both sets of visibilities, so that when they are transformed back to the map plane and added, an accurate map will be produced. The radius at which the low and high order information are added with equal weight must be decided on, as well as the range over which they will be blended. Figure 5.9 shows the type of filtering applied to the low and high order visibility data. In the case of the 408 MHz data, A, B, and C of figure 5.9 were chosen to be 12.9, 22.2, and 31.5 m respectively in the uv-plane. B = 22.2 m was chosen because an antenna with a resolution equal to 51′ (the resolution of the Haslam survey) has a response that drops to 50% at 22.2 m in the uv-plane. The blending range was chosen to ensure a smooth transition

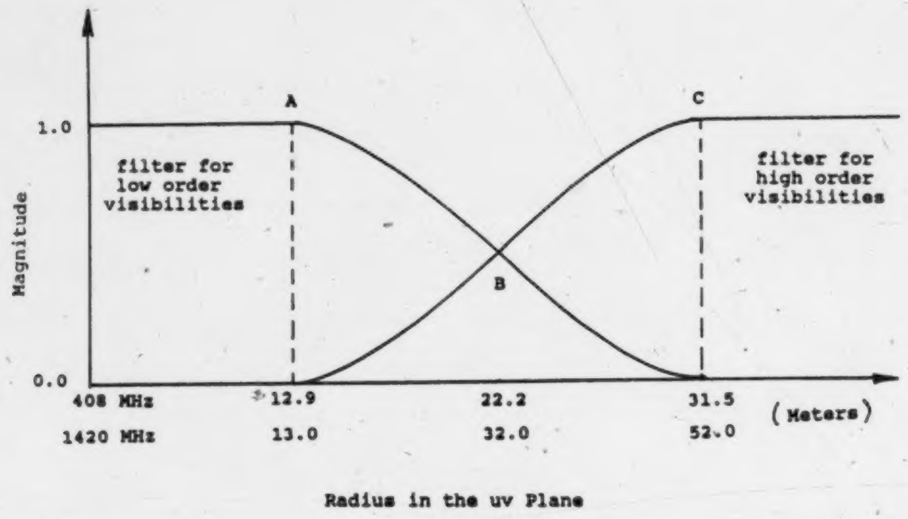

Figure 5.9
The Filters Applied to the uv Visibility Data

The uv-plane filtering of the visibility data.

A - Point at which the low order data are given a weight of 1.0, and the high order data given weight 0.0.

B - Point at which the low and high order data are given equal weight.

C - Point at which the high order data are given a weight of 1.0, and the low order data given weight 0.0.

from one data set to the other.

Applying the filter (figure 5.9) to the high order data attenuates the lower spatial frequencies, whereas the filter that is applied to the low order data has the opposite effect, and is equivalent to smoothing the map. Figure 5.10 shows the result of filtering the higher spatial frequencies out of the low order map which is shown in figure 5.8. After filtering, both the low and high order visibilities were transformed back to the map plane. The FFT program used to do the transformation back and forth between the map and uv planes is called MAP2UV.

Before being added together, the low and high order maps must be converted to the same units. The low order map was converted from mK to K (Tb). The high order map was converted from mJy/ba to K (Tb) by multiplying it by the conversion factor F, given by the expression below[42].

$$F = 0.385(E)/(1.13\ F^2\ R^2) \qquad 5.1$$

where: E = the minor/major axis ratio for the resolution,

F = the frequency of observation in GHz, and

R = the minor axis of the resolution in arcmin.

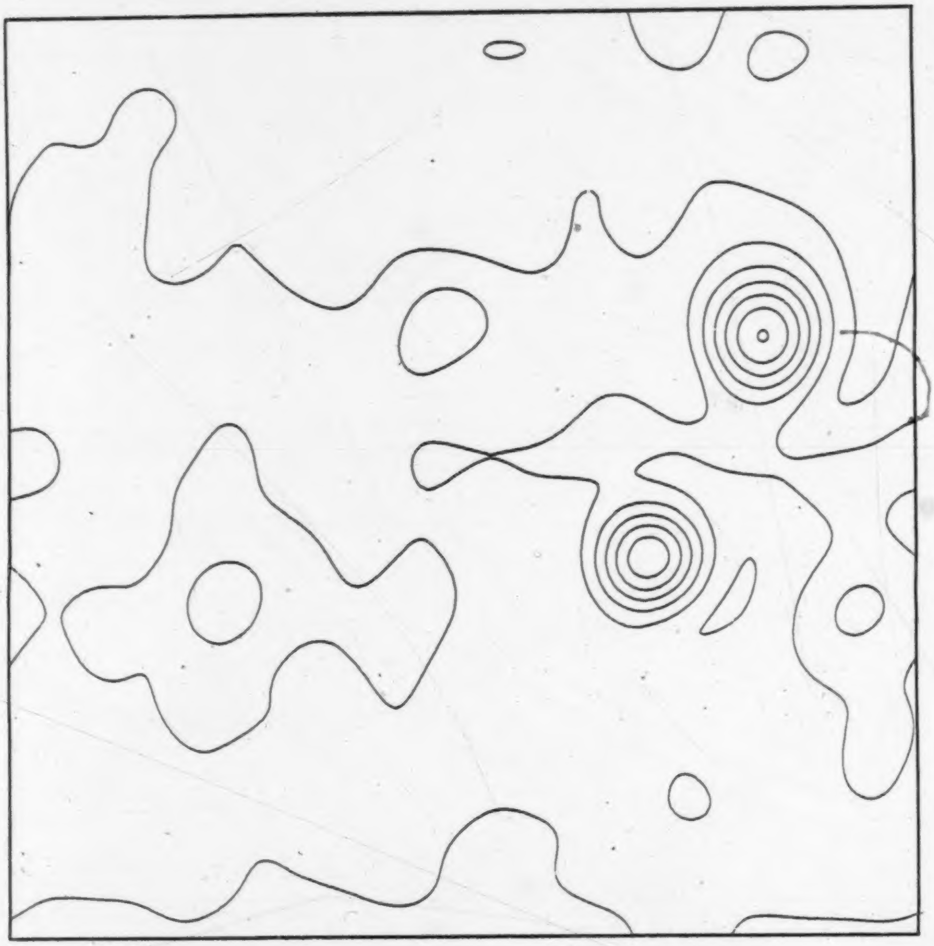

Figure 5.10
The Filtered 408 MHz Low Order Map

Contours are shown from 30.0 to 120.0 K (Tb) in steps of 10.0 K (Tb). Each pixel represents 105" making the map 14.9^0 square. The field center is at RA = 0^h 51^m 30.0^s, DEC = 65^0 30′ 0.0".

In the case of the 408 MHz map, one final correction must be applied to produce an accurate map. It is the AGC (Automatic Gain Control) correction. The 408 MHz system has an AGC to keep the receiver output power constant. The effect of this is to keep the sum of the antenna temperature and the system temperature multiplied by a gain factor constant. When the visibility data are being gathered, the antennas are periodically pointed toward point sources for calibration. There will usually be a difference in flux density between the field being observed and the one which contains the calibration source. This results in a different antenna temperature for the two fields, which will cause the gain to be changed to keep the power output the same. Therefore, a correction to account for the change in gain must be applied to the survey data. Full details of this calculation are given by Landecker[43].

The main step in the determination of the correction factor involves a calculation of the antenna temperature for both fields. The antenna temperature is obtained numerically by superimposing a Gaussian beam, matching the beam of the primary element of the synthesis telescope at 408 MHz (HPBW = 318'), on the Haslam survey data at each location. After obtaining the two antenna temperatures the correction factor can be calculated. For the field containing S183 the AGC correction works out to be 1.159.

The correction was applied to the high order map and then the low and high order maps were added together using the Manipulator feature of MADR, a program which facilitates the modification of data sets. This produced the complete 408 MHz map shown in figure 5.11. S183 can be seen at the center of the field. The zeroing of the high order map at a radius of 318' is evident. The area outside the radius of 318' contains only the brightness values of the low order map. The central portion of figure 5.11 was then extracted to form figure 5.12, a more detailed view of S183 and its surroundings. The 408 MHz map is now complete.

The 1420 MHz data were handled in a similar way. The low order spacings were obtained from the Effelsberg 21 cm Galactic Plane Survey by Kallas and Reich[39]. The survey has an upper limit of $b = +3.75^{o}$. The northern boundary of the 1420 MHz field extends beyond this value by about a degree, which necessitated the insertion of a 1 K fill value into this area to provide the missing low order values. Figure 5.13 shows the low order map with the 1 K fill values added to the north section of the map. It also shows a cross-section through the center of the map from south to north, which demonstrates that the added 1 K

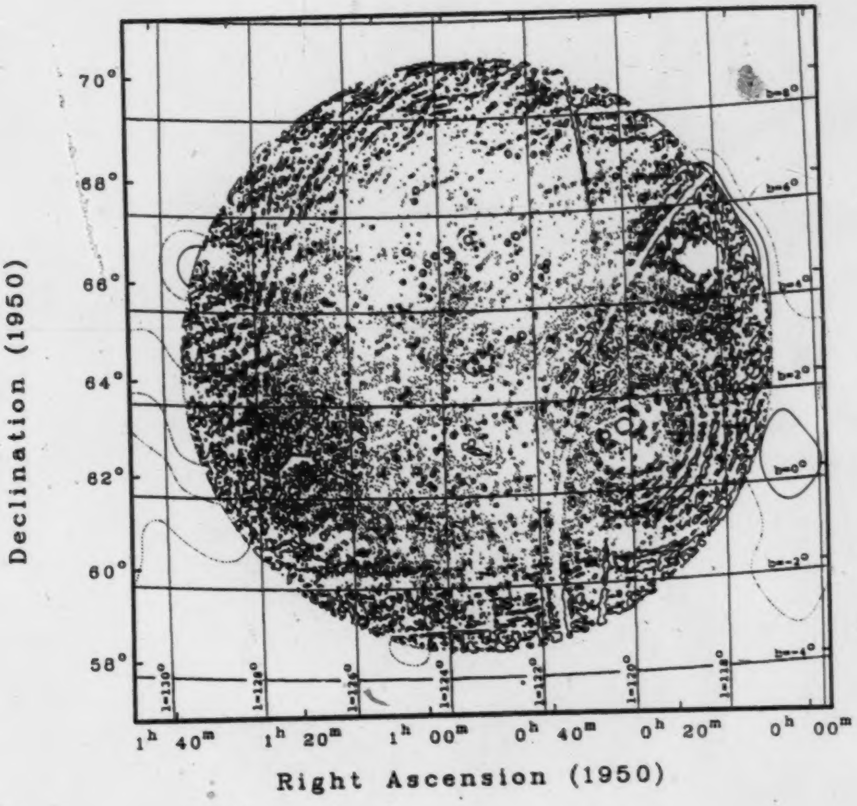

Figure 5.11
The Complete 408 MHz Map

The 512 X 512 408 MHz map showing the sum of the low and high order maps. Galactic and Equatorial coordinate systems are shown. Contours are shown from 58.0 to 82.0 K in steps of 8.0 K. The AGC correction has been added. Pixel size is 105".

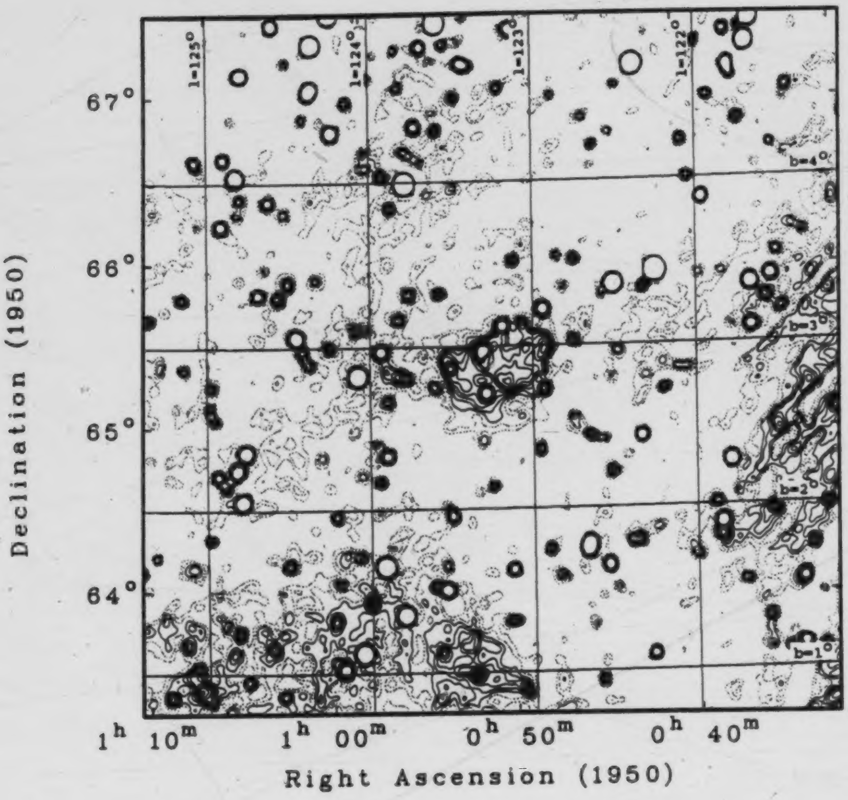

Figure 5.12
The final 408 MHz Map

The central area of the 408 MHz map. The map is 512 X 512 pixels with each pixel = 30.0". Contours are shown from 58.0 to 78.0 K in steps of 2.0 K.

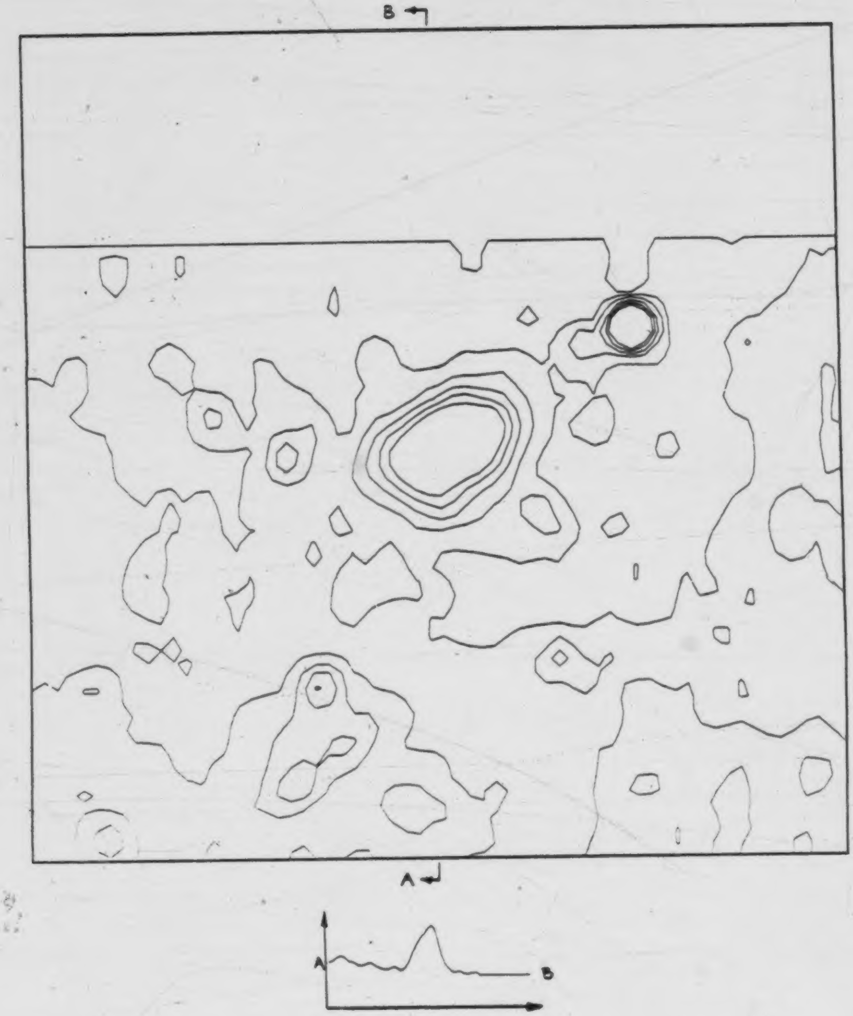

Figure 5.13
The Low Order 1420 MHz Map

The low order 64 X 64 1420 MHz map from the Effelsberg 21 cm survey[39] with the 1.0 K fill values in the upper portion. Contours are shown from 1.0 to 2.0 K in steps of 0.2 K. Each pixel represents 240" making the map 4.3° square. The field center is at RA = 0^h 51^m 30.0^s, DEC = 65° 30' 0.0". North is at the top of the map.

A cross-section is shown from south to north through the map. The fill values show up as the straight line portion of the plot.

values are a reasonable estimate of the background brightness in that direction.

As in the 408 MHz case, the visibilities of the low order map were corrected for the gaussian taper of the beam used in the Effelsberg survey (9'), and the high order map was polar corrected for the primary pattern at 1420 MHz. Both the low and high order maps were then filtered in the uv-plane with the filters shown in figure 5.9, with points A, B, and C of the filter set to 13.0, 32.0, and 52.0 m respectively. Figure 5.14 shows the effect of filtering the low order 1420 MHz map in figure 5.13.

The low and high order maps were converted to K (T_b) and added together using MADR, giving the map shown in figure 5.15. In the map, zeroing was applied to the high order data beyond a radius = 90'. Outside this radius the low order map values can be seen. Figure 5.16 shows the final 1420 MHz map which was constructed from the central section of figure 5.15.

5.2 RESULTS

Figures 5.12 and 5.16 show the 408 MHz and 1420 MHz fields containing S183. More detailed maps which have included shading are shown in figures 5.17 and 5.18, for

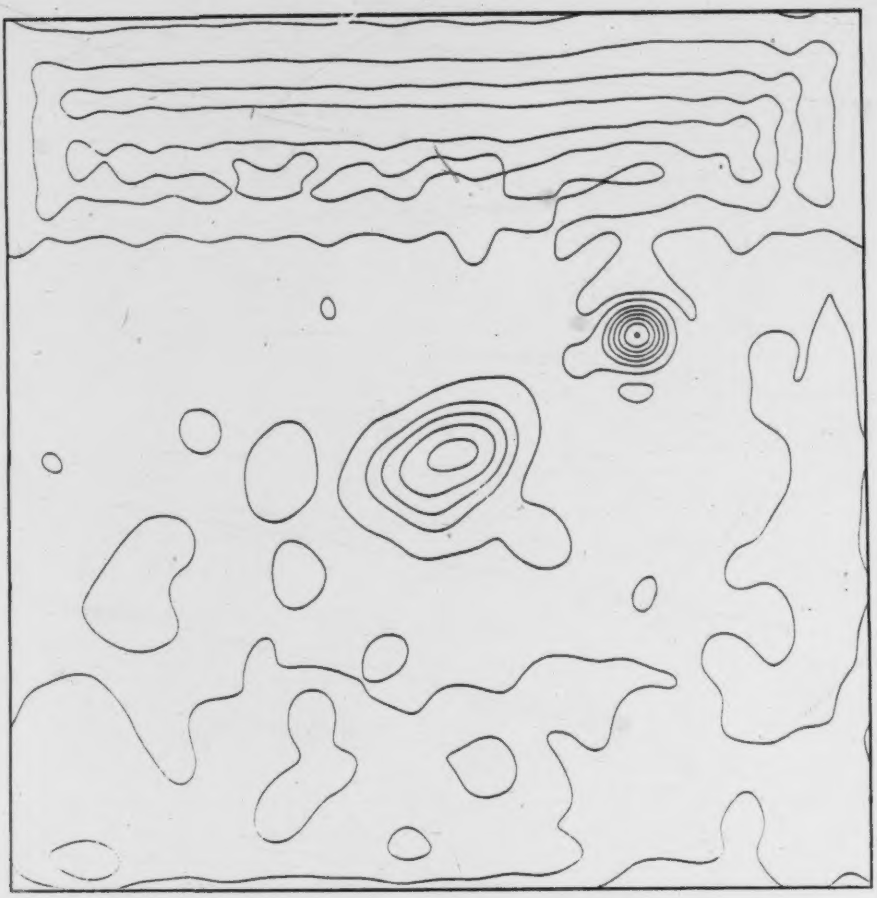

Figure 5.14
The Filtered Low Order 1420 MHz Map

The filtered 1420 MHz low order map. Contours are shown from 1.0 to 3.2 K in steps of 0.3 K. The map is 512 X 512 pixels with each pixel representing 105", making the map 4.3° square. The field center is at RA = 0^h 51^m 30.0^s, DEC = 65° 30′ 0.0".

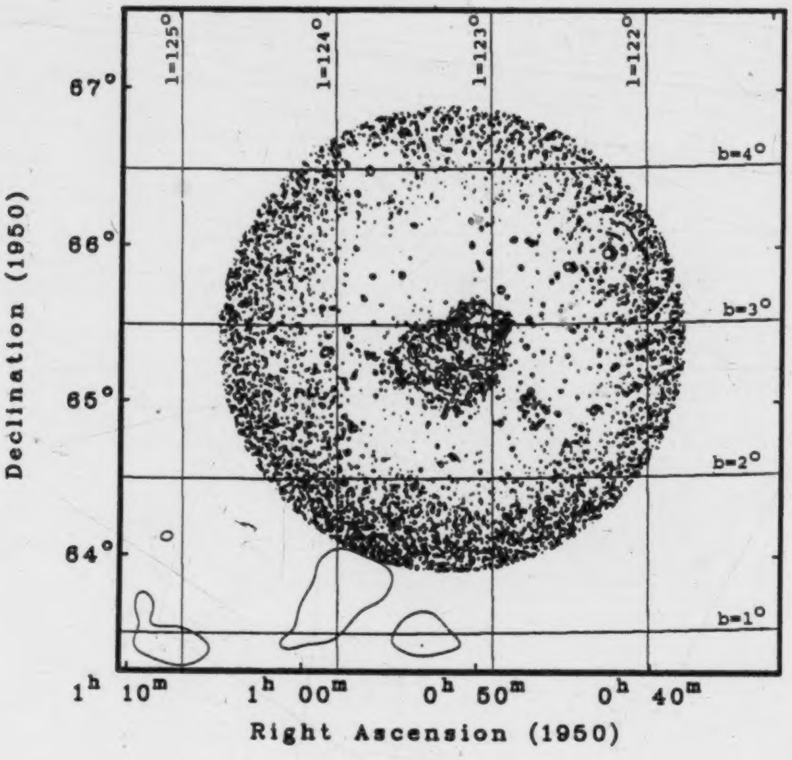

Figure 5.15
The Complete 1420 MHz Map

The 1420 MHz map with the low and high order maps added together. Contours are shown from 1.6 to 4.0 K in steps of 0.4 K. Galactic and equatorial coordinate systems are shown. The map is 512 X 512 with each pixel = 30.0".

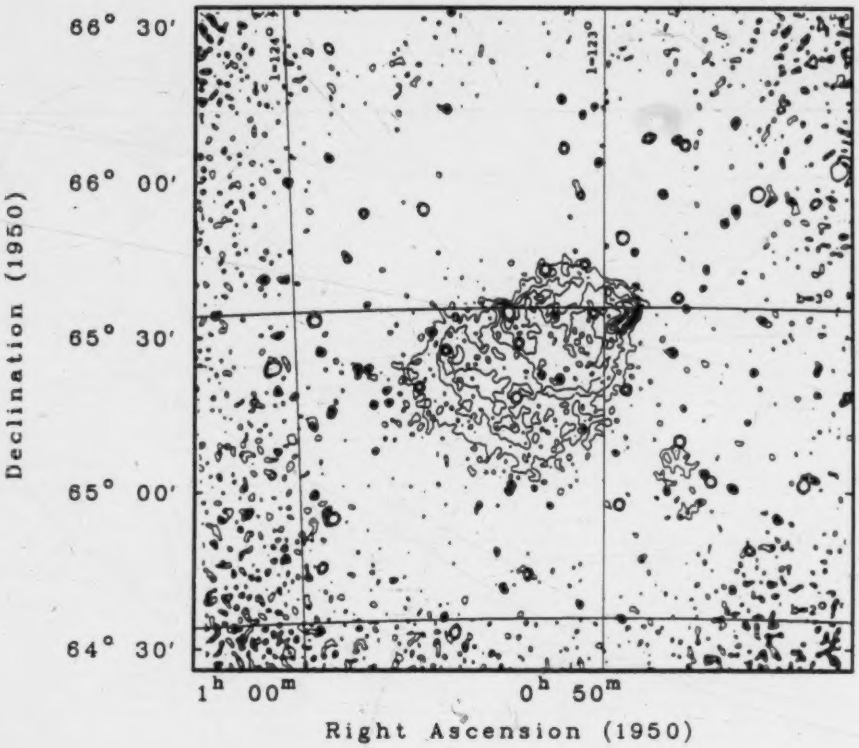

Figure 5.16
The Final 1420 MHz Map

The central 256 X 256 area of the 1420 MHz map shown in figure 7.13. Contours are shown from 1.6 to 4.0 K in steps of 0.4 K. Galactic and equatorial coordinate systems are shown. Pixel size = 30.0".

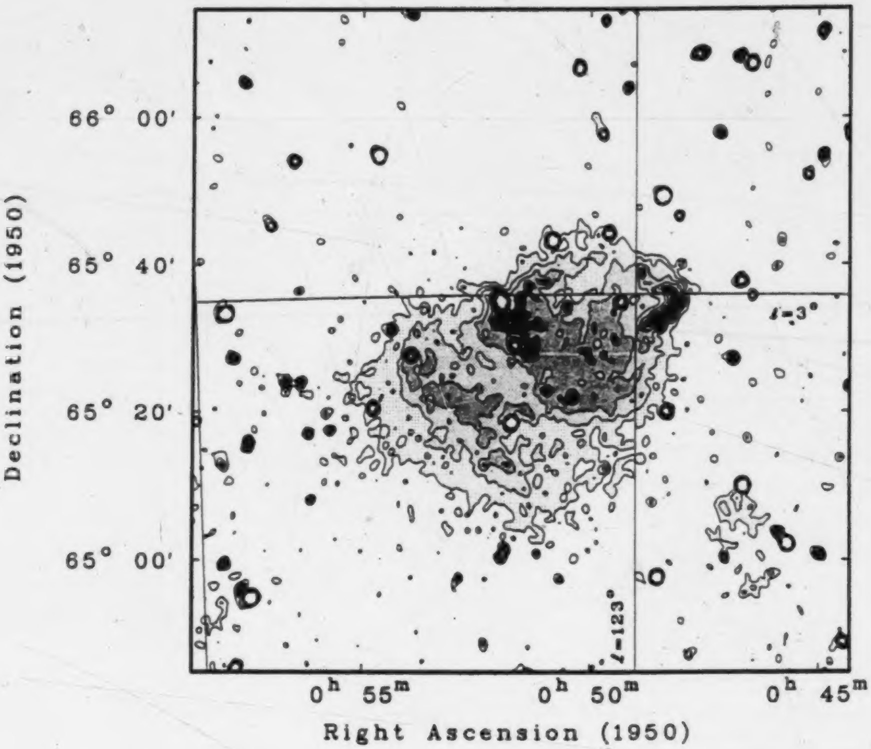

Figure 5.17
The 1420 MHz Map with Shading

Contours of brightness temperature are shown from 1.6 K to 4.0 K in steps of 0.4 K. Beamwidth is 1.0′ X 1.1′ EW X NS.

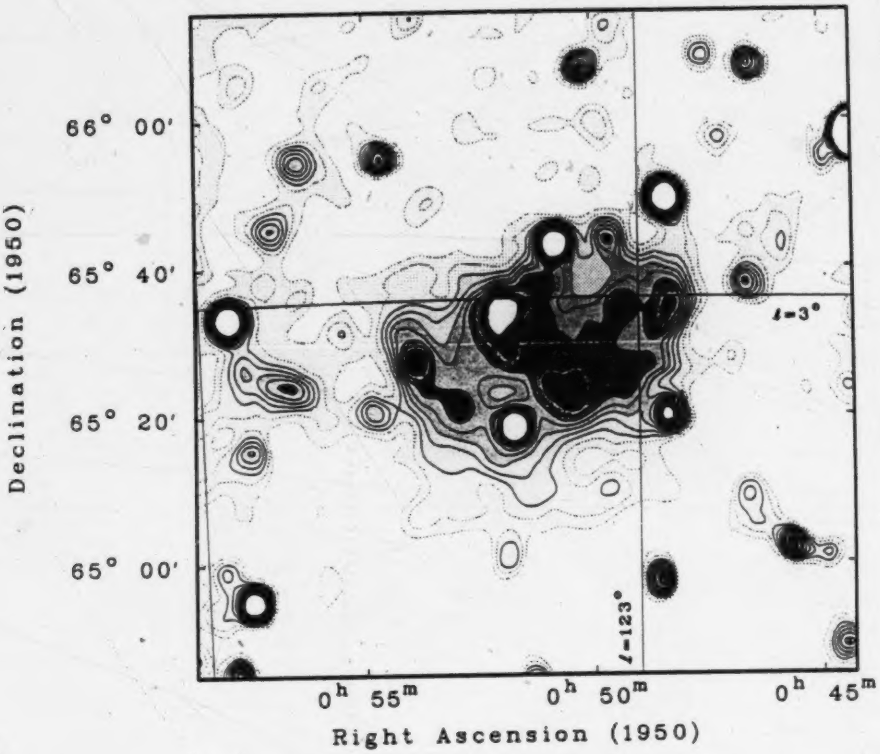

Figure 5.18
The 408 MHz Map with Shading

Contours of brightness temperature are shown from 58.0 K to 78.0 K in steps of 2.0 K. Beamwidth is 3.5' X 3.8' EW X NS.

1420 MHz and 408 MHz respectively. The shading removes any ambiguity in the contour values of figures 5.12 and 5.16.

At 1420 MHz, S183 appears as a region of emission that contains several areas of higher brightness. The most prominent of these is a compact ridge on the west side of S183. It is oriented in the SE-NW direction and has a peak brightness temperature of about 4.7 K. The ridge lies on the W side of a shell-like structure that forms the center of S183. The shell is slightly brighter on the E side as well, which gives it an edge brightened appearance. A slightly fainter region of emission forms the SE side of S183, and has the appearance of a plateau whose peak brightness is patchy and is oriented in the NE-SW direction. The south and east edges of S183 are diffuse and patchy, whereas the north and west edges are generally sharper and more defined. S183 has a similar appearance at 408 MHz. Each of the 1420 MHz features described above can be seen in the lower resolution 408 MHz map.

S183 is also visible on the red print of the Palomar Sky Survey[44], a portion of which is shown on plate 5.1. It appears as an area of obscuration surrounded by faint regions of emission. The ridge-like feature on the W side of S183 is visible, and has the same general shape as it does in the 1420 MHz map.

Plate 5.1

A Section of the Palomar Sky Survey Showing S183

The Palomar Sky Survey Red Print[44] showing the field of S183. In the top print the 1420 MHz contours are superimposed along with the equatorial and galactic coordinate systems. For comparison purposes, the bottom print shows only the S183 field.

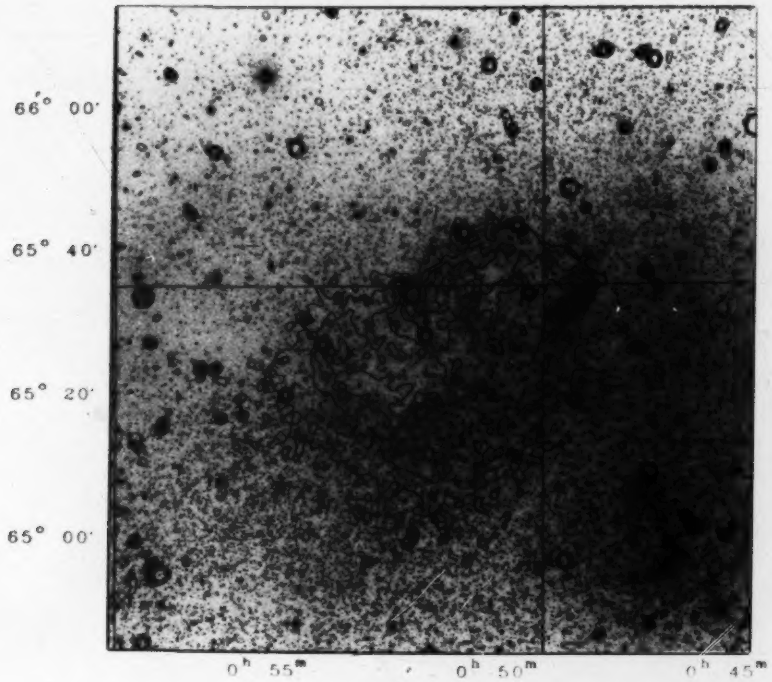
66° 00'
65° 40'
65° 20'
65° 00'
$0^h\ 55^m$
$0^h\ 50^m$
$0^h\ 45^m$

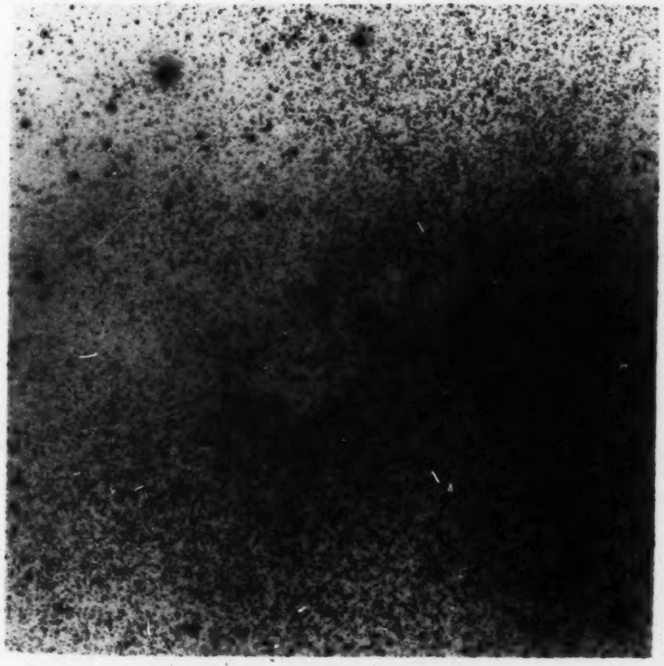

A small region of emission is visible to the SW of S183 on both the radio maps. It also appears on the red print of the Palomar Sky Survey and is designated as LBN 0611.

CHAPTER 6

INTERPRETATION OF OBSERVATIONS OF S183

6.1 408 MHz AND 1420 MHz DATA

6.1.1 DETERMINATION OF SPECTRAL INDEX

The primary reason for surveying S183 with the DRAO synthesis telescope was to reliably classify it either as a supernova remnant or an HII region. The most common tool used to decide which of these categories an object fits into is its spectral index. Spectral index α , is a measure of how the object radiates its energy as a function of frequency, and is defined by

$$\frac{S_2}{S_1} = \left(\frac{\nu_1}{\nu_2}\right)^{\alpha} \qquad 6.1$$

where: S_2 and S_1 = the flux densities at the low and high frequencies ν_2 and ν_1 respectively.

Supernova remnants radiate their energy by synchrotron emission, which has ranges of α from 0.0 to about 0.8. Shell remnants typically have $\alpha = 0.45 \pm 0.2$, and centrally concentrated remnants have $\alpha \leq 0.25$.

An HII region can have a spectral index from -2.0 to

0.1, depending on the optical depth τ of the object. If the optical depth is large ($\tau >> 1$) then $\alpha = -2.0$, however if it is small ($\tau << 1$) then $\alpha = 0.1$. The following discussion illustrates these points.

The brightness temperature T_b of an HII region is[45]

$$T_b = T_e (1 - e^{-\tau}) \qquad 6.2$$

where: T_e = the electron temperature, and
τ = the optical depth.

If the optical depth is large ($\tau >> 1$), the brightness temperature becomes the electron temperature

$$T_b = T_e. \qquad 6.3$$

If the cloud has uniform brightness over its area, and $\tau >> 1$, its flux density S is given by

$$S = \frac{2 k T_e \Omega_s}{\lambda^2} \qquad 6.4$$

where: Ω_s = the solid angle of the source,

T_e = the electron temperature,

λ = the wavelength of observation, and

k = Boltzmann's constant.

From equation 6.4, it can be seen that the flux density of an optically thick region varies as λ^{-2}, and that a spectral index $\alpha = -2.0$ is the result.

If the optical depth is small ($\tau << 1$), then equation 6.2 can be accurately approximated by

$$T_b = T_e \qquad 6.5$$

and the brightness temperature T_b becomes proportional to τ. Altenhoff et al.[46] state that τ can be expressed as the approximation

$$\tau = 8.235 \times 10^{-2} T_e^{-1.35} \nu^{-2.1} \int N_e^2 \, dl \qquad 6.6$$

for $\nu << 10$ GHz, and $T < 9 \times 10^5$ K

where: T_e = the electron temperature in K

N_e = the electron density in cm^{-3}, and

ν = the frequency in GHz.

The integral term in equation 6.6 is the emission measure in parsec cm^{-6}, where 1 parsec = 3.086 X 10^{18} cm.

From equation 6.4, and using equations 6.5 and 6.6 the flux density in an optically thin region is

$$S = \frac{2k\,(T_e\,\tau)}{\lambda^2}\,\Omega_s$$

$$\text{or} \qquad S \propto \frac{\tau}{\lambda^2} = \frac{1}{\nu^{2.1}\,\lambda^2}$$

$$\text{or} \qquad S \propto \frac{\lambda^{2.1}}{\lambda^2} = \lambda^{0.1}. \qquad 6.7$$

Therefore, in the optically thin case, the flux density is proportional to the wavelength raised to 0.1. This means that the spectrum is essentially flat, or that the spectral index is very close to zero.

To obtain the spectral index, values of flux densities were obtained at 408 MHz and 1420 MHz from the maps shown in figures 5.18 and 5.17 respectively, using the program AIM(INTEGRATE). The program sums pixel values above a background level inside polygons drawn on a CRT display using a trackball. The background for each pixel is determined by fitting a twisted plane through the data values at the corners of the polygon. The pixel values are summed inside the polygon after background subtraction, and then converted to flux density.

Table 6.1 lists five measurements of flux density at 408 MHz, and eight measurements of flux density at 1420 MHz. The flux density values have been averaged to obtain 6.92 ± 0.50 Jy at 408 MHz and 6.33 ± 0.40 Jy at 1420 MHz. In addition to the 5 polygons used in the 408 MHz average, a sixth polygon was defined with boundaries significantly outside those of S183. From this polygon the flux density was 10.11 Jy, showing that the measurement is very dependent on locating the boundaries of S183 accurately. Changing the location of the sides of the polygon has the effect of changing the value of background that is subtracted in the determination of flux density.

The polygons used for each measurement are shown on figures 6.1 and 6.2, for 408 MHz and 1420 MHz respectively. The values of flux density for 408 MHz and 1420 MHz include the contributions of point sources that are contained within the boundaries of S183. This enables direct comparison of these flux densities with those measured previously with broader beams.

TABLE 6.1

FLUX DENSITY MEASUREMENTS OF S183

408 MHz

Polygon #	Flux Density (Jy)
1	6.081
2	7.087
3	7.254
4	7.303
5	6.871
6	10.107

Ave (excluding # 6) = 6.92 ± 0.50

1420 MHz

Polygon #	Flux Density (Jy)
1	6.275
2	6.659
3	6.137
4	5.872
5	5.879
6	6.169
7	6.698
8	6.977

Ave = 6.33 ± 0.40

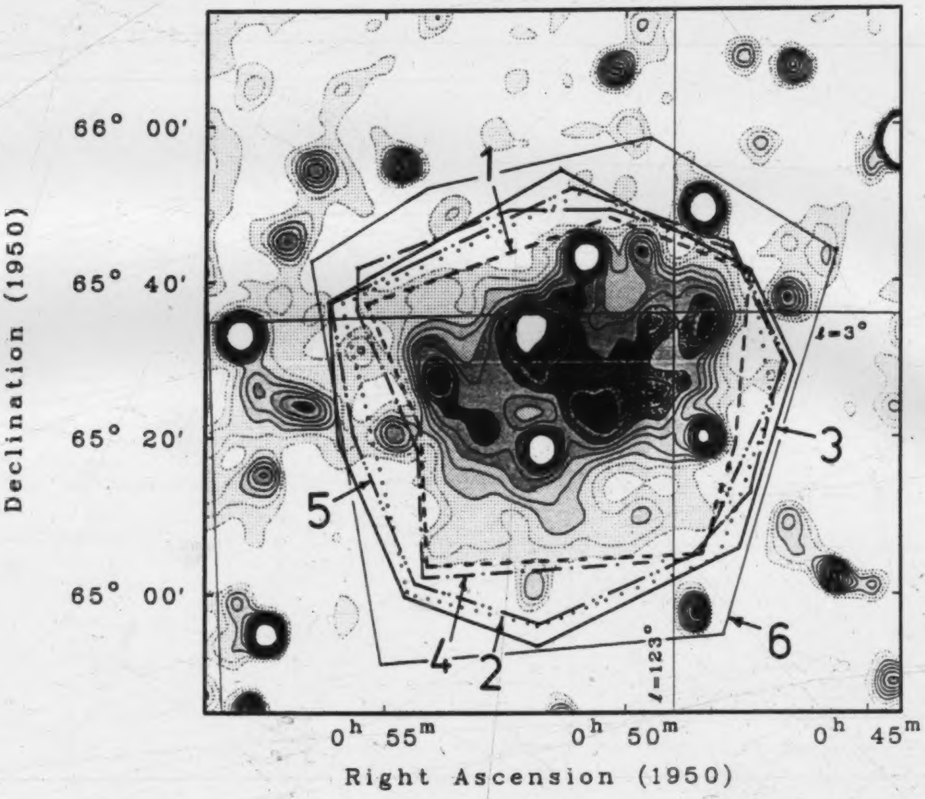

Figure 6.1
The 408 MHz Polygons

Polygons used for the determination of 408 MHz flux density. Polygons 1 to 5 are drawn around S183 on its approximate boundary. Polygon 6 is drawn to include a greater area to illustrate what effect poor resolution has on the flux density measurement.

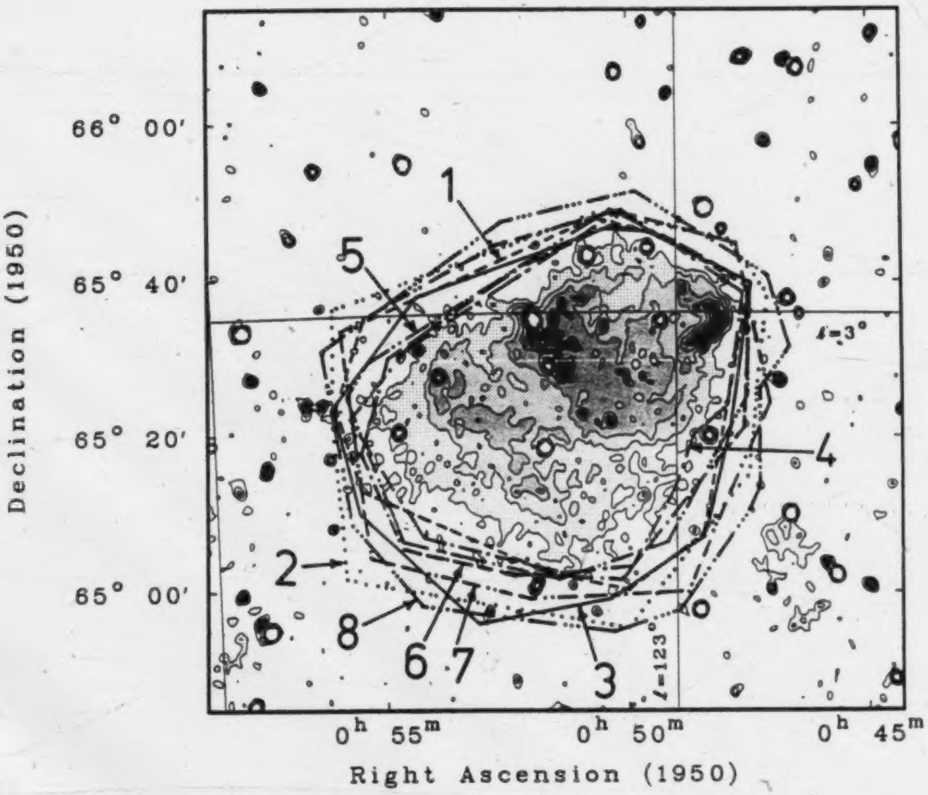

Figure 6.2
The 1420 MHz Polygons

Polygons used for the determination of 1420 MHz flux density.

9

The flux density measurements of S183 at 408 MHz and 1420 MHz are listed in table 6.2 along with previous measurements of the object at other frequencies. The spectrum of S183, which is shown in figure 6.3, is obtained by plotting the flux density values of table 6.2 versus frequency. A spectral index of $\alpha = 0.10 \pm 0.05$ is obtained by fitting a weighted least squares line through the measurements listed in table 6.2. The measurement by Bonsignori-Facondi and Tomasi[50] in 1979 at 408 MHz was not included in the spectral index determination because of poor resolution in the N-S direction (110′). It was this measurement that suggested that S183 was a supernova remnant.

For comparison, the spectral index of S183 using only the DRAO flux density measurements is $\alpha = 0.07 \pm 0.07$. This estimate includes the point sources, which are probably mostly extragalactic with steep synchroton spectral indices. Including the sources will steepen the spectral index slightly.

The value of $\alpha = 0.10 \pm 0.05$ shows that S183 is probably an HII region instead of a supernova remnant,as was suggested by Bonsignori-Facondi and Tomasi[50]. A spectral index of ~ 0.1 does not rule out the possibility that S183 is a supernova remnant of the type resembling the Crab Nebula. However, the appearance of S183 is not typical

TABLE 6.2 MEASURED FLUX DENSITIES FOR S183

Frequency (MHz)	Resolution (arcmin)	Flux (Jy)	Observers	Year
2695	18	5 ± 1.5	Churchwell & Walmsley[47]	1973
1420	36	4.8 ± 1.0	Galt & Kennedy[48]	1968
1420	1.0	6.33 ± 0.40	This work	1987
1400	10	7.1 ± 2.5	Felli & Churchwell[48]	1972
408	4.2 X 110	11.5 ± 1.7	Bonsignori-Facondi & Tomasi[50]	1979
408	3.5	6.92 ± 0.50	This work	1987

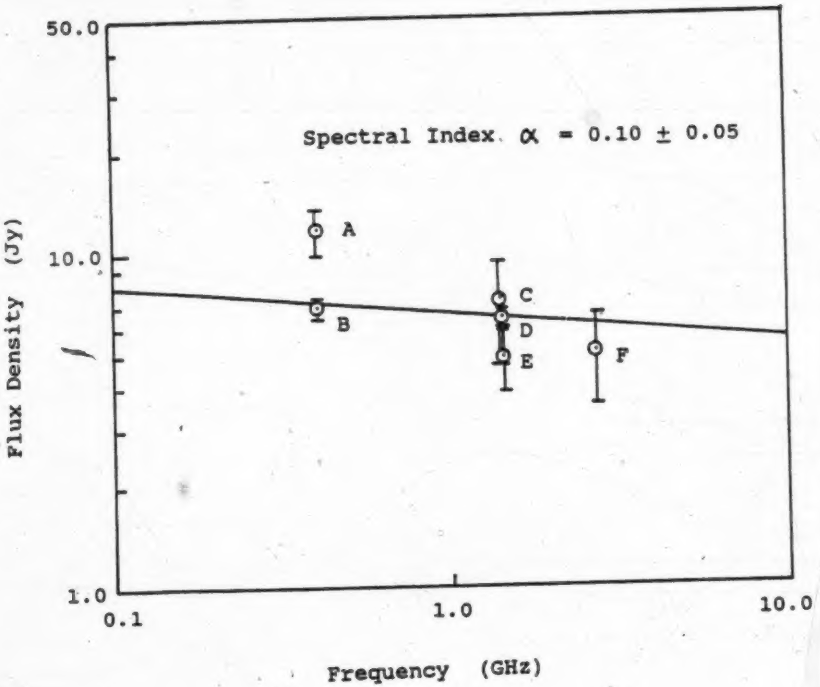

Figure 6.3
The Radio Spectrum of S183

A spectral index α = 0.10 ± 0.05 is obtained by fitting a weighted least squares straight line though the data in table 6.2. The individual measurements are: A) Bonsignori-Facondi & Tomasi, B) this work, C) Felli & Churchwell, D) this work, E) Galt & Kennedy, and F) Churchwell & Walmsley. The flux density measurement by Bonsignori-Facondi and Tomasi was not included in the determination of α because of poor N-S resolution (110').

of the centrally concentrated Crab-like supernova remnants. Furthermore, other evidence to be presented later makes the HII region interpretation the most plausible one.

A brightness temperature spectral index β , may also be calculated. If the Rayleigh-Jeans law (equation 6.8),

$$S = \frac{2kT}{\lambda^2} \qquad 6.8$$

is substituted into equation 6.1, it follows immediately that

$$\frac{T_2}{T_1} = \left(\frac{\nu_1}{\nu_2}\right)^{\beta} \qquad 6.9$$

where: T_2 and T_1 = the brightness temperatures at the low and high frequencies ν_2 and ν_1 respectively, and that $\beta = 2 + \alpha$, where α is the spectral index of equation 6.1.

Figure 6.4 is a brightness temperature spectral index map of S183. To make the map, a background of 58.0 K was subtracted from the 408 MHz map, and 1.6 K was removed from

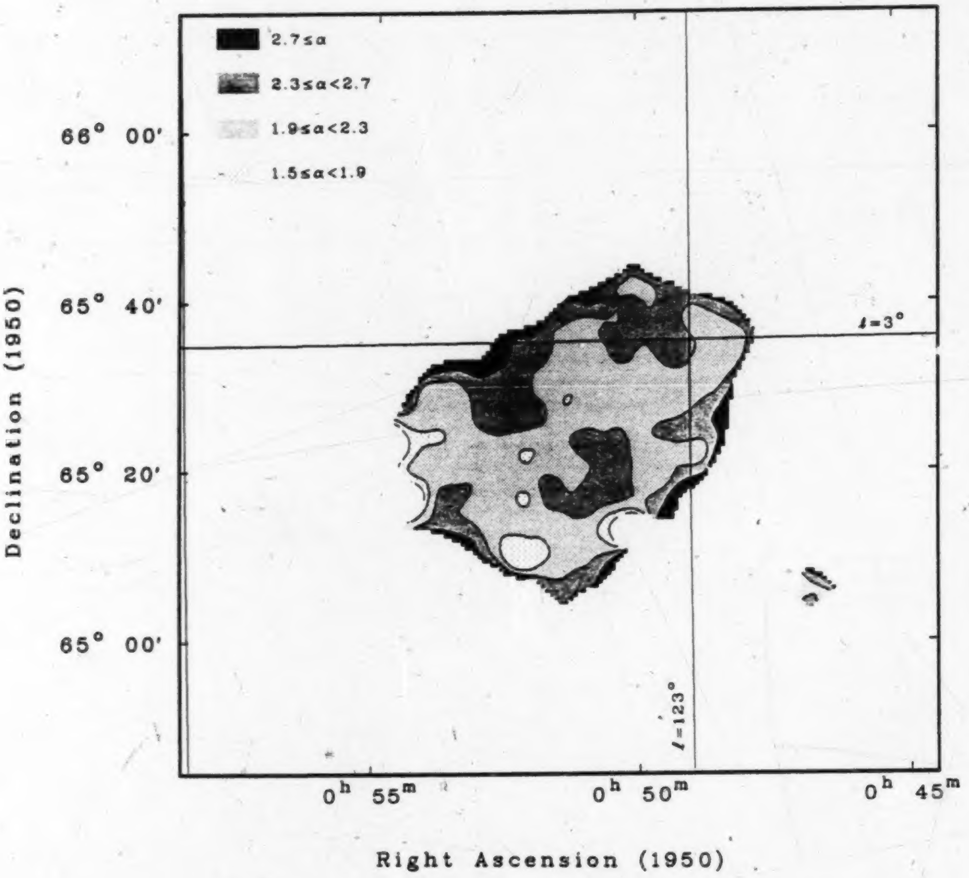

Figure 6.4

The Brightness Temperature Spectral Index Map of S183 the 1420 MHz map. Equation 6.9 was solved for β giving equation 6.10 below.

$$\beta = \frac{\log_{10}\left(\frac{T_2}{T_1}\right)}{\log_{10}\left(\frac{\nu_1}{\nu_2}\right)} \qquad 6.10$$

The 1420 MHz map was smoothed to the resolution of the 408 MHz map. Then the 408 MHz map and the smoothed 1420 MHz map were used as inputs for equation 6.10. The MANIPULATOR feature of the program MADR was used to calculate β for each pixel of the brightness temperature spectral index map.

A brightness temperature spectral index of approximately 2.0 to 2.1 is consistent with an optically thin HII region. It can be seen , by looking at the map in figure 6.4, that most values of β within the boundaries of S183 fall within the limits $1.9 < \beta < 2.3$. A supernova remnant would likely have values of β clustered around a value in the range 2.2 to 2.7 on such a map. There are some areas around the edge of S183 that have either a high or low spectral index. These are errors caused by taking ratios of small numbers in T_2/T_1 of equation 6.10, after the backgrounds have been subtracted.

6.1.2 A MODEL OF S183

The appearance of S183 suggests that we are looking at shells of ionized gas. One shell, nearly complete, has a diameter of about 20' and is centered at $0^h 50^m$, 65° 30'. A second incomplete shell lies to the south-east.

Therefore, S183 can be modeled as an HII region made up of two separate components. The first component is the circular region that has edge brightening on the east and west sides. This can be modeled as a shell of gas with inside and outside diameters of 15' and 25'. The second component is the slightly fainter region of emission that forms the SE side of S183. It can be modeled as a hemispherical shell of gas with inside and outside diameters of 20' and 35'. Figure 6.5 shows the model of S183 with the various angular dimensions labeled. The angular sizes of S183 were obtained from measurements on the 408 MHz and 1420 MHz maps shown in figures 5.18 and 5.17, and are essentially the same at both frequencies.

Figure 6.6 shows the model of S183 with the brightness temperatures of the various parts labeled after the background was removed. The model parameters of size, optical depth, electron temperature, and electron density

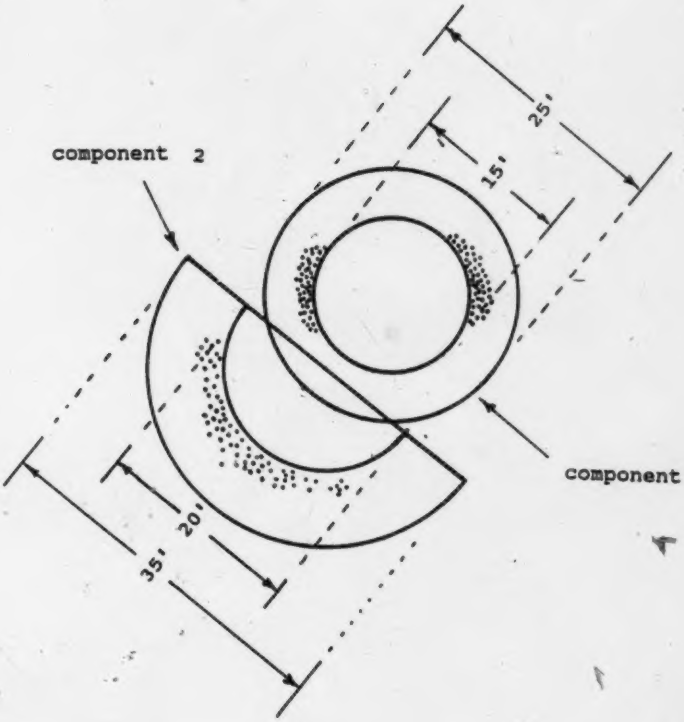

Figure 6.5
Model of S183

Shell model of S183, showing components 1 and 2, with angular dimensions labeled. The shaded (rim) areas approximate the regions of higher brightness temperature seen in the maps shown on figures 5.18 and 5.17.

408 MHz

(58 K background removed)

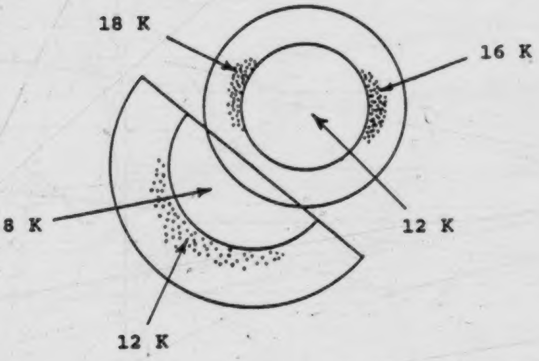

1420 MHz

(1.6 K background removed)

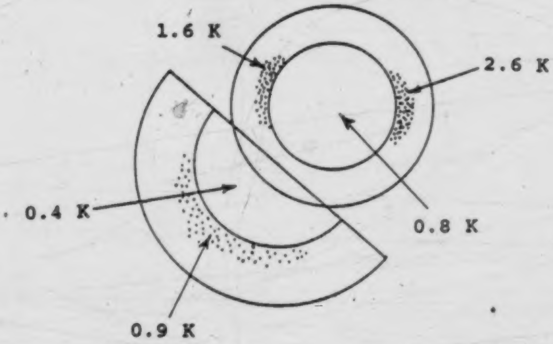

Figure 6.6
Brightness Temperatures of the Components of S183

S183 showing central and rim brightness temperatures for components 1 and 2 at 408 MHz and 1420 MHz.

must be chosen such that the model will predict the appearance of S183 as is shown in figure 6.6.

The basic question that must be answered, before attempting to determine the physical parameters of the model, is the distance to S183. Fich and Blitz[51] determined a kinematic distance to S183 in 1984. It is based on a rotation curve for the outer Galaxy, the assumption that a CO cloud with a measured radial velocity of -10.3 km s^{-1} in this direction is associated with S183, and the assumption that all the objects in the Galaxy are undergoing only circular motion. The rotation curve for the Galaxy was based on HI terminal velocities from the first quadrant of the inner Galaxy[52] and CO velocities and distances to exciting stars of optical HII regions in the outer Galaxy[53]. The rotation curve used by Fich and Blitz is shown in figure 6.7, and is used in the following manner to obtain an estimate of the distance to S183.

The galactic rotation velocity ω (km s^{-1} kpc^{-1}) of any object orbiting in the plane of the Galaxy is given by[54]

$$\omega = \frac{V_r \cos b}{R_0 \sin l} + \omega_0 \qquad 6.10$$

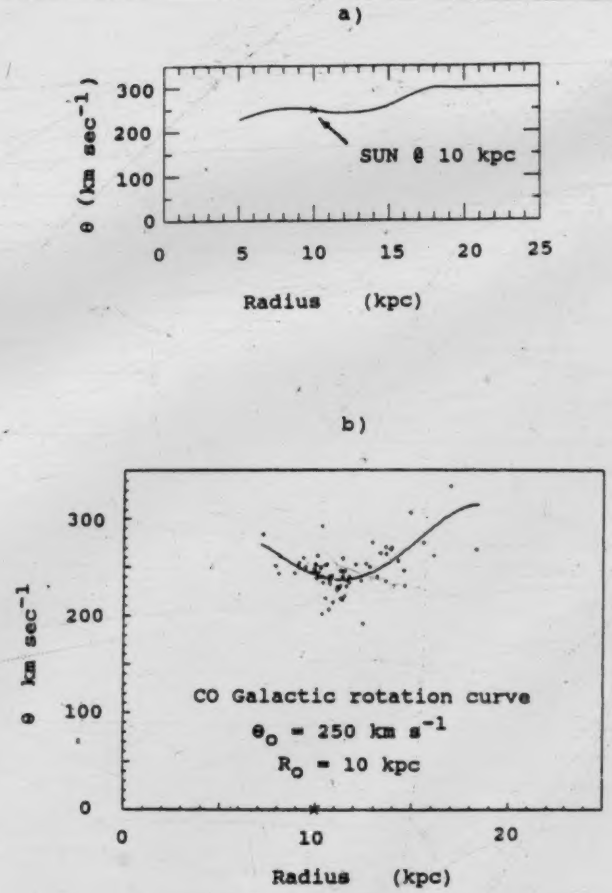

Figure 6.7
Rotation Curve of the Galaxy

a) Galactic rotation curve, (Adapted from Fich and Blitz[51]) used to determine the distance to S183.

b) The CO rotation curve of the outer Galaxy showing the data points which are omitted in the top curve (Adapted from Blitz and Fich[55]).

where: V_r = the measured radial velocity of an object,

R_o = the distance of the sun from the galactic center,

b and ℓ = the galactic latitude and longitude of the object, and

ω_o = the angular velocity of the Sun about the galactic center (km s^{-1} kpc^{-1}).

Fich and Blitz[51] used 25 km s^{-1} kpc^{-1} for ω_o and 10 kpc for R_o. A value for ω is found by substituting the galactic coordinates for S183 and the values for V_r,R_o and ω_o into equation 6.10. The tangential velocity θ was then determined to be 238 km s^{-1} using equation 6.11 below.

$$\theta = R_o \omega \qquad 6.11$$

Given that θ = 238 km s^{-1}, Fich and Blitz[51] then found R_{S183} = 10.42 ± 0.3 kpc by numerically interpolating on the rotation curve in figure 6.7a. Then by geometry, the distance to S183 was found to be d = 0.74 ± 0.51 kpc.

The large relative uncertainty in the distance is due to the flat slope of the rotation curve in the locality of the Sun. As well, the data on which the rotation curve is based has significant scatter, as is shown in figure 6.7b. This means that a fairly broad range of R could satisfy the angular velocity requirement of $\Theta = 238$ km s^{-1}. However, for the model calculations, the distance to S183 will be assumed to be accurate, and equal to 0.74 kpc.

To arrive at a model for S183 the following list of parameters was calculated using the DRAO program RADPHYS written by Higgs[56]:

1) opacity (κ)
2) optical depth (τ)
3) brightness temperature (T_b)
4) emission measure (EM)
5) mass (M)
6) flux density (S)
7) excitation parameter (U)

The program requires values for electron temperature (T_e), electron density (N_e), distance (d), angular size, frequency of observation, and the percentage of singly ionized He. Of these, the frequency, angular size and distance are known, the first two from the survey, and the distance from Fich and Blitz[51]. To calculate the mass, the percentage of singly ionized He has been assumed to be 14%. The electron temperature has been assumed to be 8000 K, which is typical for HII regions.

With T_e, d, and angular dimensions held constant, the value of electron density was varied, and a table of output parameters was constructed for each frequency. By looking at the tables, an electron density that correctly predicts the observations at 408 MHz and 1420 MHz can be found. Using this approach, the parameters of a model for S183 were obtained.

The following example is a detailed explanation of the calculations that are performed by RADPHYS. The example is applied to component 1 of S183 shown in figure 6.5.

1) Calculation of opacity (κ)

The first step in calculating the parameters of the model for S183 is the determination of opacity cm^{-1} (κ). The required input values are: frequency (ν = 1420 MHz), electron temperature (T_e = 8000 K), and electron density (N_e = 10 cm^{-3}). For small $h\nu/kT$, the expression in c.g.s. units for opacity (cm^{-1}) is[57]

$$\kappa = \frac{8}{3}\left(\frac{\pi}{6}\right)^{1/2} \frac{e^6}{c\,(M_e k T_e)^{3/2}} \frac{Z^2 g}{\nu^2} N_e N_i \qquad 6.12$$

where: e = charge of the electron,

M_e = mass of the electron,

k = Boltzmann's constant,
T_e = electron temperature,
N_e, N_i = number density of electrons and ions,
Z = the ionic charge ,
g = the Gaunt factor, and
ν = the frequency of observation.

The Gaunt factor g in equation 6.13 is given by Lang[58] as ,

$$g = \frac{\sqrt{3}}{\pi} \ln \left[\left(\frac{2}{\gamma}\right)^{5/2} \left(\frac{kT_e}{M_e}\right)^{1/2} \left(\frac{kT_e}{2\pi Z e^2 \nu}\right) \right] \qquad 6.13$$

for: $\omega >> \omega_p$, where $\omega_p = 5.64 \times 10^4 N_e^{1/2}$, $T < 3.6 \times 10^5 Z^2$ K, and $\gamma = 1.781$.

Using equation 6.13, $g = 5.58$ for $T_e = 8000$ K and $\nu = 1420$ MHz. Using this, equation 6.12 is evaluated, and the opacity is found to be

$$\kappa = 6.84 \times 10^{-24} \text{ cm}^{-1}$$
$$\text{or} \quad \kappa = 2.11 \times 10^{-5} \text{ pc}^{-1},$$

where 1 pc = 3.086×10^{18} cm.

2) Calculation of optical depths (τ)

Next, to calculate optical depths for S183, the actual dimensions (D) of the shell in parsecs are needed. They are calculated using

$$D = d \Delta \phi \qquad 6.14$$

where: d = the distance in parsecs to S183 (740 pc),

$\Delta\phi$ = the angular dimension of the feature being considered (15' and 25' for the inside and outside diameters of the shell for component 1).

Using equation 6.14, the inside and outside diameters of the shell are found to be

$D_i = 3.23$ pc

$D_o = 5.38$ pc.

The optical depth along two paths were calculated, the maximum path length (l_m) and the central path length (l_c). These are shown on figure 6.8a. Figure 6.8b shows the

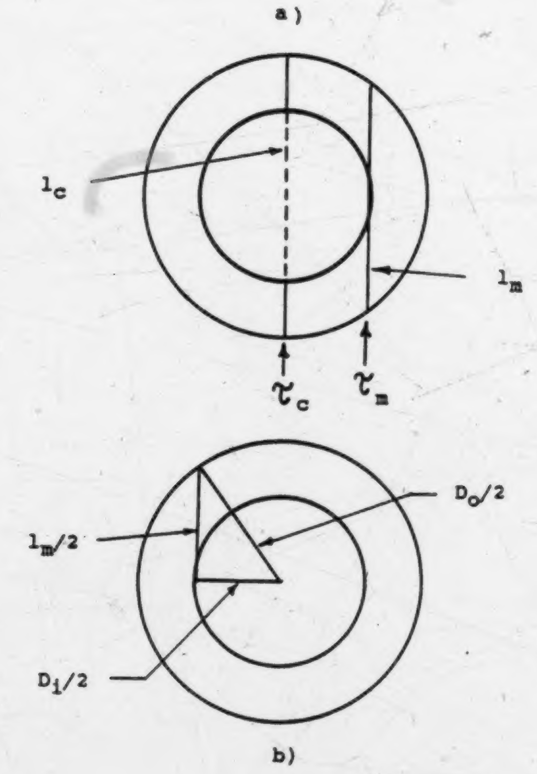

Figure 6.8
Cross-Section Through Component 1 of S183

a) Model of S183 showing shell cross-section. Path lengths l_c and l_m are shown for which various parameters are calculated.

b) Shell cross-section showing the quantities $l_m/2$, $D_o/2$, and $D_i/2$ used to calculate l_m.

quantities used in equation 6.15 below to calculate l_m.

$$l_m = 2\sqrt{\left(\frac{D_o}{2}\right)^2 - \left(\frac{D_i}{2}\right)^2} \qquad 6.15$$

The above values of 3.23 pc and 5.38 pc for D_i and D_o result in

l_m = 4.3 pc, and

$l_c = D_o - D_i$ = 2.15 pc.

Rohlfs[59] defines optical depth as

$$\tau = \int_0^S \kappa \, ds \qquad 6.16$$

where: κ = the opacity, and

S = the path length.

In this case,

$\tau_m = \kappa l_m = 9.07 \times 10^{-5}$

and $\tau_c = \kappa l_c = 4.54 \times 10^{-5}$.

3) Calculation of brightness temperature (T_b)

Since the above values of τ are small, equation 6.5 can be used to calculate the brightness temperatures as follows

$$T_{b\ m} = T_e\ \tau_m = 8000(9.07 \times 10^{-5}) = 0.73\ K, \text{ and}$$
$$T_{c\ c} = T_e\ \tau_c = 8000(4.54 \times 10^{-5}) = 0.36\ K.$$

4) Calculation of emission measure (EM)

Emission measure is defined by Rohlfs[59] to be

$$EM = \int_0^S N_e^2\ ds \qquad 6.17$$

where: N_e = number density of electrons (cm^{-3}) and,
S = path length (pc).

With the assumed electron density $N_e = 10\ cm^{-3}$, and the dimensions $l_m = 4.3$ pc and $l_c = 2.15$ pc, the corresponding emission measures can be found.

$$EM_m = 10^2(4.3) = 430\ cm^{-6}\ pc$$
$$Em_c = 10^2(2.15) = 215\ cm^{-6}\ pc$$

5) Calculation of mass (M)

The mass of hydrogen (in solar masses $M_\odot$) of a spherical shell of HII is given by[60]

$$M_{HT} = \frac{\pi}{6} \frac{(D_o^3 - D_i^3)(3.086 \times 10^{18})^3 N_e M_H}{M_\odot \; (1 + FI_{He} P_{He})} \qquad 6.18$$

where: D_i and D_o = the inside and outside diameters of the shell in parsecs,

N_e = number density of electrons cm^{-3},

M_H = mass of hydrogen atom (1.673×10^{-24} g),

$M_\odot$ = mass of the Sun (1.989×10^{33} g),

FI_{He} = fraction of helium assumed to be singly ionized (1.0),

P_{He} = % of He in nebula (14 %), and

3.086×10^{18} = the conversion from parsecs to cm.

Evaluating equation 6.18 for $N_e = 10$ cm^{-3} gives

$$M_{HT} = 13.87 \; M_\odot .$$

The total mass (M_T) is then found by using

$$M_T = M_{HT}(1.03 + 4.0(P_{He})) \qquad 6.19$$

The total mass is then

$$M_T = 22.1\ M_\odot .$$

6) Calculation of flux density (S)

The expression for flux density is given by[60]

$$S = \frac{2}{3}(1\times 10^{23})\left(\frac{2k\,\nu^2}{c^2}\right)(\kappa\, Te)(D_oA_o - D_iA_i) \qquad 6.20$$

where: k = Boltzmann's constant,

ν = frequency (Hz),

c = velocity of light (cm s^{-1}),

κ = opacity (pc^{-1}),

T_e = electron temperature (K),

A_i and A_o = the solid angles of the inside and outside surface of the shell in steradians, using 15' and 25' for their angular dimensions, and

D_i and D_o = the diameter of the inside and outside surface of the shell in pc.

Using equation 6.20, the flux density was found to be

$$S = 1.22 \text{ Jy}.$$

7) Calculation of excitation parameter (U)

The last item to be calculated in the above list is excitation parameter (U). It is given by[60]

$$U = \left[\frac{3 N_e^2 (D_o^3 - D_i^3)}{8\pi} \right]^{1/3} \qquad 6.21$$

where: N_e = electron density (cm^{-3}),
D_o = outside diameter of shell (pc), and
D_i = inside diameter of shell (pc).

Using D_i and D_o = 3.23 pc and 5.38 pc, the excitation parameter U is

$$U = 11.34 \text{ pc cm}^{2/3}$$

The above values 1) through 7) were calculated for component 1 of S183 at 1420 MHz, assuming an electron density $N_e = 10$ cm^{-3}. These values form the first line of data in table 6.3, which is a tabulation of parameters 1)

TABLE 6.3 DETERMINATION OF MODEL PARAMETERS FOR S183

f (MHz)	N_e (cm^{-3})	Optical Depth (τ_c (X 10^{-4})	τ_m)	Opacity (κ) (X 10^{-4}) (pc^{-1})	Excitation Parameter (U) ($cm^{-2}pc$)	Emission Measure (EM_c ($cm^{-6}pc$)	EM_m)	Flux Density (S) (Jy)	Brightness Temperature ($T_{b\ c}$ (K)	$T_{b\ m}$)	Mass (H) ($M_\odot$)	(H + He)
						COMPONENT 1						
1420	10	0.45	0.91	0.212	11.3	215	430	1.22	0.36	0.73	13.9	22.1
	15	1.02	2.05	0.476	14.9	484	968	2.76	0.82	1.64	20.8	33.1
	17.5	1.39	2.79	0.648	16.5	659	1318	3.75	1.12	2.23	24.3	38.6
	20	1.82	3.64	0.846	18.0	861	1722	4.90	1.45	2.90	27.8	44.1
408	10	6.20	12.4	2.88	11.3	215	430	1.37	4.95	9.90	13.9	22.1
	12	8.92	17.8	4.14	12.8	309	620	1.98	7.14	14.3	16.7	26.4
	15	13.9	27.9	6.48	14.8	484	968	3.09	11.2	22.3	20.8	33.1
	20	24.8	49.6	11.5	18.0	861	1722	5.50	19.8	39.7	27.8	44.1
						COMPONENT 2						
1420	8	0.44	0.84	0.135	13.8	206	395	1.12	0.35	0.67	15.8	25.1
	10	0.68	1.31	0.212	16.1	322	618	1.75	0.55	1.05	19.8	31.4
	12	0.98	1.88	0.305	18.0	465	890	2.51	0.79	1.51	23.7	37.7
408	8	5.95	11.4	1.84	13.9	206	395	1.26	4.75	9.11	15.8	25.1
	10	9.29	17.8	2.88	16.1	322	618	1.95	7.40	14.2	19.8	31.4
	12	13.4	25.6	4.14	18.2	465	890	2.82	10.7	20.5	23.7	37.7

through 7) for components 1 and 2 of S183 at both 408 MHz and 1420 MHz. The table was generated by holding the inputs constant for each frequency while varying the electron density N_e. The electron temperature was assumed to be 8000 K for all of the calculations.

The idea behind table 6.3 is that the true electron density of each component of S183 should fall within the range of tabulated values. If this is the case, the values of brightness temperature listed in table 6.3 that are associated with that electron density, should correctly predict the rim and central brightness temperatures for each component of S183 (shown in figure 6.6), at both 408 MHz and 1420 MHz.

Table 6.4 is a listing of T_b for the rim (the maximum brightness temperature) and the central brightness temperature for both components of S183, at 408 MHz and 1420 MHz. Backgrounds of 58 K and 1.6 K have been removed at the low and high frequencies respectively. Now, an electron density must be found for each component of S183 in table 6.3, that correctly predicts the values of T_b. By inspection, it can be seen that for component 1, an electron density of 17.5 cm^{-3} for 1420 MHz, and 15 cm^{-3} for 408 MHz comes reasonably close to predicting the observed values in table 6.4. For component 2, a good agreement exists between the predicted and observed temperature

TABLE 6.4 MEASURED BRIGHTNESS TEMPERATURES OF S183
(From figure 6.5)

Component	Frequency (MHz)	T_b central (K)	T_b max. (rim) (K)
1	408	12.0	17.0
	1420	0.8	2.1
2	408	8.0	12.0
	1420	0.4	0.9

brightness values at $N_e = 10\ \mathrm{cm}^{-3}$.

Table 6.5 shows the predicted values of brightness temperature (T_b) that have been extracted from table 6.3 using $N_e = 16\ \mathrm{cm}^{-3}$ for component 1, and $N_e = 10\ \mathrm{cm}^{-3}$ for component 2. The values for $N_e = 16\ \mathrm{cm}^{-3}$ were interpolated from table 6.3 using second order polynomials. By comparing the values in tables 6.4 and 6.5, it can be seen that reasonable agreement exists between the measured and model values of brightness temperature. This validates the choice of $N_e = 16\ \mathrm{cm}^{-3}$ for component 1, and $N_e = 10\ \mathrm{cm}^{-3}$ for component 2, of S183. Table 6.6 lists the complete set of model parameters for S183 at 408 MHz and 1420 MHz.

The remaining task is to combine the results for components 1 and 2, to obtain an average electron density, and mass for S183 as a whole. Components 1 and 2 have approximate volumes of 64 pc^3 and 91 pc^3 with electron densities of 16 cm^{-3} and 10 cm^{-3} respectively. Using a weighted average, the electron density for S183 works out to be

$$N_e = 12.5\ \mathrm{cm}^{-3}.$$

The model predicts a flux density of 5.47 Jy at 408 MHz, and 4.89 Jy at 1420 MHz as compared to measured values of 6.92 Jy and 6.33 Jy for the same frequencies. Therefore

TABLE 6.5 MODEL BRIGHTNESS TEMPERATURES OF S183
(Extracted from table 6.3)

Component	N_e (cm^{-3})	Frequency (MHz)	T_b central (K)	T_b max. (rim) (K)
1	16	408	12.7	25.4
		1420	0.94	1.87
2	10	408	7.4	14.2
		1420	0.55	1.05

TABLE 6.6 LIST OF PARAMETERS FOR THE MODEL OF S183

(Assuming Te = 8000 K, d = 740 pc, and angular dimensions as shown on fig. 6.5)

Parameter	Component 1		Component 2	
	408 MHz	1420 MHz	408 MHz	1420 MHz
Electron density N_e (cm^{-3})	16		10	
Optical Depth ($\tau \times 10^{-3}$)				
Central	1.58	0.12	0.93	0.068
Max. (rim)	3.17	0.23	1.78	0.13
Opacity ($\kappa \times 10^{-3}$)	0.737	0.054	0.288	0.021
Brightness Temp. T_b (K)				
Central	12.7	0.93	7.4	0.55
Max. (rim)	25.4	1.87	14.2	1.05
Emission Measure EM ($cm^{-6}pc$)				
Central	551		322	
Max. (rim)	1102		618	
Excitation Parameter U ($pc\ cm^{2/3}$)	15.5		16.1	
Flux S (Jy)	3.52	3.14	1.95	1.75
Mass ($M_\odot$)				
Hydrogen	22.2		19.8	
Hydrogen + Helium	35.3		31.4	

the model under-predicts the flux density, but it still comes very close considering the uncertainties involved. For example, the distance given by Fich and Blitz[51] has uncertainty of ± 510 pc in a distance of 740 pc.

The mass of hydrogen contained within S183 is 42.0 $M_{\odot}$. When the 14 % helium is considered, the total mass is found to be 66.7 $M_{\odot}$. Table 6.7 summarizes the main characteristics of S183.

6.1.3 EXCITING STAR OF S183

The distance to S183 given by Fich and Blitz[51] was kinematically determined, because no exciting star for the nebula had been identified. The distances to stars can be measured independent of kinematics. The stars in this field are quite faint, with the brightest (within the boundaries of plate 5.1) being SAO[61] 011502 with $m_v = 6.0$. Table 6.8 lists a number of the brighter stars in the field, that are identified in the SAO catalogue. There are two stars, numbers 011439 and 011476, that fall within the boundaries of S183. They have magnitudes 8.3 and 9.2, and are listed as spectral type A2 and A0 respectively.

From table 6.6, the model for S183 gives an excitation parameter $U = 16$ pc $cm^{2/3}$. Rohlfs[62] lists excitation

TABLE 6.7 SUMMARY OF THE MAIN CHARACTERISTICS OF S183

Coordinates	$l = 123.2^{\circ}$ $b = +2.9^{\circ}$
Distance	0.74 ± 0.51 kpc
Flux Density	
408 MHz	6.33 ± 0.40 Jy
1420 MHz	6.92 ± 0.50 Jy
N_e	$\simeq$ 12.5 cm^{-3}
Volume	$\simeq$ 155 pc^3
Mass	
Hydrogen	42.0 $M_{\odot}$
Hydrogen + Helium	66.7 $M_{\odot}$

Note: Assuming that component 1 is a complete hollow sphere and component 2 is a complete hollow hemisphere.

TABLE 6.8 SELECTED SAO STARS IN THE FIELD OF S183

#	SAO	RA	DEC	m_V	Spectral
	#	h m s	° ' "		Type
1	011400	0 45 09	64 50 50	7.1	G5
2	011411	0 46 06	65 46 44	8.7	G5
3	011416	0 46 39	64 48 39	8.0	A5
4	011439	0 49 29	65 37 12	8.3	A2
5	011476	0 53 17	65 26 17	9.2	A0
6	011502	0 55 20	66 04 57	6.0	B9

parameter vs. spectral type; a portion of his table is reproduced in table 6.9. An excitation parameter of 16 pc $cm^{2/3}$ (from the model parameters listed in table 6.9), indicates that a star with spectral type between B0 and B0.5 is responsible for exciting S183. Neither of the SAO stars that are within the boundary of S183 (SAO 011439 and SAO 011476), fits this description. The other stars within the boundaries of S183 are considerably fainter than these two, so that their $m_V \gtrsim 10$.

Allen[63] states that a main sequence B0 star has an absolute magnitude $M_V = -4.1$. Using equation 6.22, the apparent magnitude of such a star can be calculated, given that its distance coincides with that of S183.

$$m - M = 5 \log_{10}(r/10) \qquad 6.22$$

where: m = apparent magnitude
M = absolute magnitude ($M_V = -4.1$)
and r = distance in pc (740 pc)

The apparent magnitude of a B0 star at 740 pc works out to be $m = 5.25$, assuming no interstellar extinction, and no extinction by dust and gas in S183. Looking at the

TABLE 6.9 EXCITATION PARAMETER (U) FOR STARS OF SPECTRAL TYPE O4 TO B1 (Adapted from Rolphs[62])

Spectral Type	U (pc $cm^{2/3}$)
O4	148
O5	122
O6	90
O7	68
O8	54
O9	41
O9.5	34
B0	24
B0.5	11
B1	3.5

stars within the boundary of S183 on plate 5.1, it can be seen that they are at least magnitude 10 and fainter. Therefore, assuming that a B0 star is responsible for exciting S183, it must suffer at least 5 magnitudes of extinction. This is possible since there is considerable obscuration in this direction (plate 5.1).

6.1.4 THE SEARCH FOR A RADIO RECOMBINATION LINE IN S183

Recombination lines in the radio spectrum result from electrons undergoing downward transitions in the upper levels of the hydrogen atom. Finding such a line in S183 would be useful since it would confirm that S183 is indeed an HII region, since recombination lines are not observed in supernova remnants. Also a recombination line observation would allow an additional check on the distance given by Fich and Blitz[51], which is based on a CO radial velocity of $V_r = -10.3$ km s^{-1}. A recombination line velocity would also be useful information to have when the HI data from the synthesis survey is reduced.

An attempt was made to observe a recombination line in S183 with the DRAO 26 m telescope, but without success. It was quite difficult finding a line, within the range of the spectrometer, that was free of contamination by satellite interference.

Three lines were observed, H157α ,H158α ,and H159α , with rest frequencies of 1683.20, 1651.541, and 1620.672 MHz respectively. A receiver bandwidth of 2.0 MHz was used with frequency switching to record the line. In alternate cycles the receiver was tuned to the recombination line frequency and to a reference frequency 1 MHz lower. The difference between spectra on the line and at the reference frequency was calculated and integrated for about 10 minutes before recording. Each recorded spectrum was made up of 40 samples of 16 seconds duration. After collection, each recorded spectrum was plotted and inspected for satellite interference. The contaminated records were rejected with the remaining ones being added to form the final spectrum.

The H157α line had strong broadband satellite interference which made it unsuitable for observing S183. It was used as a check on the system by observing the HII region W3. The peak H157α brightness temperature on W3 after about 4 hours of integration was approx. 230 mK. E. J. Chaisson[64] gives H157α = 310 mK ± 10 mK.

S183 was observed at H158α for about 24 hours and at H159α for about 40 hours. Each spectrum was fitted with a fourth order polynomial using FITAPOLY to remove the curved baselines. Neither line was detected above the rms noise levels of 3.0 mK and 2.5 mK for H158 α and H159 α respectively.

The expected sensitivity of the H159 α recombination line search is given by

$$T_{rms} = \frac{T_{sys}}{\sqrt{\tau B}} \qquad 6.23$$

where: T_{sys} = system temperature (60 K),
B = channel bandwidth, (2MHz/(128 channels) = 15.6 KHz), and
τ = integration time in seconds (40 hours = 1.444×10^5 seconds).

When equation 6.23 is evaluated, T_{rms} = 1.27 mK. This value must then be multiplied by $\sqrt{2}$ because the reference spectrum is being subtracted from the "on" spectrum (the line is in both since switching is only 1 MHz in a 2 MHz band). Therefore the expected sensitivity is

$$\sqrt{2}\,(1.27) = 1.8 \text{ mK}.$$

This is reasonably close to the observed 2.5 mK.

6.2 IRAS (INFRARED ASTRONOMICAL SATELLITE) DATA

In 1983 an infrared telescope was launched into a 900 km circular orbit above the earth. During an 11 month period an all sky survey was completed in four wavelength bands centered on 12, 25, 60, and 100 μm[65].

IRAS maps of S183 in the 60 μm and 100 μm bands are shown in figures 6.9 and 6.10. These maps were obtained by accessing the data contained in the IRAS 60 and IRAS 100 micron survey (splines I) by van Albada et al.[66]. Both surveys are available in machine readable form on the VAX system at DRAO.

Figure 6.11 shows a 1420 MHz map with the 60 μm emission superimposed. This figure illustrates the relation of the infrared to that of the 1420 MHz continuum.

6.2.1 CALCULATION OF DUST TEMPERATURES

The IRAS maps at 60 μm and 100 μm can be used to calculate the temperature of dust grains (T_D) in S183 using equation 6.24 given by Evans[67].

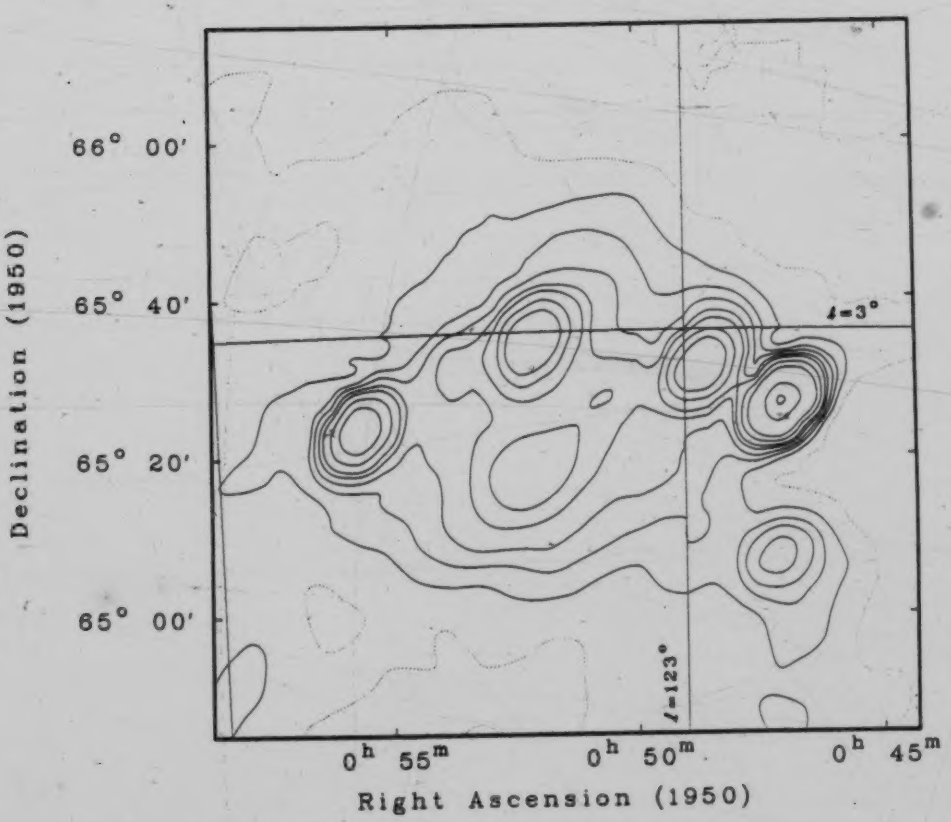

Figure 6.9
S183 at 60 μm

IRAS map of S183 at 60 μm. Angular resolution is 8'. Contours are at 60, 70, 80, 90, 100, 115, 130, 160, 200, 350, and 450 X (6.667 X 10^{-9} W/(m^2sr)). The elongated beam is an artifact of the scanning process used to acquire the data.

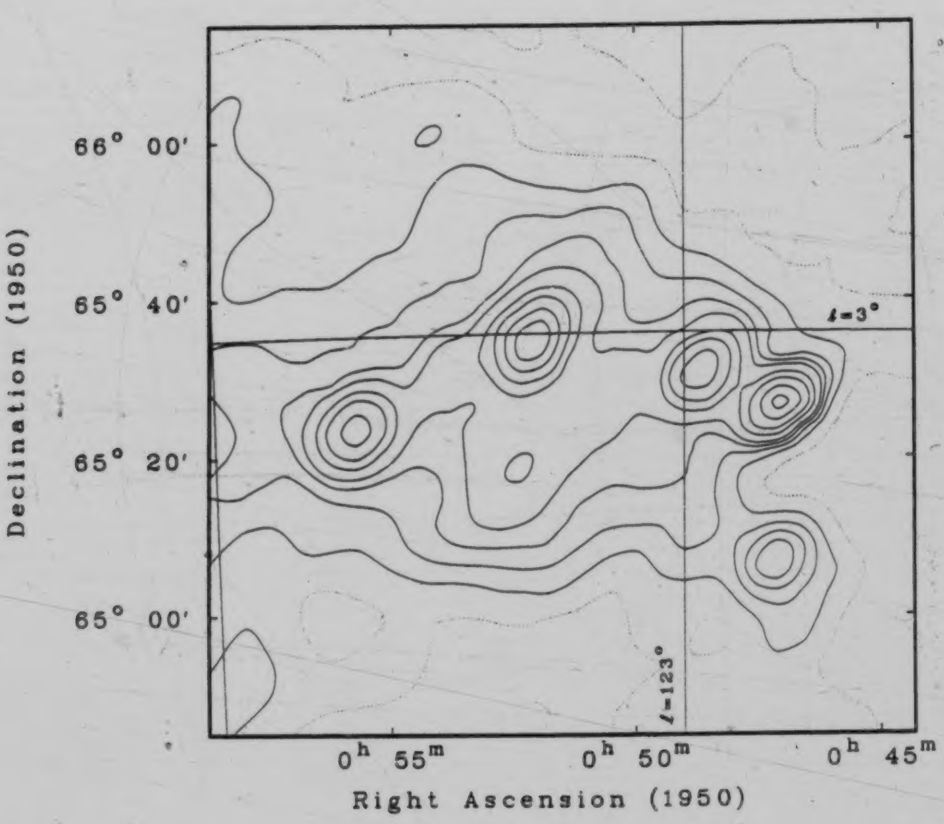

Figure 6.10
S183 at 100 μm

IRAS map of S183 at 100 μm. Angular resolution is 8′. Contours are at 175, 200, 225, 250, 275, 300, 350, 400, 475, 550, and 650 X (3.333 X 10^{-9} W/(m^2sr)).

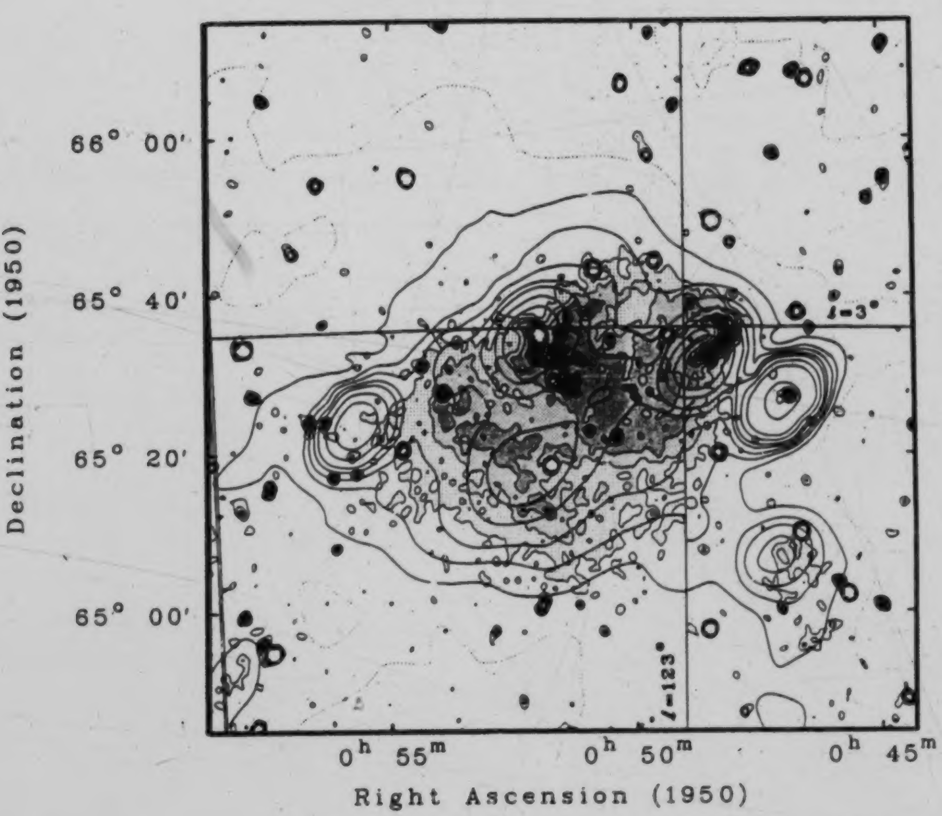

Figure 6.11

1420 MHz Map with 60 µm Emission Superimposed

$$T_D = \frac{\frac{hc}{k}\left(\frac{1}{\lambda_2} - \frac{1}{\lambda_1}\right)}{(3+\beta)\ln\left(\frac{\lambda_1}{\lambda_2}\right) + \ln\left(\frac{S\nu(\lambda_1)}{S\nu(\lambda_2)}\right)} \qquad 6.24$$

Here grain emissivity is assumed to follow $\varepsilon(\lambda) = \varepsilon_0 \lambda^{-\beta}$, $e^{hc/kT} >> 1$ for both λ_1 and λ_2, and

β = 1,

λ_1 = 60 µm,

λ_2 = 100 µm,

S_ν = flux density at λ_1 and λ_2,

h = Planck's constant,

c = velocity of light, and

k = Boltzmann's constant.

After removing backgrounds of 5.67×10^{-7} and 8.33×10^{-7} W m^{-2} sr^{-1} for the 60 µm and 100 µm maps respectively, and correcting for the different bandwidths, equation 6.24 was used to calculate the dust temperatures shown in figure 6.12. This figure shows that S183 has dust temperatures of approximately 46 K with ± 5K variations over its extent. The one exception to this is the infrared source on the west side of S183 at RA = 0^h 46^m 51.2^s, DEC = 65^o 27' 19". The dust temperature at this location is

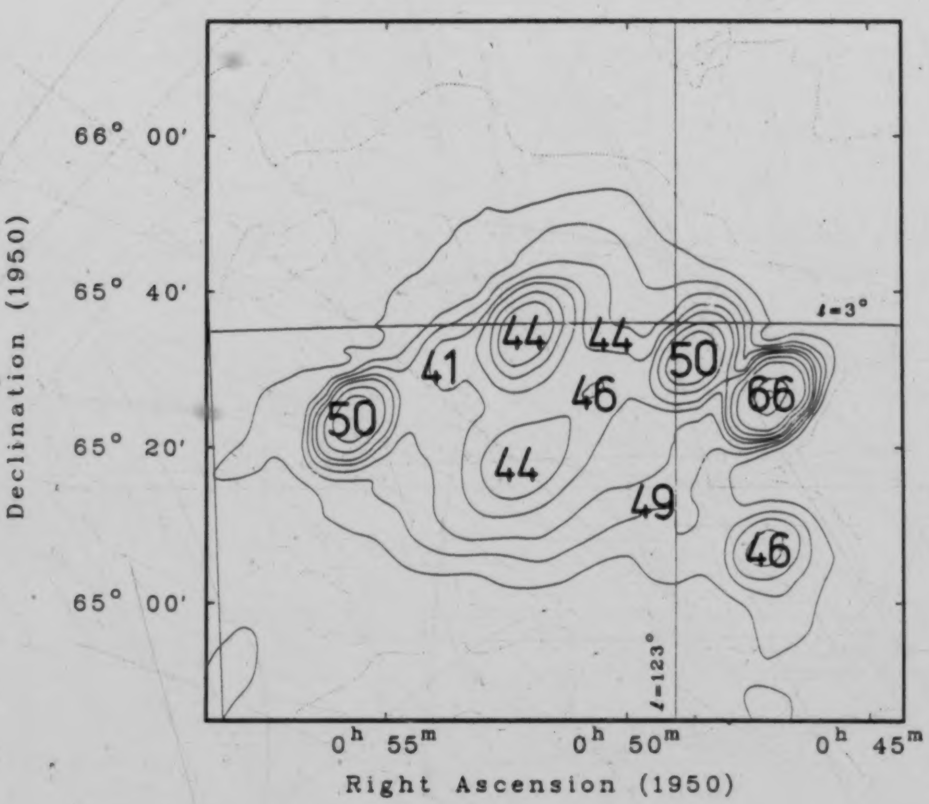

Figure 6.12
Map of $T_{D\ 60/100}$ For S183

IRAS map of S183 at 60 μm showing $T_{D\ 60/100}$ for various locations. Backgrounds of 5.67 X 10^{-7} W $m^{-2}sr^{-1}$ and 8.33 X 10^{-7} W $m^{-2}sr^{-1}$ have been removed from the 60 μm and 100 μm maps respectively, before calculating T_D.

66 K, or about 20 K warmer than those for S183. This source appears outside the boundary of S183 at 408 MHz and 1420 MHz.

6.2.2 CALCULATION OF THE PARAMETER "R"

Fürst, Reich, and Sofue[68] have proposed a method to distinguish between thermal and nonthermal sources using the ratio of IRAS 60 μm to radio 2.7 GHz emission. This method can be applied to S183 as a further check of its nature. They use the fact that the ratio R of infrared to radio continuum flux density is ~ 1000 for HII regions, whereas it is $\leq$ 15 for supernova remnants. This results from HII regions being much stronger infrared emitters than supernova remnants.

To obtain the ratio R for S183, the maps must be in the same units of Jy/sr, and the backgrounds must be subtracted. Since the ratio R for S183 as a whole is desired, the maps have not been converted to the same angular resolution. The beam size for both the IRAS 60 μm (8') and the 408 MHz (3.5' X 3.8') maps is much smaller than the angular dimensions of S183.

The program AIM(INTEGRATE) which was used to obtain the flux density of the 408 MHz polygons shown in figure 6.1 also gives the brightness after background subtraction for each polygon. When these values were averaged for the 408 MHz map the following value was obtained.

$$\bar{B}_{408} = 37,659 \text{ Jy sr}^{-1}$$

To convert the 60 µm map to brightness, van Albada et al.[66] give the multiplicative conversion factor 0.262 MJy sr^{-1}. The average of the 60 µm map is about 120 tape units, with a background of about 85 units. Therefore,

$$B_{60\ \mu m} = (120-85)(0.262 \times 10^6) \text{ Jy sr}^{-1},$$

giving $B_{60\ \mu m} = 9.17 \times 10^6 \text{ Jy sr}^{-1}$.

The R ratios by Furst et al.[68] use 2.7 GHz, so in this case the 408 MHz brightness should be converted to a 2.7 GHz brightness using a spectral index $\alpha = 0.07$ in equation 6.25 below.

$$B_{2.7\ GHz} = B_{408\ MHz}(2700/408)^{-0.07} \tag{6.25}$$

Using the value for the 408 MHz brightness found above, the 2.7 GHz brightness is found to be

$$B_{2.7\ GHz} = 32993 \text{ Jy sr}^{-1}.$$

Finally, R is obtained by taking the ratio of the

60 μm to 2.7 GHz brightness, giving

$$R = (9.17 \times 10^6)/(32993) = 278$$

From the above it can be seen that $R >> 15$, which shows again that S183 is probably an HII region, and not a supernova remnant.

6.3 LBN 0611

This is a small region of emission that is visible to the SW of S183 on both the 408 MHz and 1420 MHz maps. It is also evident on the red print of the Palomar Sky Survey shown in plate 5.1. The temperature brightness spectral index map (figure 6.4) shows it to have a spectral index in the range $1.9 \leq \beta \leq 2.3$, which indicates that it is a small HII region. Figure 6.12 shows it to have a dust temperature $(T_{D\ 60/100}) = 46$ K.

6.4 CONCLUSIONS

The 408 MHz and 1420 MHz maps of S183 which were obtained using the DRAO synthesis telescope, have better resolution than any previous surveys of the object. The information obtained from these maps has shown that S183 is an HII region and not a supernova remnant, as has been suggested previously in the literature.

Flux densities of 6.33 ± 0.40 Jy and 6.92 ± 0.50 Jy at 1420 MHz and 408 MHz have been found which corresponds to a spectral index of $\alpha = 0.07 \pm 0.07$. A map of spectral index shows that there are no significant variations of this parameter across the nebula, thus eliminating the possibility that the object is a supernova remnant superimposed on an HII region.

The radio continuum images reveal that a large part of the nebula is optically obscured. The distance to S183 is 0.74 ± 0.51 kpc based on a CO emission line measurement by Fich and Blitz[51]. Although no radio recombination lines were detected, 40 hours of observation with the DRAO 26 m telescope has placed an upper limit of 2.5 mK on H159α.

IRAS images also suggest that S183 is an HII region, with dust temperatures of 50 ± 5 K. Modeling indicates that S183 has a mass of ~ 42 $M_\odot$ of hydrogen or about 66.7 $M_\odot$ if 14 % helium is considered, with an overall electron density of ~ 12.5 cm^{-3}.

CHAPTER 7

CONCLUSIONS

This thesis has explored two topics which are related to the synthesis telescope at DRAO. The first is an investigation into the antenna performance at 1420 MHz. It has shown how to improve the sensitivity of the telescope by reducing the antenna temperature of the individual elements of the array.

Before this work, an estimate of antenna temperature equal to 19.8 K was obtained by considering the individual contributors in turn. This was about 5 or 6 K lower than the measured value of 26 K. By measuring the power pattern of one of the antennas, a better understanding of the individual contributors has been obtained. It has shown that feedleg scatter can account for most of the discrepancy between the estimated and measured values of antenna temperature. A numerical calculation of antenna temperature using the power pattern has given an antenna temperature of 27.6 K, which is in good agreement with the measured value of 26 K. This demonstrates that the values of the individual contributors to antenna temperature are known with a reasonable degree of accuracy.

A reduction of antenna temperature due to spillover and feedleg scatter was obtained by adding two modifications to the antenna. The first modification was a fence attached to the rim of the antenna, which lowered the antenna temperature by about 8 K. It accomplished this by partially suppressing the spillover lobe and the feedleg scatter lobes. The second modification involved changing the shape of the feedlegs from a circular to a triangular cross-section. About a 5 K improvement in antenna temperature was realized as a result of this modification.

Modifying the antenna with a fence to improve the performance of the telescope at 1420 MHz could degrade the performance at 408 MHz, by increasing the sidelobes in the front half of the antenna pattern. For this reason, changing the shape of the feedlegs seems to be the best modification to implement at this time to reduce the antenna temperature. It is a relatively easy modification to the existing and future antennas of the array, and would have little influence on their mechanical performance.

The second topic of this thesis is a discussion of an observation of Sharpless 183 (S183), made with the DRAO synthesis telescope. Previous observations of this object failed to show conclusively whether it is an HII region or a supernova remnant. The 408 MHz and 1420 MHz maps from the synthesis telescope have better resolution than any of the previous observations of this object. Flux densities of 6.33 ± 0.40 and 6.92 ± 0.50 Jy have been found at 1420 MHz and 408 MHz respectively. These measurements combined with previously published flux densities give a spectral index of 0.10 ± 0.05, which implies that S183 is probably an HII region and not a supernova remnant. There is no significant spectral index variation across the nebula. The radio continuum images reveal that a large part of the nebula is optically obscured. This likely accounts for the failure to identify the exciting star of the nebula. A kinematic distance of 740 pc to S183 has been estimated based on the probable association with a CO cloud with a measured radial velocity of -10.3 Km s^{-1}.[51] Modeling indicates that ~ 67 $M_\odot$ of ionized material is present with N_e ~ 12.5 cm^{-3}. Comparison with IRAS images also suggests that S183 is an HII region. An upper limit of 2.5 mK has been placed on the H159 α brightness temperature as a result of 40 hours of observation with the DRAO 26 m telescope.

REFERENCES

1. Christiansen, W.N., and Hogbom, J.A. 1985, Radiotelescopes, Second Ed. (Cambridge University Press), pp. 169-172.

2. Ibid, p. 25.

3. Ibid, p. 248.

4. Ibid, pp. 107-111.

5. Ibid, pp. 239-241.

6. Nyquist, H. 1928, Phys. Rev., vol. 32, 110-113.

7. Veidt, B. 1981, Internal Report, Antenna Performance Tests, DRAO. p. 18.

8. Jordan, E.C., and Balmain, K.G. 1968, Electromagnetic Waves and Radiating Systems, (Prentice-Hall, Inc., New Jersey) p.415.

9. Veidt, B., 1984, A 408 MHz Synthesis Radio Telescope, M.Sc. Thesis, University of Alberta, Edmonton, pp. 31-32.

10. Mumford, W.W. 1961, Proceedings of the IRE, Vol. 49, 427-447.

11. David, V., and Voge, J. 1969, Propagation of Waves, (Pergamon Press, London England), p.109.

12. Higgs, L.A., 1967, Bull. Astr. Inst. Netherlands, Suppl. 2, 59-76.

13. Westman, H.P. 1968, Reference Data For Radio Engineers, (Howard W. Sams and Co. Inc., Indianapolis) pp 25-48.

14. David, V. and Voge, J. 1969, Propagation of Waves, (Pergamon Press, London England), p. 44.

15. Kraus, J.D. 1966, Radio Astronomy, (McGraw-Hill, New York) p.159.

16. Narasimhan, M.S., Raghavan, K., and Ramanujam, P. 1983, IEEE Transactions on Antennas and Propagation, Vol. AP-31, No. 5, 792.

17. Mumford, W.W. 1961, Proceedings of the IRE, Vol. 49, 427-447.

18. Hombach, V., and Thielen, H. 1984, Electronic Letters, Vol. 20, No 19, 792.

19. Brink, R.W., 1942, Spherical Trigonometry, (Appleton-Century-Crofts, New York), pp. 21-22.

20. Rusch, W.V.T., Sorensen, O., and Baars, J.W.M. 1982, IEEE Transactions on Antennas and Propagation, Vol. AP-30, No. 4, 789.

21. Rusch, W.V.T., Appel-Hansen, J., Klein, C.A., and Mittra, R. 1976, IEEE Transactions on Antennas and Propagation, Vol. AP-24, No.2, 182.

22. Kildal, P., Olsen, E., Aas, J.A. 1988, IEEE Transactions on Antennas and Propagation, Vol. AP-36, No. 2, 186-188.

23. Ibid, 182.

24. Ibid, 185.

25. Satoh, T., Endo, S., Matsunaka, N., Betsudan, S., Katagi, T., and Ebisui, T. 1984, IEEE Transactions on Antennas and Propagation, Vol. AP-32, No. 7, 698-704.

26. Ibid, 699.

27. Ibid, 700.

28. Kildal, P., Olsen, E., Aas, J.A. 1988, IEEE Transactions on Antennas and Propagation, Vol. AP-36, No. 2, 189.

29. Ibid, 188.

30. Sharpless, S. 1959, Astrophys. J. Suppl. vol. 4, 257.

31. Kallas, E., and Reich, W. 1980, Astron. and Astrophys. Suppl., vol. 42, 227-243.

32. Galt, J.A., and Kennedy, J.E.D. 1968, Astron. J., Vol. 73, 135.

33. Felli, M., and Churchwell, E. 1972, Astron. and Astrophys. Supp., vol. 5, 369-432.

34. Churchwell, E., and Walmsley, C.M. 1973, Astron. and Astrophys., vol. 23, 117-124.

35. Bonsignori-Facondi, S.R., and Tomasi, P. 1979, Astron. and Astrophys., vol. 77, 93-100.

36. Clark, D.H., Caswell, J.L., Mon. Not. R. Astr. Soc., vol. 174, 267.

37. Fich, M., and Blitz, L. 1984, Astrophys. J., vol. 279, 125-135.

38. Haslam, C.G.T., Salter, C.J., Stoffel, H., and Wilson, W.E. 1982, Astron. and Astrohys. Suppl., vol. 47, 1.

39. Kallas, E., and Reich, W. 1980, Astron. and Astrophys. Suppl., vol. 42, 227-243.

40. Hogbom, J.A. 1974, Astron. and Astrophys. Suppl., vol. 15, 417.

41. Steer, D.G., Dewdney, P.E., and Ito, M.R. 1984, Astron. and Astrophys. Suppl., vol. 137, 159-165.

42. Shortspac, A Systematic Approach to Adding Short Spacing Data. DRAO Helpfile Documentation.

43. Landecker, T.L. Oct. 1987, AGC Corrections to Synthesis Telescope Observations At 408 MHz, DRAO Documentation. DRAO, Penticton, B.C.

44. California Institute of Technology. 1954, National Geographic Society - Palomar Sky Atlas. Pasadena, U.S.A.

45. Kraus, J. D. 1966, Radio Astronomy (McGraw-Hill, New York), p.306.

46. Altenhoff, W., Mezger, P., G., Strassl, H., Wendker, H., Westerhout, G. 1960, Veroff Sternwarte, vol. 59, 48.

47. Churchwell, E., and Walmsley, C.M. 1973, Astron. and Astrophys., vol. 23, 117-124.

48. Galt, J.A., and Kennedy, J.E.D. 1968, Astron. J., vol. 73, 135.

49. Felli, M., and Churchwell, E. 1972, Astron. and Astrophys. Supp., vol. 5, 369-432.

50. Bonsignori-Facondi, S.R., and Tomasi, P. 1979, Astron. and Astrophys., vol. 77, 93-100.

51. Fich, M. and Blitz, L. 1984, Astrophys. J., vol. 279, 125-135.

52. Burton, W.B., and Gordon, M.A. 1978, Astr. Ap., vol. 63, 7.

53. Blitz, L., Fich, M., and Stark, A.A. 1980, Interstellar Molecules, ed. B.H. Andrew, (Reidel, Dordrecht), p.213.

54. Fich, M. and Blitz, L. 1984, Astrophys. J., vol. 279, 126.

55. Blitz, L. and Fich, M. 1983, Kinematics, Dynamics and Structure of the Milky Way, ed. W.L.H. Shuter (Reidel, Dordrecht), p. 143.

56. Higgs, L.A., Feb. 1986, RADPHYS, A Program to Calculate Some Simple Quantities Relevant to the Study of HII Regions. DRAO, Penticton, B.C.

57. Allen, C.W. 1976, Astrophysical Quantities, (The Athlone Press, London), p. 102.

58. Lang, K.R. 1980, Astrophysical Formulae, (Springer-Verlag, New York), p. 46.

59. Rohlfs, K. 1986, Tools of Radio Astronomy, (Springer-Verlag, Berlin), p. 178.

60. Higgs, L.A., Feb. 1986, RADPHYS, A Program to Calculate Some Simple Quantities Relevant to the Study of HII Regions. DRAO, Penticton, B.C.

61. Smithsonian Astrophysical Observatory Star Catalog, 1966, (Smithsonian Institution, Cambridge, Mass.).

62. Rohlfs, K. 1986, Tools of Radio Astronomy, (Springer-Verlag, Berlin), p. 249.

63. Allen, C.W. 1976 Astrophysical Quantities, (The Athlone Press, London), p. 206.

64. Chaisson, E.J. 1972, Nature Phys. Sc., vol. 239, 83.

65. Walker, G. 1987, Astronomical Observations, (Cambridge University Press, England), p. 108.

66. van Albada, G.D., Baud, B., Boulanger, F., de Pagter, P.J., Pol, W., Renes, J.J. and Wesselius, P.R. 1984, Internal Report, Laboratory for Space Research, University of Groningen.

67. Evans, N.J.,II. 1980, Interstellar Molecules, ed. B.H. Andrew, (Reidel, Dordrecht), p. 4.

68. Furst, E., Reich, W., Sofue, Y. 1987, Astron. and Astrophys. Suppl., vol. 71, 63-67.